WFPS-TME-104
UC-20,20A,20B,20D

REACTOR APPLICATION OF AN IMPROVED BUNDLE DIVERTOR

T. F. YANG
G. W. RUCK
A. Y. LEE
G. SMELTZER
T. PREVENSLIK

NOVEMBER 1978

PREPARED FOR THE US DEPARTMENT OF ENERGY
CONTRACT EG-77-C-02-4544

fusion power systems department

Westinghouse Electric Corporation
P.O. Box 10864, Pgh. Pa. 15236

DISCLAIMER

WFPS-TME-104
NOVEMBER 1978

REACTOR APPLICATION OF AN IMPROVED BUNDLE DIVERTOR

PREPARED BY: T. F. YANG, G. W. RUCK, A. Y. LEE,
G. SMELTZER, AND T. V. PREVENSLIK

REVIEWED BY: G. Gibson
G. GIBSON, MANAGER
NUCLEAR AND PLASMA ENGINEERING

APPROVED BY: T. C. Varljen
T. C. VARLJEN, MANAGER
ENGINEERING

fusion power systems department

Westinghouse Electric Corporation
P.O. Box 10864, Pgh. Pa. 15236

ACKNOWLEDGEMENT

This work was performed for the Office of Fusion Energy of the U.S. Department of Energy under Contract EG-77-C-02-4544. Reproduction, translation, publication, use and disposal, in whole or in part, by or for the United States Government is permitted.

Many informative discussions with D. L. Chapin and J. E. Faulkner on the nuclear shielding problems, the review of the manuscript and numerous suggestions of G. Gibson and T. C. Varljen, are acknowledged by the authors.

Printed in the United States of America
Available from
National Technical Information Service
U. S. Department of Commerce
5285 Port Royal Road
Springfield VA 22161
Price:Printed Copy $5.50;Microfiche $3.00

ABSTRACT

A Bundle Divertor was chosen as the impurity control and plasma exhaust system for the beam driven Demonstration Tokamak Hybrid Reactor - DTHR. In the context of a preconceptual design study of the reactor and associated facility a bundle divertor concept was developed and integrated into the reactor system. The overall system was found feasible and scalable for reactors with intermediate toroidal field strengths on axis. The important design characteristics are: the overall average current density of the divertor coils is 0.73 kA for each tesla of toroidal field on axis; the divertor windings are made from superconducting cables supported by steel structures and are designed to be maintainable; the particle collection assembly and auxiliary cryosorption vacuum pump are dual systems designed such that they can be reactivated alternatively to allow for continuous reactor operation; and the power requirement for energizing and operating the divertor is about 5 MW.

TABLE OF CONTENTS

Section		Page No.
1.0	INTRODUCTION	1-1
2.0	MAGNETICS OF THE BUNDLE DIVERTOR	2-1
	2.1 MAGNETIC CONFIGURATION STUDY	2-1
	2.2 MAGNETIC STRESS ANALYSIS	2-11
3.0	DIVERTOR OPERATION	3-1
	3.1 DIVERTOR OPERATION	3-1
	3.2 PARTICLE REMOVAL AND VACUUM SYSTEM	3-3
	3.3 PLASMA SHEATH	3-8
	3.4 THE COLLECTOR EDGE PROBLEM	3-9
4.0	MECHANICAL DESIGN	4-1
	4.1 MECHANICAL DESIGN	4-1
	4.2 DIVERTOR COLLECTOR ASSEMBLY DESIGN	4-13
	4.3 ALTERNATE COLLECTOR ASSEMBLY DESIGNS	4-14
	4.4 DIVERTOR COIL MAINTENANCE	4-18
5.0	CRYOGENIC DESIGN OF THE DIVERTOR MAGNETIC COIL	5-1
	5.1 SUPERCONDUCTOR DESIGN PARAMETERS	5-1
	5.2 REFRIGERATION LOADS	5-7
6.0	THERMAL DESIGN OF THE PARTICLE COLLECTORS	6-1
	6.1 COLLECTOR V-TUBES	6-1
	6.2 FRONT TUBES	6-3
7.0	COLLECTOR STRESS EVALUATION	7-1
	7.1 V-SHAPED TUBE BUNDLE AND THERMAL SHIELD	7-1
	7.2 LOADING EVALUATION	7-2
	7.3 STRESS ANALYSIS	7-3
	7.4 STRUCTURAL CRITERIA AND EVALUATION	7-5
	7.5 RECOMMENDATIONS	7-11

TABLE OF CONTENTS (CONTINUED)

Section		Page No.
8.0	SHIELDING ASSESSMENT	8-1
9.0	DIVERTOR POWER REQUIREMENTS	9-1
	9.1 DIVERTOR COIL CHARGING REQUIREMENTS	9-1
	9.2 REQUIREMENTS FOR THE BUS	9-1
	9.3 POWER SUPPLY	9-3
	9.4 POWER REQUIREMENT SUMMARY	9-3
10.0	SUMMARY AND CONCLUSIONS	10-1
11.0	REFERENCES	11-1

LIST OF FIGURES

Figure No.		Page No.
2-1	The Evolution of Divertor Improvements from DITE to ISX-B.	2-2
2-2	Flux Patterns for: (a) DITE-Type Divertor; (b) W-ISX-B Divertor with Circular Coils; (c) $\overline{W}$-ISX-B Divertor with D-Shaped Coils.	2-4
2-3	Plan View of the Diverted Flux Bundle Expanded by a Pair of Mirror Coils.	2-7
2-4	Magnetic Flux Patterns for Different Divertor Angles for a Range of Toroidal Field Intensities.	2-8
2-5	Flux Expansion as a Function of Divertor Angle α. I_D/B_T is Constant.	2-10
2-6	Angular and Cross-Sectional Grids for Force Computation.	2-13
2-7	Stress Distributions Over the Cross Sections at the Middle of Segments 1 and 10.	2-14
2-8	Stress Distributions: (a) Without Divertor, and (b) (b) With Divertor, Over the Cross Section of TF Coil Intersecting Midplane.	2-15
3-1	Particle Collector Systems. No Advanced Particle and Thermal Flux Expansion Assumptions are Used. Water-Cooling is Chosen as a Reference; This Represents the Most Stringent Design Case.	3-4
3-2	Side View of a Conceptual Dual Particle Collection and Regeneration System.	3-6
3-3	The Illustration of a Dual Cryosorption Module for Simultaneous Pumping and Regeneration.	3-7
3-4	Plasma Power Profile on the Collector as a Spatial Function from the Separatrix.	3-10
4-1	Demonstration Tokamak Hybrid Reactor.	4-2
4-2	DTHR Bundle Divertor Plan View.	4-3

LIST OF FIGURES (CONTINUED)

Figure No.		Page No.
4-3	Bundle Divertor Coil Cut-Away Views.	4-5
4-4	Bundle Divertor Side Elevation.	4-12
4-5	Collector System (Alternate Scheme I).	4-15
4-6	Collector System (Alternate Scheme II).	4-17
4-7	DTHR Bundle Divertor Concept Plan View when the Coils are Outside the Vacuum Vessel.	4-19
4-8	DTHR Bundle Divertor Concept Side Elevation for the Divertor Coils Outside the Vacuum Vessel.	4-20
4-9	DTHR Bundle Divertor Coil Removal Sequence.	4-22
5-1	Oversimplified Divertor Coil Model for Cryogenic Design.	5-2
5-2	Cryogenic Recovery Capability of the Nb_3Sn Superconductors at 10 and 7 Tesla.	5-6
6-1	Bundle Divertor Particle Collector Tubes.	6-2
6-2	Circumferential Temperature Distribution at Tube Outlet End.	6-5
6-3	Steady State Circumferential Temperature Distribution of the Front Thermal Shield Tube.	6-7
7-1	Thermal Shield Tube Worst Case Duty Cycle.	7-4
7-2	Estimated Amzirc Stress Rupture Data.	7-9
8-1	Neutron and Gamma Fluxes at Distances from First Wall.	8-2
8-2	Total Nuclear Heating Rate. Data Taken from TNS.	8-3
9-1	Divertor Power Supply System.	9-2

LIST OF TABLES

Table No.		Page No.
2-1	DTHR REFERENCE PLASMA PARAMETERS	2-5
2-2	DTHR BUNDLE DIVERTOR COIL PARAMETERS	2-6
2-3	COMPARISON OF DIVERTOR PARAMETERS	2-12
5-1	PRELIMINARY SPECIFICATIONS FOR THE MAGNETIC COIL AND THE Nb_3Sn SUPERCONDUCTORS FOR THE DTHR BUNDLE DIVERTOR OPERATED AT 10 TESLA	5-4
5-2	PRELIMINARY SPECIFICATIONS OF Nb_3Sn SUPERCONDUCTORS FOR DTHR BUNDLE DIVERTOR OPERATED AT 7 TESLA	5-5
6-1	SUMMARY OF THERMAL DESIGN OF WATER-COOLED V-TUBES FOR PARTICLE COLLECTION	6-4
10-1	SUMMARY OF KEY BUNDLE DIVERTOR DESIGN PARAMETERS	10-2

1.0 INTRODUCTION

Magnetic divertors, either poloidal or bundle divertors, are perceived as active means of impurity control and helium (fusion ash) removal for tokamak fusion reactors. Because of the design difficulties of a divertor, which were identified in the past, many other schemes, such as impurity reversal, cool gas blanket, low Z coating of the first wall, etc., have been suggested as alternative means for impurity control. However, the physics of these methods are not clear, none of them has been demonstrated experimentally, and most important of all, none of them solves the problem of helium removal. Without this function, a sustained long-burn pulse is probably not possible. Based on physics understanding, experimental evidence, and engineering methods, divertors still remain the best alternative at this time. Therefore, what is important is the demonstration of continuous design improvement and the potential for further improvement. One example is the compact poloidal divertor[1] which demonstrated significant design advances in the poloidal divertor area. The work reported here provides significant improvements over the original bundle divertor concept[2]. Although not all of the design issues are resolved, the basis has been established for consideration of the bundle divertor as a viable option for tokamak fusion reactor application. Furthermore, many of the remaining areas of uncertainty are amenable to near-term experimental examination.

The critics of the bundle divertor contend that it is not applicable to a reactor because the divertor current and forces and power consumption are inherently large[3,4]. However, it has been shown that the current density and forces can be greatly reduced with an improved design method for an experimental tokamak device ISX-B[5]. This report will demonstrate that such an improved divertor is applicable to a reactor with a toroidal field on the plasma axis as high as 5.5 T and aspect ratio of 4.3. This field is considered to be in the intermediate range. The application of the bundle divertor to a reactor with lower field and smaller aspect ratio has also been demonstrated with somewhat different modifications[6,7].

The most significant achievement is the reduction in required divertor current density; the current densities per tesla of field to be nulled are 25 kA/cm^2 for DITE, 11 kA/cm^2 for ISX-B and 1 kA/cm^2 for the present DTHR bundle divertor concept.

Besides designing an efficient divertor magnetic system, attention has been given to design details which enable the evaluation of an integrated divertor system. This includes the cryogenic design of the divertor coils, mechanical and maintenance design of the divertor coil assembly, the mechanical and thermal design of the divertor collector system, the method of cycling the collector to permit essentially continuous operation of the reactor, and associated materials and stress analyses. Another accomplishment is that the divertor assembly has been designed for removal and maintenance.

It should be emphasized that an attempt was made to evaluate the collector system under the most severe operating conditions. The system appears to be feasible, but is by no means state-of-the-art. Therefore, advanced design and experimental programs should be carried out to quantitively establish design margins and provide an engineering proof of principle demonstration.

The bundle divertor concept reported here was developed as part of the integrated pre-conceptual design of a near-term Demonstration Tokamak Hybrid Reactor (DTHR)[8,9]; therefore, it was necessary to address such integration feasibility issues as coil interaction forces, the divertor assembly mechanical interface with the tokamak, and radiation shielding space.

2.0 MAGNETICS OF THE BUNDLE DIVERTOR

2.1 MAGNETIC CONFIGURATION STUDY

It has been shown in previous work[5] that an improved bundle divertor design can be employed in the experimental device ISX-B, which can be scaled to reactors. In this section, the practical feasibility of such a divertor for reactors is discussed along with the potential for further improvement. A typical reactor, DTHR[8,9], is used as a design model; however, a scaling method, which is based on the intensity of the field to be nulled, is also given.

For completeness of the discussion, the method of design improvement is described again here. The first improvement is shown by Figure 2-1a. An additional pair of auxiliary divertor coils has been provided on the vertical plane passing through the center leg of the divertor coils. One coil is directly above and another coil is directly below the original divertor coils, and they are located symmetrically with respect to the mid-plane. The function of the auxiliary coils is to reduce the toroidal field locally in the divertor region and to make the locus of the stagnation points of the separatrices vertical instead of concave toward the divertor coils. The radiation shielding space between the stagnation points and conductor inside the loop of the separatrix is increased and becomes uniform. The second improvement is shown in Figure 2-1b as it has been applied to the ISX-B device. The turns of the new divertor coils are distributed over a larger area than that of the original DITE design. The width of the coil is doubled while the radial depth is the same. The current requirement is reduced while the stagnation point is at the same location. This is possible by increasing the radius of the successive turns of the divertor coils. The fields on the geometrical axis and the stagnation point can be kept the same and the turns are located further away from the plasma while the radius is increased. The radius of each turn is determined by the ripple requirement on the axis, the angular opening of the gap between the TF coils, the vertical space and mechanical design considerations.

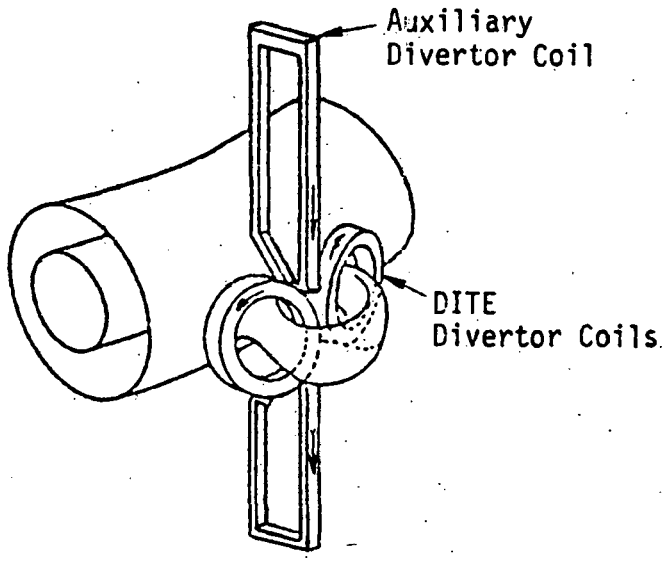

(a)

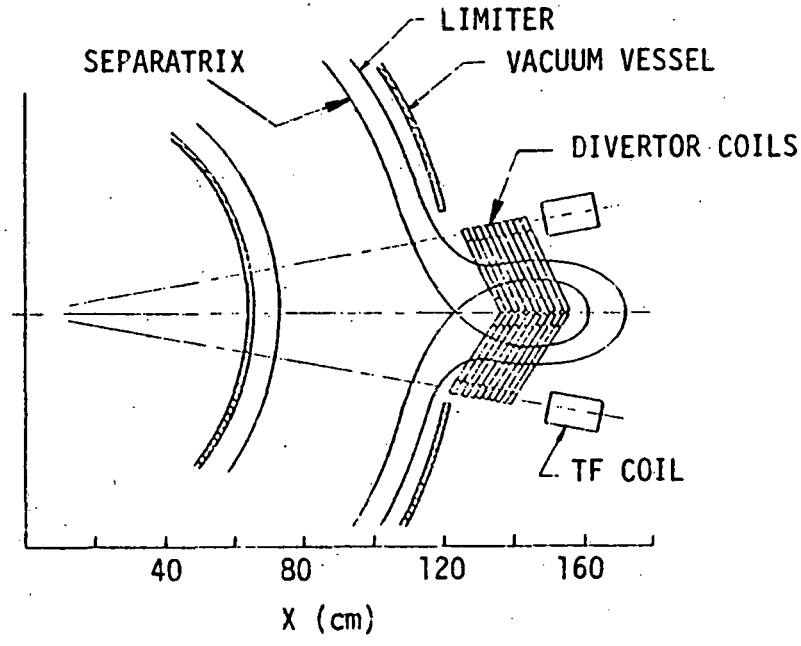

(b)

Figure 2-1. The Evolution of Divertor Improvements from DITE to ISX-B.
(a) Trimetric View - Showing the Auxiliary Coils Applied to the Original DITE Divertor
(b) Plan View - Showing an Effective Way of Distributing the Turns in ISX-B.

The divertor coils can be made in a D-shape instead of circular. A comparison of the divertor flux of these three cases, i.e., the DITE-type and the improved design with circular coils and D-shape coils, are shown by Figure 2-2. The fluxes extend further away from the plasma and the expansion is larger in the improved designs. The D-shaped coils provide the best results.

A comparison of required currents and the current densities and stress distribution will be discussed later. In the following, the application of this improved divertor to a reactor is discussed.

The bundle divertor has been designed as an integrated impurity control and exhaust system for DTHR, a beam driven hybrid tokamak currently being investigated by Westinghouse. Although a beam driven device, the plasma parameters and power density are expected to be in the intermediate range considered for future reactors. The magnetic field on axis, B_o = 5.45 T, is slightly higher than intermediate values considered these days. The important parameters of the DTHR are listed in Table 2-1, and the flux configurations are shown by Figure 2-3. As mentioned in the introduction, this is the optimal configuration constrained by the predetermined machine parameters.

The divertor design should be scalable. The main constraint on the divertor scaling is the toroidal magnetic field strength. To understand this particular important scaling relationship, the variation of the divertor flux configuration with field intensity and divertor coil angle has been studied. The results are presented in Figures 2-4 and 2-5. Figure 2-4 shows the variation of the flux configurations with respect to divertor angle and magnetic field intensity on axis. In each case, the currents in the divertor and auxiliary coils were adjusted until the null point was nearly at the same location. The flux is diverted to larger major radius and has a larger expansion for the larger divertor coil angle, α, at a fixed B_t. If the space inside and between the TF coils is limited it is better to use a larger α. The upper limit of α for DTHR is 40° constrained by the given space between the first wall and the inner surface of the TF coil dewar and 60 cm of shielding. If we denote the radial width of the flux bundle by ΔR and radial distance of the loop of the separatrix intersecting the centerline by Rs, the expansion of the diverted flux is defined

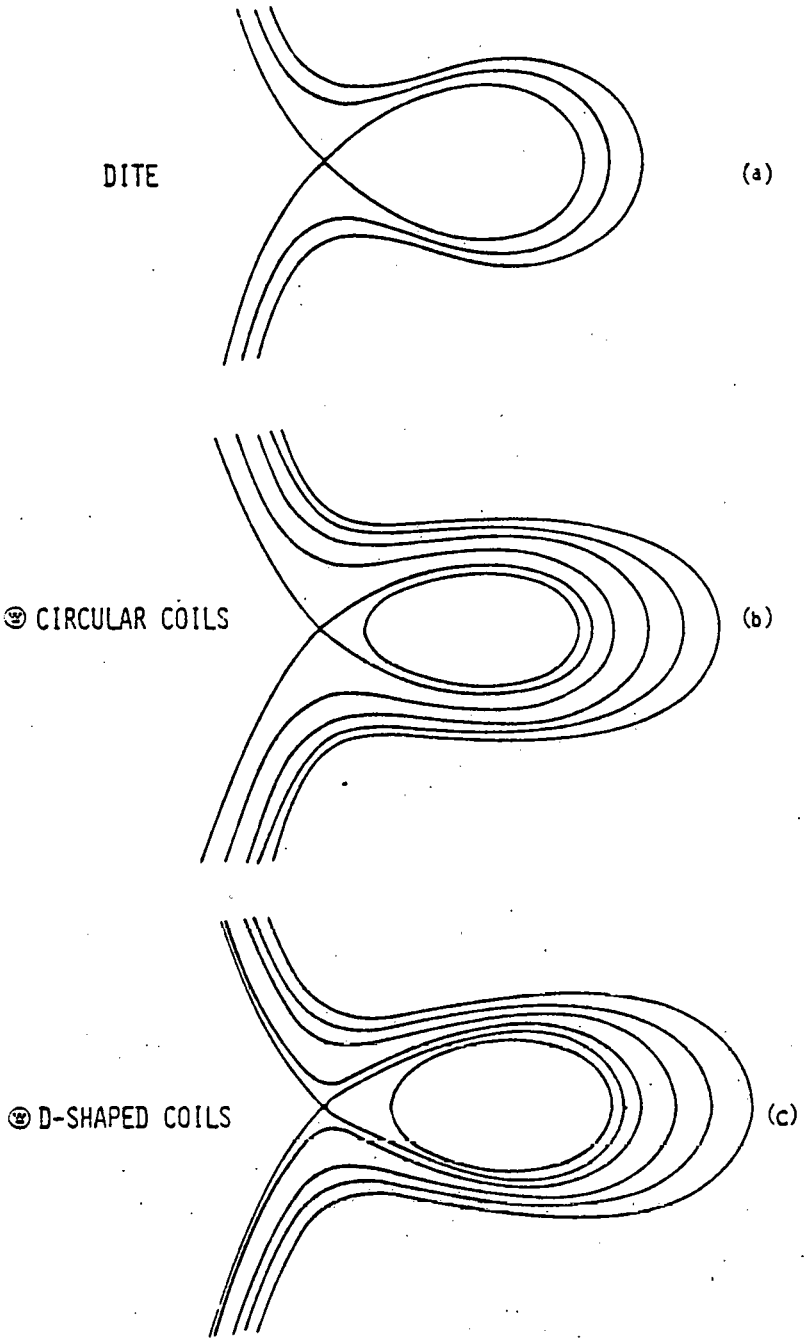

Figure 2-2. Flux Patterns for: (a) DITE-Type Divertor; (b)Ⓦ-ISX-B Divertor with Circular Coils; (c)Ⓦ-ISX-B Divertor with D-Shaped Coils.

TABLE 2-1

DTHR REFERENCE PLASMA PARAMETERS
(MARCH 1978)

MAJOR RADIUS	5.2 m
MINOR RADIUS	1.2 m
ELONGATION	1.6
TOROIDAL FIELD ON AXIS	5.5 T
PLASMA CURRENT	5.1 MA
NEUTRAL BEAM POWER	150 MW_t
PLASMA TEMPERATURE	13 keV
ELECTRON DENSITY	1.5×10^{20} m^{-3}
PLASMA β	6%
POLOIDAL β	4.0
WALL LOADING	2 MW/m^2
FUSION POWER	950 MW_t
REQUIRED τ_E	0.5 s
EMPIRICAL τ_E	2.0 s
$n_e\tau_E$	7.5×10^{19} m^{-3} s
DISCHARGE PULSE LENGTH	70 s
RESET TIME	15 s
PLANT AVAILABILITY	40%

MASTER

G. Haas
D. Beard
J. E. Baublitz
F. E. Coffman
J. F. Clarke
R. C. Davidson
N. A. Davies
E. E. Kintner
J. Murphy
K. Zwilsky
C. R. Head
U.S. Department of Energy (G-234)
Office of Fusion Energy
Washington DC 20545

Dr. E. Rossi
U.S. Department of Energy
Office of Laser Fusion
Washington DC 20545

U. S. Department of Energy
(2 reproducible copies)
Technical Information Center
P. O. Box 62
Oak Ridge TN 37830

O. B. Morgan
D. Steiner
Oak Ridge National Laboratory
P. O. Box Y
Oak Ridge TN 37830

D. M. Meade
M. B. Gottlieb
E. Frieman

Princeton University
Plasma Physics Laboratory
P. O. Box 451
Princeton NJ 08540

Dr. F. R. Scott
Dr. N. A. Amherd
Piet Bos
Electric Power Research Institute
3412 Hillview Avenue
P. O. Box 10412
Palo Alto CA 94304

K. R. Schultz
S. C. Burnett
General Atomic Company
P. O. Box 81608
San Diego CA 92138

W. C. Gough
DoE Office
Electric Power Research Institute
Palo Alto CA 94304

B. K. Jensen
Research and Development
Public Service Electric & Gas Company
80 Park Place
Newark NJ 07101

E. J. Kohler
E. S. Halfmann
Philadelphia Electric Company
2301 Market Street
Philadelphia PA 19101

J. Luoma
W. Hirst
R. Williams
General Public Utilities Service Corp.
260 Cherry Hill Road
Parsippany NJ 07054

James L. Mulloy
J. A. Vaughn
Los Angeles Department of Water & Power
P. O. Box 111
Los Angeles CA 90051

C. C. Baker
S. D. Harkness
Argonne National Laboratory
9700 S. Cass Avenue
Argonne IL 60439

T. J. Driscoll
John Weissmantle
John Valente
Long Island Lighting Company
175 E. Old Country Road
Hicksville NY 11801

C. E. Taylor (L-384)
J. D. Lee
Lawrence Livermore Laboratory
University of California
P. O. Box 808
Livermore CA 94550

Dr. R. Uhrig
Vice President, Nuclear Affairs
Florida Power & Light Company
9250 West Flagler Street
Miami FL 33101

Dr. George Watkins
Empire State Electric Energy
Research Corporation
1271 Avenue of the Americas
New York NY 10020

J. Powell
Brookhaven National Laboratory
Upton, Long Island NY 11973

F. L. Ribe
University of Washington
MS FL-10
Seattle WA 98195

Dr. Heinz Pfeiffer
Pennsylvania Power & Light Company
2 North Ninth Street
Allentown PA 18101

G. R. Siegel
Tennessee Valley Authority
1360 Commerce Union Bank Building
Chattanooga TN 37041

D. E. Simmons
Houston Lighting & Power Company
Houston TX 77001

W. B. Bechanan
Kentucky Utilities Company
120 South Limestone
Lexington KY 40507

T. J. Burke
Long Island Lighting Company
P. O. Box 618
Wading River NY 11792

S. J. Buchsbaum
Bell Laboratories
Crawford Corner Road
Holmdel NJ 07733

D. R. Cohn
Francis Bitter Laboratory
Massachusetts Institute of Technology
120 Albany Street
Cambridge MA 02139

R. W. Conn
G. Kulcinski
Nuclear Engineering Department
University of Wisconsin
Madison WI 53706

E. C. Creutz
National Science Foundation
1800 G Street, N.W.
Washington DC 20440

Dr. Harold L. Falkenberry
Power Research & Development Branch
Tennessee Valley Authority
503 Power Building
Chattanooga TN 37401

Dr. V. A. Finlayson
Utah Power & Light Company
P. O. Box 899
Salt Lake City UT 84110

S. O. Dean (Dr.)
Science Applications, Inc. (SAI)
8400 West Park Drive
McLean VA 22104

Mr. E. C. Fiss
Duke Power Company
Design Engineering Department
P. O. Box 2178
Charlotte NC 28242

C. W. Giesler
Wisconsin Public Service Corp.
P. O. Box 1200
Green Bay WI 54305

R. Goodrich
Northeast Utilities
P. O. Box 270
Hartford CT 06101

W. H. Hightower
Electric Plant Board
101 N. Main Street
Hopkinsville KY 42240

W. C. Wolkenhauer
Washington Public Power Supply System
P. O. Box 968
300 George Washington Way
Richland WA 99352

H. Yoshikawa
Westinghouse Hanford Company
P. O. Box 1970
Richland WA 99352

R. Krakowski
Los Alamos Scientific Laboratory
P. O. Box 1663
Los Alamos NM 87544

L. M. Lidsky (Rm 38-174)
Massachusetts Institute of Technology
Department of Nuclear Engineering
Cambridge MA 02139

Dr. Ron Liikala
Battelle Memorial Institute
Pacific Northwest Laboratory
P. O. Box 999
Richland WA 99352

Sidney Law
Northeast Utilities
P. O. Box 270
Hartford CT 06101

R. E. Aronstein
Advanced Nuclear Systems Research
& Engineering
Bechtel Corporation
P. O. Box 3965
San Francisco CA 94119

Dr. J. N. Grace
Princeton Area Office
U. S. Department of Energy
James Forrestal Campus
Princeton University
P. O. Box 451
Princeton NJ 08540

TABLE 2-2

DTHR BUNDLE DIVERTOR COIL PARAMETERS

FIELD ON AXIS	B_T = 5.5 T
ASPECT RATIO	A = 4
TWO D-SHAPED DIVERTOR COILS CURRENT/COIL	= 14.0 MA-turns
TWO VERTICAL AUXILIARY COILS CURRENT/COIL	= 6.4 MA-turns
DIVERTOR COIL ANGLE (see Figure 3-15)	α = 40°
AVERAGE DIVERTOR COIL DIAMETER	d = 2.65 m
OVERALL WIDTH OF THE COIL	ℓ = 1.15 m
SUPERCONDUCTOR CABLE	2 cm x 2 cm Nb_3Sn/Cu
CABLE CURRENT	32 kA
CABLE CURRENT DENSITY	8 kA/cm^2
COIL STRUCTURE	STAINLESS STEEL BOBBINS CONSTANT THICKNESS
SHIELDING SPACE BETWEEN CONDUCTOR AND FIRST-WALL	= 0.60 m
HELIUM INLET TEMPERATURE*	= 4.2 K
PUMPING POWER (THERMAL)	= 3.5 MW
COIL INDUCTANCE	= 126 mH
ELECTRICAL POWER SUPPLY (30 MIN CHARGING TIME)	= 600 kW

*Forced flow supercritical helium cooling at 4 atm inlet pressure.

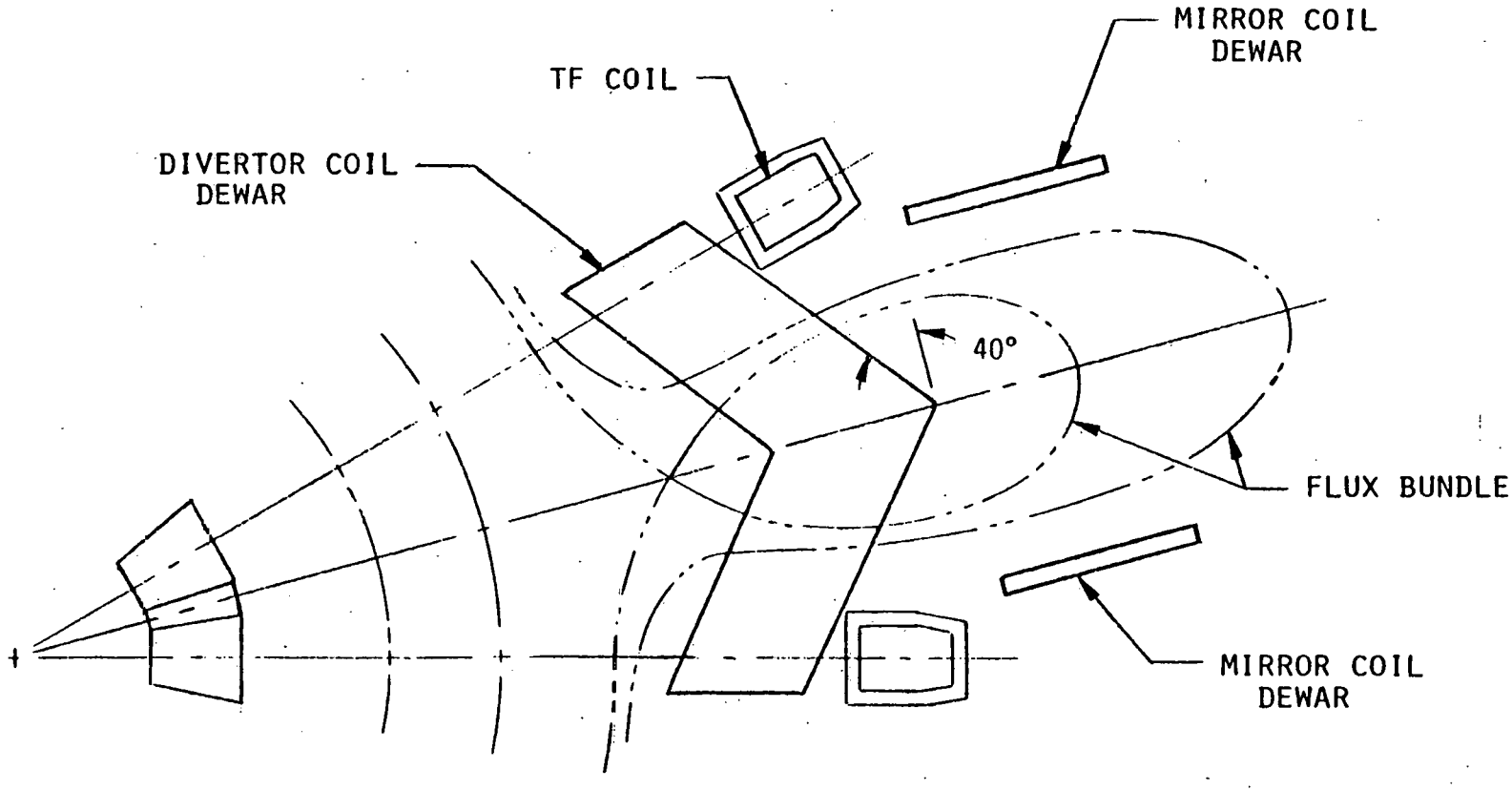

Figure 2-3. Plan View of the Diverted Flux Bundle Expanded by a Pair of Mirror Coils.

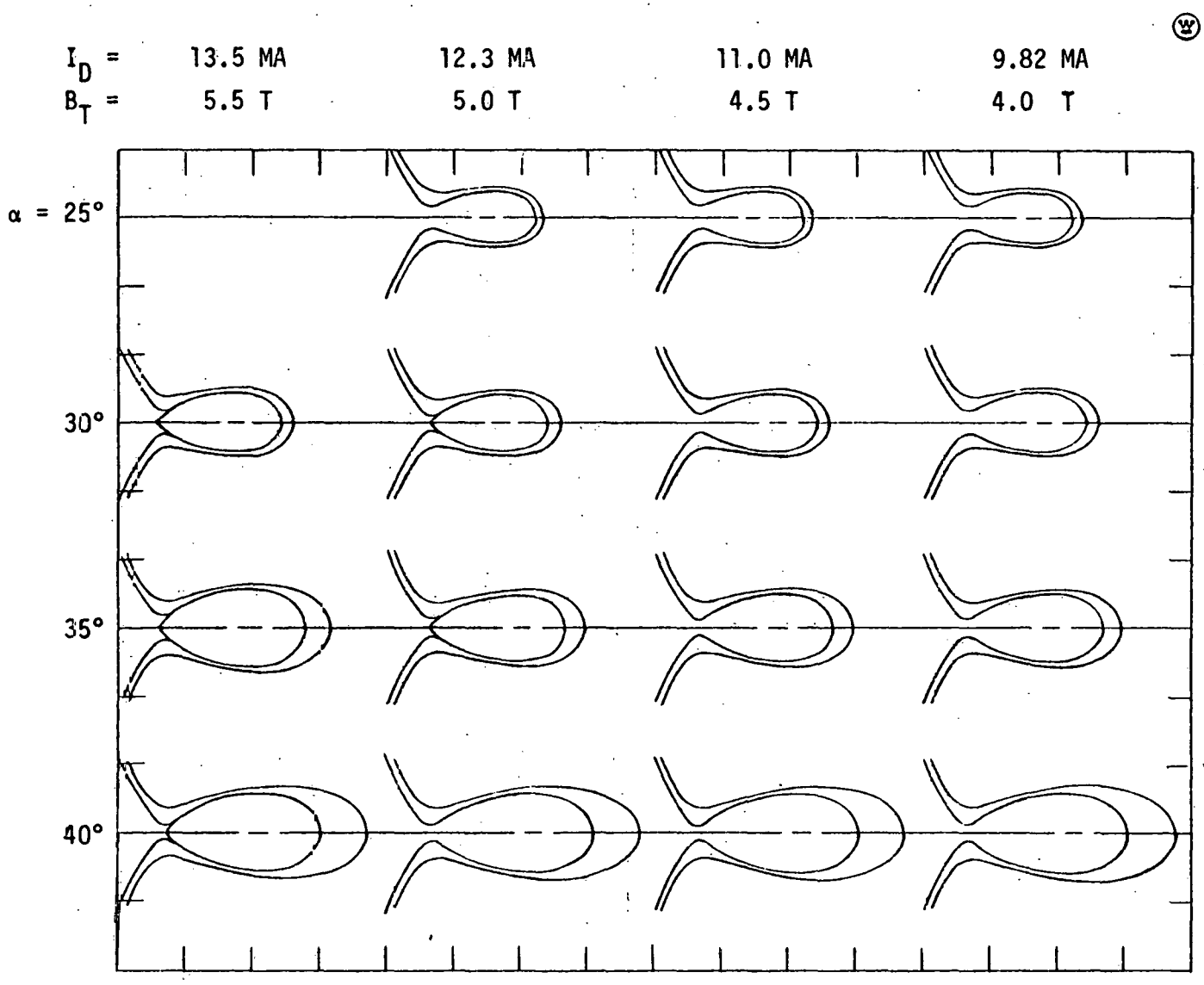

Figure 2-4. Magnetic Flux Patterns for Different Divertor Angles for a Range of Toroidal Field Intensities.

as

$$\varepsilon = \frac{\Delta R}{\delta_{SC}}$$

where δ_{SC} is the scrape-off layer thickness. ε is plotted as a function of α for constant B_t/I_D in Figure 2-5. The current density chosen for DTHR is the upper limit based on a maximum allowable current of 32 kA for the Nb_3Sn/Cu cable of 2 cm x 2 cm cross section (see Section 4). The variation of the flux, current and current density in the divertor coils with the size of the reactor depends on the number and the size of TF coils, but they are dominated by the toroidal field intensity which has to be nulled. The toroidal field contribution to the total field at the null point is given by

$$B_{null} = \frac{B_o R_o}{(R_o + a + \delta_{null})} = \frac{B_o A}{(A + 1 + \frac{\delta_{null}}{a})}$$

where δ_{null} is the distance of the null point to the outer plasma edge (by observation varying roughly as $\delta_{null} \simeq \frac{2}{3} a$). The current requirement would be less for smaller aspect ratios. The upper limit of B_{null} is about 4.0 T. Therefore, the bundle divertor is applicable to a reactor of intermediate field strength. The information provided here gives a general idea of the scaling of a bundle divertor of this design. Consistent with $B_{null} = 4.0$ T, it is possible to design a bundle divertor for a reactor having $B_o = 6$ T with A = 3, a = 2 m, and $\delta_{null} = 1.0$ m.

As was mentioned previously, the divertor parameters given in Table 2-2 were chosen to satisfy the physical constraints where the TF bore size was predetermined from other considerations. One such consideration was to keep the TF coils as compact as possible so that SF coils would not be too far away from the plasma. This in turn allowed keeping the SF coil currents and energy storage within reasonable magnitudes.

The diverted flux at the particle collector can be further expanded by a pair of mirror coils energized by a small current of 200 kA. This results in a total expansion in radial width $\varepsilon = 15$.

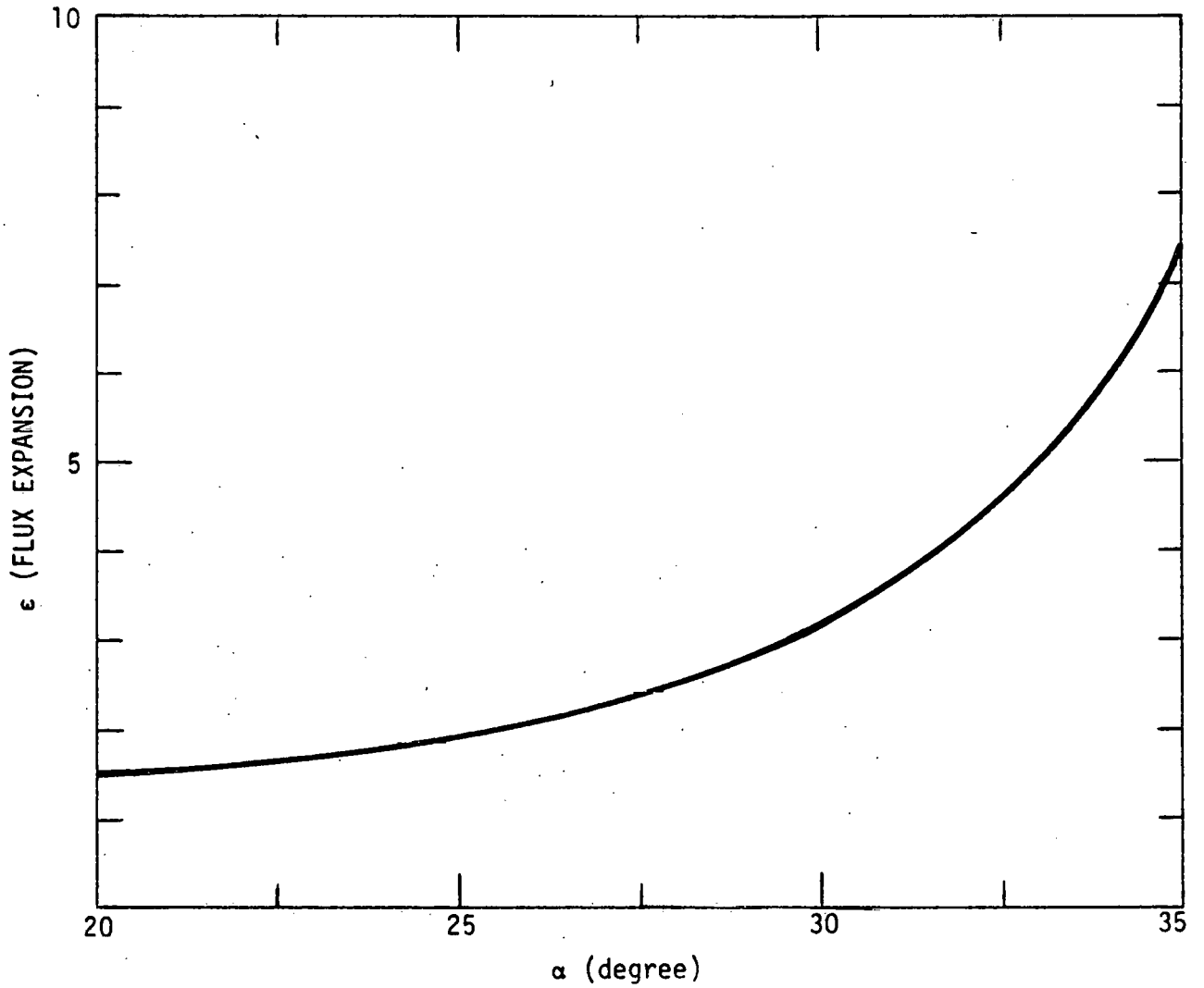

Figure 2-5. Flux Expansion as a Function of Divertor Angle α. I_D/B_T is Constant.

Table 2-3 compares the toroidal fields and currents and current densities per tesla of field intensity for DITE TYPE, ISX-B, and DTHR divertors. The reduction in current density per tesla is significant.

2.2 MAGNETIC STRESS ANALYSIS

It had been generally conceded that the torques and forces on divertor coils are too large to be constrained for a reactor application. Because the current is high and is concentrated in a limited area, there is little space available for structure. Therefore, previously one had to rely on the strength of the conductor to resist the torque and stress. However, as has been pointed out in some recent work[5], the current can be reduced and the space available for conductors can be doubled for ISX-B. This means enough structure can be provided to counter the stress. It was pointed out that the internal stress distribution is very important. Although the current density required is much smaller for the DTHR, the magnetic field intensity and total current is much larger. It is important that the stress distribution for DTHR be analyzed.

The detailed magnetic stresses have been computed on the grid points illustrated by Figure 2-6. Each half of each coil is divided into 10 circular arc segments at equal angular intervals. Figure 2-7 shows the force per unit area per meter over the cross sections near 0° and 180°. The stresses are largest at the right edge and decrease toward the left edge. They also change directions from the upper end to the lower end. There are points where the stresses are zero. The internal torques are small. The maximum stresses are f_ρ = 0.3 kN/cm^3, and f_Z = 0.22 kN/cm^3. The internal structure can easily be designed for the maximum stresses. The net outward translational force is 44×10^6 N, which can also be restrained.

The magnetic stress distribution over the cross section intersected by the midplane of the outside TF coil leg without the divertor energized, is shown by Figure 2-8a. The stress is symmetric and is the highest at the center of the inner edge. The net radial force is 20 MN/m; the tension at this point is 5.8 MN/m. When the divertor is energized, the stress distribution is shown by Figure 2-8b where it is seen that the symmetry is destroyed. The net radial

TABLE 2-3
COMPARISON OF DIVERTOR PARAMETERS

	DITE TYPE	Ⓦ ISX-B DIVERTOR	Ⓦ DTHR DIVERTOR
B_T	1.8 T	1.8 T	5.5 T
α	25°	25°	40°
I_D	3.2 MA	2.2 MA	28 MA
J_D	40 kA/cm^2	13.8 kA/cm^2	4 kA/cm^2
J_D/B_T	22 kA/cm^2-T	7.7 kA/cm^2-T	0.73 kA/cm^2-T

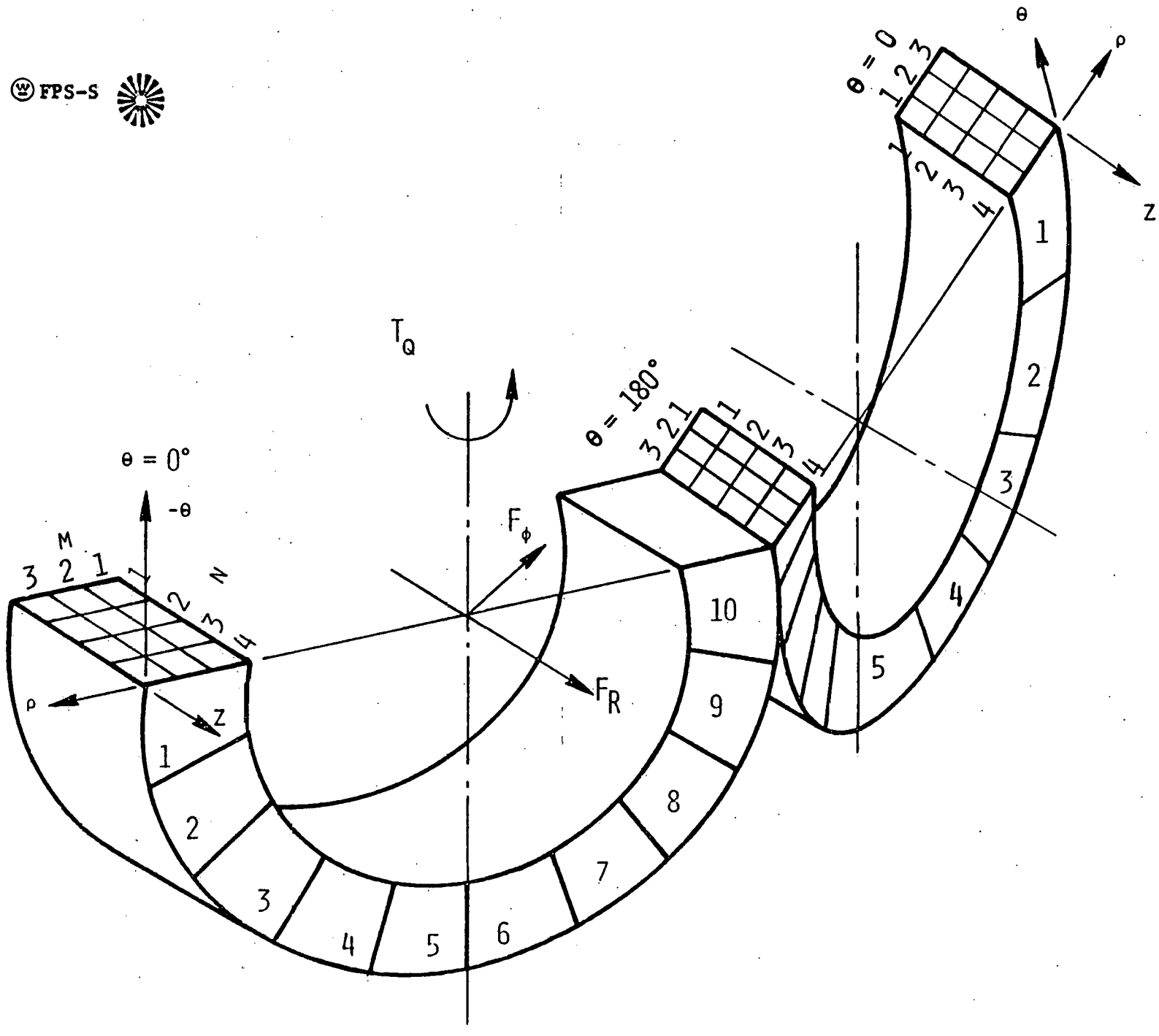

Figure 2-6. Angular and Cross-Sectional Grids for Force Computation.

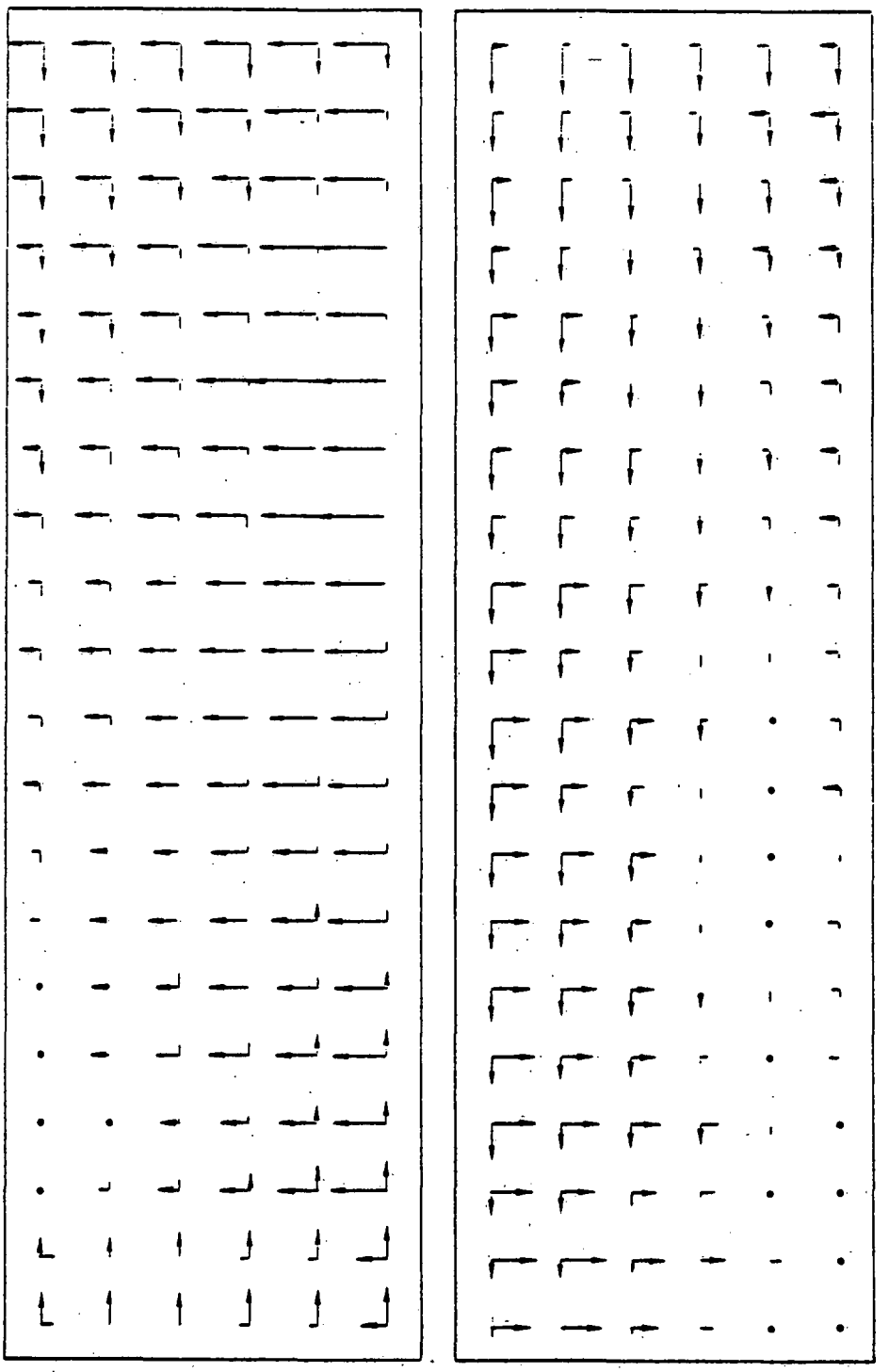

Figure 2-7. Stress Distributions Over the Cross Sections at the Middle of Segments 1 and 10.

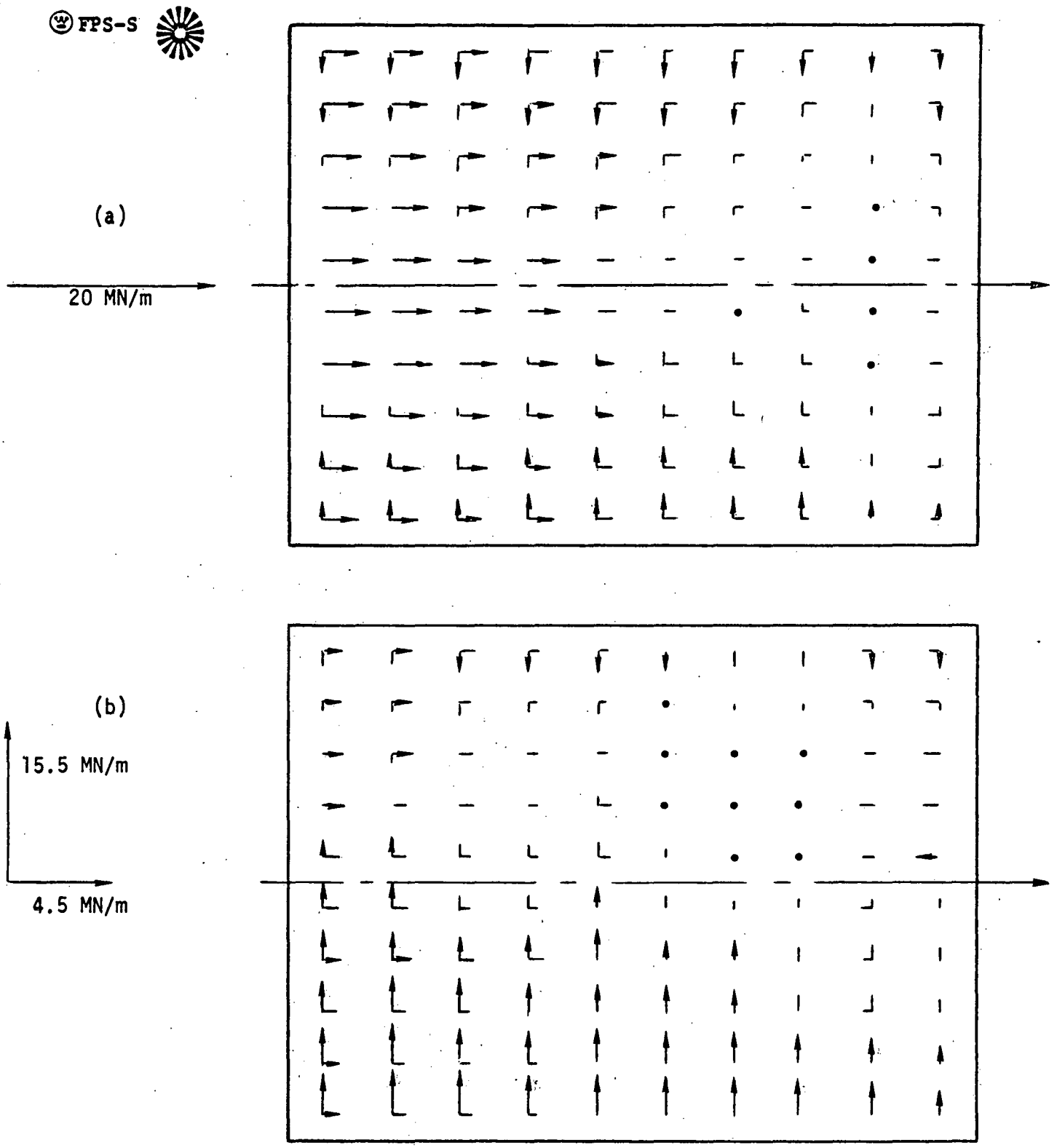

Figure 2-8. Stress Distributions: (a) Without Divertor, and (b) With Divertor, Over the Cross Section of TF Coil Intersecting Midplane.

force becomes 4.5 MN/m and tension becomes 1.03 MN/m. There is 15.5 MN/m lateral on the TF coil. The net force on the TF, due to the divertor coils, tends to push them apart.

3.0 DIVERTOR OPERATION

The properties of the plasma stream, which flows into the divertor, and all the requirements and principles of operation of the divertor will be discussed in this section. Based on these requirements and operating principles a sufficiently detailed design of each component, including cryogenic, thermal, vacuum, and mechanical design, were carried out to demonstrate feasibility.

3.1 PLASMA PROPERTIES

The fusion power of the reference DTHR is 950 MW. The power associated with the α-particles is about 190 MW, and the power associated with the neutral beams is 150 MW. All of this power (340 MW), less the radiated power, will go to the divertor in the form of particle diffusion losses. The total power to the divertor is about 280 MW.

It has been theoretically predicted and observed experimentally that the density profile in the scrape-off layer drops sharply[10-17]. The effect of a bundle divertor on the diffusion coefficients has been discussed in detail by Stott, et al.[17] for a divertor having a strong divertor magnetic mirror where the mirror ratio M is $>> \varepsilon = a/R$ and is about 2 to 3. In this design the mirror ratio has been reduced to the order ε. Thus, the mirror is much weaker than is given in the theory. Therefore, further studies are needed in order to apply the theory directly. A simplified model of Keilhacker[13] will be used. Experiments on FM_1[15] and DIVA[16] indicate that the flow velocity into the divertor is about one-third of the sound speed. The observed widths of the scrape-off layers in DIVA[16] and DITE[17] are consistent with the sound model and a perpendicular diffusion coefficient corresponding to 0.1 to 0.5 times the Bohm diffusion. In DIVA the diffusion coefficient was also shown to have the functional dependence expected for Bohm diffusion. Thus, we can reasonably assume that the perpendicular diffusion coefficient $D_\perp$ is 0.5 times the Bohm diffusion and can be written as

$$D_\perp = 0.5 \frac{kT}{16\ eB}$$

The flow velocity can be written as

$$\nu_{||} = \frac{1}{3}\sqrt{\frac{2kT}{m}}$$

Assuming that the particles travel around the torus about 10 turns before being diverted[2], the geometrical path length, L, into the divertor is roughly

$$L \cong 2\pi R q_D$$

where $q_D = 2\pi/x_D$ and x_D is the divertor acceptance angle[17] and S is the shape factor. The e-folding characteristic width in the scrape-off layer is

$$\Delta = (D_{\perp}\,\tau_{||})^{1/2}$$

where $\tau_{||} = L/\nu_{||}$. Therefore,

$$\Delta = \frac{0.5}{16}\,\frac{kT}{eB}\,\frac{2\pi q_D R}{\frac{1}{3}\sqrt{\frac{2kT}{m}}}$$

$$= \left(0.6\,\frac{q_D R}{eB}\,\sqrt{\frac{mkT}{2}}\right)^{1/2}$$

If the mean temperature in the scrape-off layer is assumed to be 0.5 keV, and using the averaged value $q_D = 10$, then

$$\Delta \cong 10 \text{ cm}\ .$$

The unloading and shielding efficiencies are in excess of 90% as established experimentally by DITE[17]. These values do not influence the design of the collector system because an unloading efficiency of 100% is assumed which gives the maximum particle and thermal fluxes as a design basis.

3.2 PARTICLE REMOVAL AND VACUUM SYSTEM

The average particle density of the plasma is $\bar{n} = 1.5 \times 10^{14}$ cm^{-3}. Assuming the particle confinement time $\tau_p = 1$ s, the particle current streaming into the divertor is

$$Q = \frac{2\pi^2 Sa^2 R_o \bar{n}}{\tau_p} \simeq 3.6 \times 10^{22}/s$$

The particle throughput to the divertor is 1080 $\tau\ell$/s which has to be removed, and the back-streaming to the plasma has to be kept as low as possible. The thermal power of 280 MW also has to be transferred. The projected area of the flux bundle available for particle collection is 6 m^2. That is, the maximum height of the flux bundle is 2 m and the radial width is 3 m. Here, we will concentrate on the mechanical collection function which is in fact the most stringent requirement.

For sustaining a long burn time at reasonably high vacuum, the collector must be able to trap the particles with a high sticking probability and holding capacity. The materials suitable for this purpose have been surveyed and given in another report[1]. In this report, it is assumed that the commercially available alloy, Zr/Al, which is deposited on constantan (copper and Zr alloy) and which has been reported to have a trapping efficiency of 100% and holding capacity of 2×10^{19} cm^{-2} at a temperature of approximately 200°C[18] is employed. The reference pulse length of DTHR consists of 70 s operation and 15 s down. The collector should be able to hold the particles for many operating cycles so that the $\sim$ 80% duty cycle can be maintained.

It is not possible to regenerate the collector during the 15 s downtime. Therefore, the projected surface is increased by employing 10 V-shaped surfaces, which consist of water-cooled pipes as shown by Figure 3-1. The total surface area is

$$A_C = 2\left(\frac{\pi}{2} N\ell\right) = 188 \text{ m}^2$$

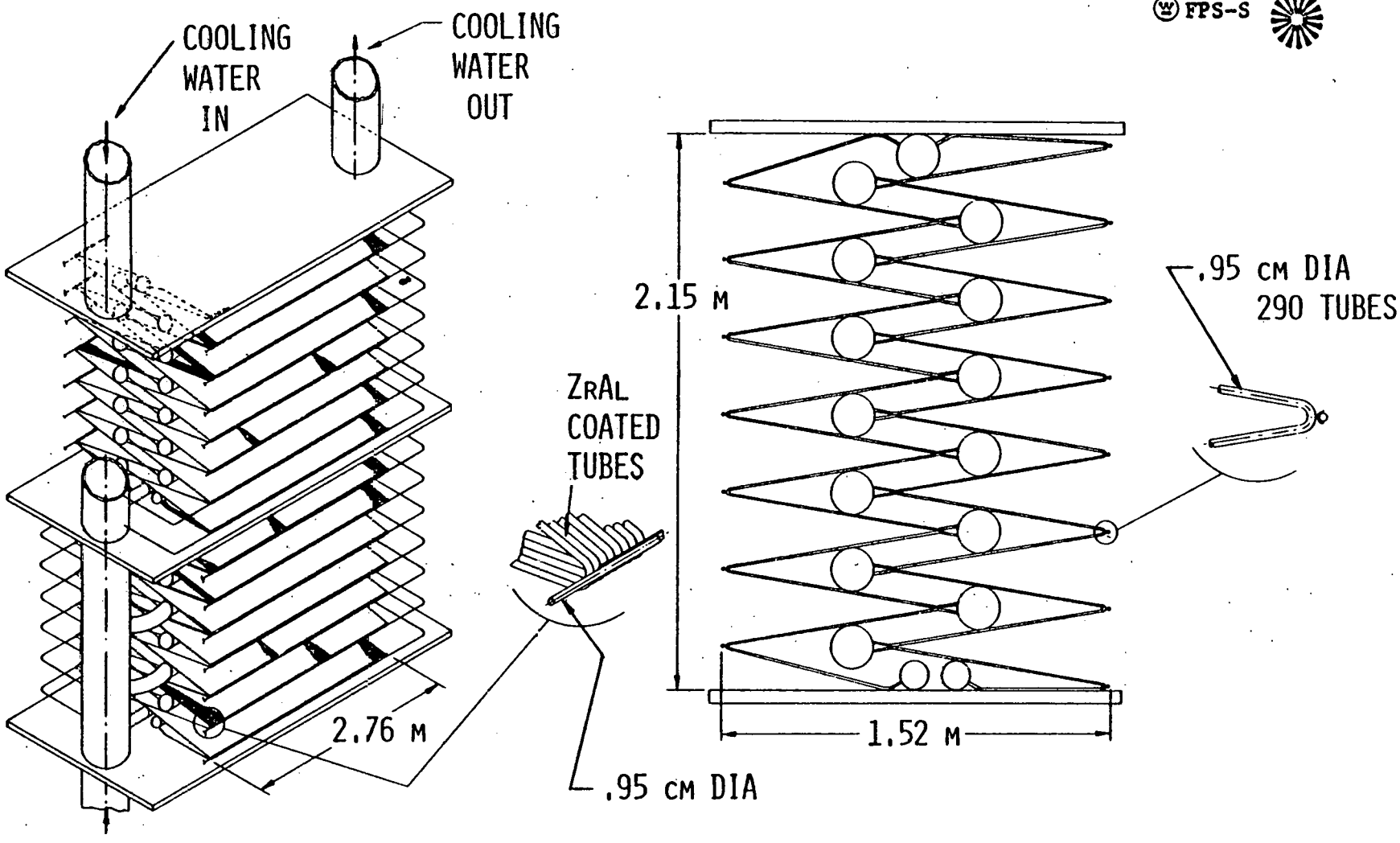

Figure 3-1. Particle Collector Systems. No Advanced Particle and Thermal Flux Expansion Assumptions are Used. Water-Cooling is Chosen as a Reference; This Represents the Most Stringent Design Case.

Therefore, the average particle flux per unit area is

$$\bar{\dot{\phi}} = \frac{\dot{n}}{A_C} = 1.9 \times 10^{20} \text{ particle/s/m}^2.$$

The holding time will be 1053 seconds or 17 minutes. The collector will be designed to be regenerated at 10 minute intervals or at $\sim$ 60% of the full capacity. Therefore, seven cycles are used.

The helium concentration is about 1% of the plasma stream or 10.8 $\tau\ell$/s throughput. A trapping efficiency for helium of 60% can be expected[19]. It will be pessimistically assumed to be zero. To maintain a helium partial pressure of 10^{-5} torr, a pumping speed of 1.1×10^6 ℓ/s is required. The specific speed of a cryosorption surface is $\sim$ 3.7 ℓ/s/cm^2[20]. Therefore, about 30 m^2 of projected area of cryopanel is needed which can be easily designed around the enclosure of the burial chamber. The method of regenerating the collector and the cryopanel without interrupting the tokamak operation is described below.

As shown by Figures 3-2 and 3-3, both the collection and cryosorption panels are dual units. Figure 3-2 shows that collection unit II is in the lower chamber and is sealed at the top. This unit is warmed up to 600°C to release the trapped particles which are pumped and collected. In the meantime, unit I is collecting particles. Before reaching the capacity of unit I, the whole collection system is lifted up slowly until unit I enters the chamber on the top which is then sealed for regeneration. This cycle is reversed when unit II reaches its capacity. The system is designed to move at $\sim$ 1 m/s. For increasing the capacity, each unit can be higher than the actual height required for collection. The dual cryosorption module system is illustrated by Figure 3-3. The cryopanels, of course, are not directly exposed to the energetic particles. The valves are designed to slide back and forth between two neighboring modules. One module can be closed for regeneration while the neighboring one is open for pumping. This dual particle collection unit and cryosorption module system allows for continuous collection and regeneration simultaneously without affecting the duty factor. Efforts to develop these concepts will be continued.

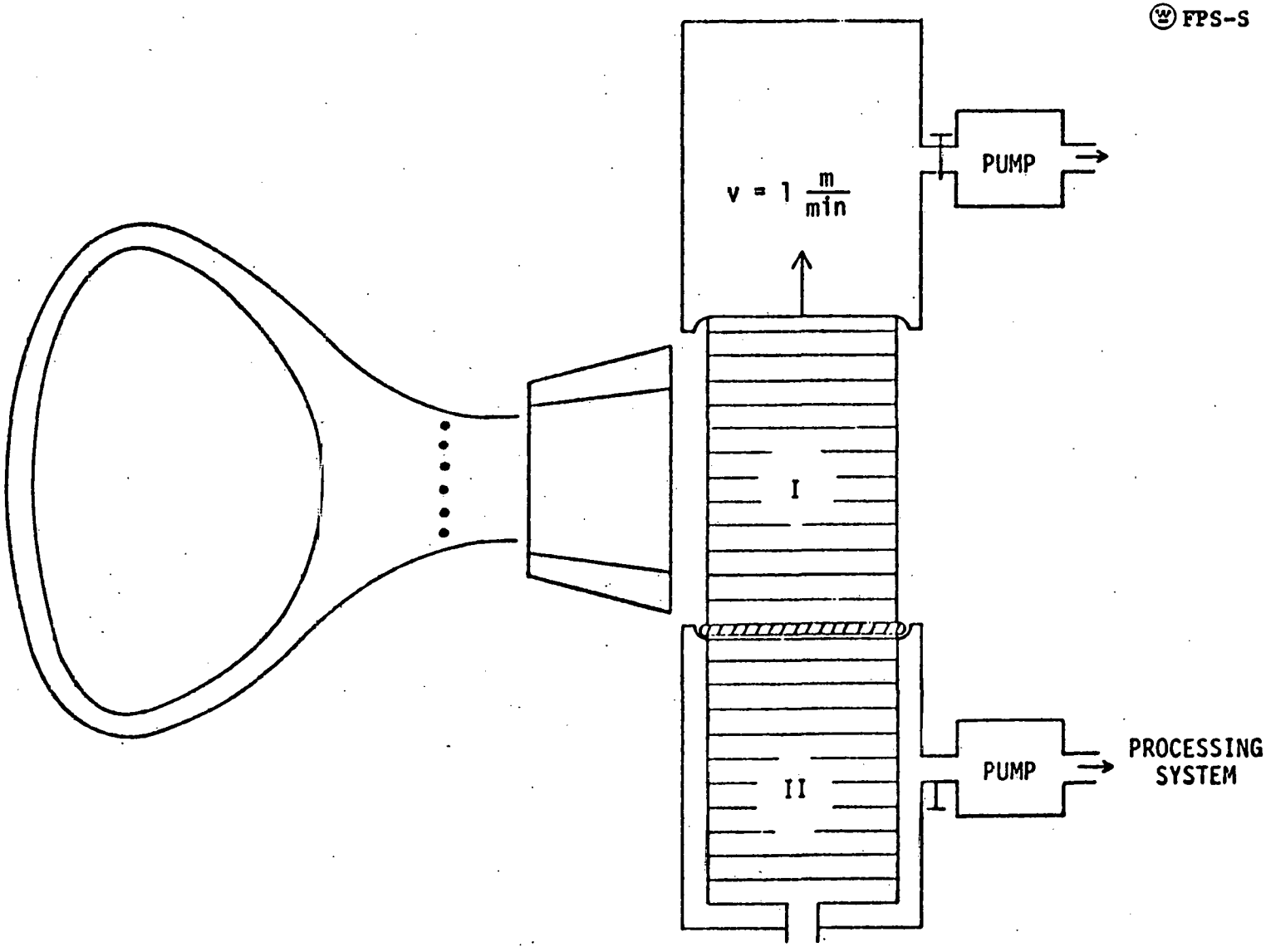

Figure 3-2. Side View of a Conceptual Dual Particle Collection and Regeneration System.

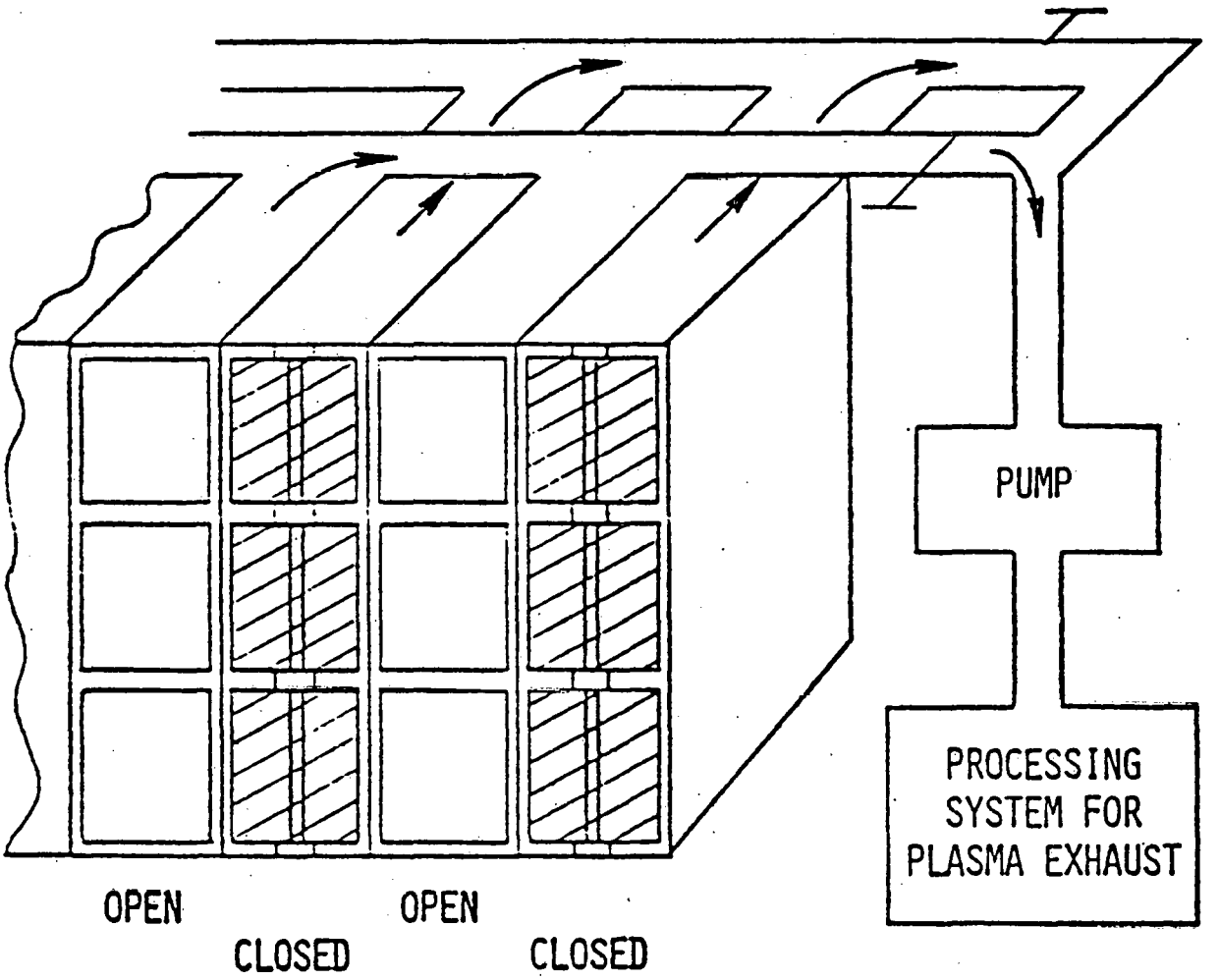

Figure 3-3. The Illustration of a Dual Cryosorption Module for Simultaneous Pumping and Regeneration.

Because of the front edge and peak density problem the effective trapping coefficient is smaller than 1; 90% is a reasonable value. To maintain an operating pressure of 10^{-5} τ we need approximately 90 m^2 of projected area of Zr/Al or cryopanel, and it is feasible to put 90 m^2 of Zr/Al getter system inside the chamber. The back flow can now be estimated as follows: the back flow ratio for hydrogen molecules is,

$$R_f = \frac{C\ (1 - S)}{C + S_A}$$

where C is the flow conductance of the divertor channel, S_A is the auxiliary pumping speed and s = 0.9, the effective trapping efficiency. The length of the divertor is about 3 m and the average diameter is 0.4 m. The flow conductance is about 7000 ℓ/s; therefore, R_f is less than 1%. S is assumed to be zero for helium and S_A is 10^6 ℓ/s. The back flow of helium is also less than 1%.

3.3 PLASMA SHEATH

There have been many concerns about the plasma sheath problem on the collector[21,22]. When the magnetic field lines pass through the collecting surfaces, the plasma will take in a positive potential relative to the surface because electrons are flowing toward the surface at a relatively high speed in view of their low mass. The plasma potential will build-up to the point where ion and electron losses are equalized, maintaining a constant plasma potential. This is the normal description of the formation of the Langmuir Sheath region that occurs at a plasma-electrode interface. Unipolar arcing then occurs when small hot spots occur on the wall. The spot vigorously emits electrons that flow back into the plasma. This electron current allows the plasma potential to fall below its original value, this in turn allows larger electron leakage currents from the plasma. Ultimately, a balance is set-up where the excess plasma electron current just matches the return current from the hot spot. This phenomena has been called unipolar arcing.

A suggestion here of dealing with this problem is to apply a small negative potential to the front tube to suppress the secondary electrons. This potential will also strip a fraction of the electrons from the plasma stream.

According to the same principle of direct energy conversion, the plasma will spread out due to the self-potential of positive charge before reaching the collecting surfaces. Theoretical and experimental work is needed to verify this concept. A direct conversion study is underway to examine these issues in more detail.

3.4 THE COLLECTOR EDGE PROBLEM

Along the separatrix the maximum field in the divertor channel is B_{max} = 7.6 T at R = 8.7 m and $\theta = \pm 6°$. The minimum field is B_{min} = 0.38 T at R = 11.7 m and $\theta = 0°$. The field at the edge of the collector is B_e = 1.4 T. Accordingly, the fields along the outside flux line are B'_{max} = 7.3 T, B'_{min} = 0.02 T, and $B'_e \cong$ 0.005 T. Applying the conservation of magnetic moment, $\mu = W_\perp/eB$, to the motion of the charged particles the $W_\perp$ on the collector is $W_\perp$ = 0.1 kT at the separatrix and $W_\perp$ = 0.002 kT at the outside flux line. The gyro-radii computed from

$$\rho = \frac{mV_\perp}{eB}$$

are 4 cm and 2 cm respectively. Therefore, the heat flux will spread out over the gyro-radius. The drift of a particle is harder to calculate and will be discussed in another work[23]. However, the sizes of the gyro-radii tell us that the plasma has to be continuous and diffuses across the field while in transit from the time of entering the divertor channel until reaching the collector. According to the same argument given in Section 3.1, we can write

$$\Delta'_d = \left(\frac{0.5}{16}\ \frac{kT}{eB}\ \frac{L_S}{\frac{1}{3}\sqrt{\frac{kT}{m}}}\right)^{1/2}$$

where L_S is the length of the half separatrix loop. Pessimistically assuming the maximum field B = 2.0 T, then

$$\Delta'_d = 12 \text{ cm}$$

Taking into account the fast weakening in B, this distance roughly agrees with the value of the gyro-radius. Therefore, the plasma does not sharply peak at

the surface of the separatrix and it should have a distribution as shown in Figure 3-4. The profile on the left side of the separatrix is exp $(-|x|/\Delta_d')$ and on the right side is exp $[-|x|/(\Delta_d + \Delta_d')]$ where $\Delta_d = 15\Delta$ is the projected characteristic length of the plasma in the scrape-off layer in the torus. Integrating over the projected collection area and normalizing to the total power the peak power density is found to be 4.0 kW/cm^2. This happens only at the ends of the front pipes near the separatrix. For thermal and stress analysis the heat flux distribution is averaged over the gyro-radius. It will be shown later that there is no difficulty with respect to heat transfer, but the effect on the material integrity due to nonuniform thermal stress is a problem. The front pipe is expected to require periodic replacement. As will be recommended later, advanced coolants, such as helium, sodium, or lithium, should be evaluated.

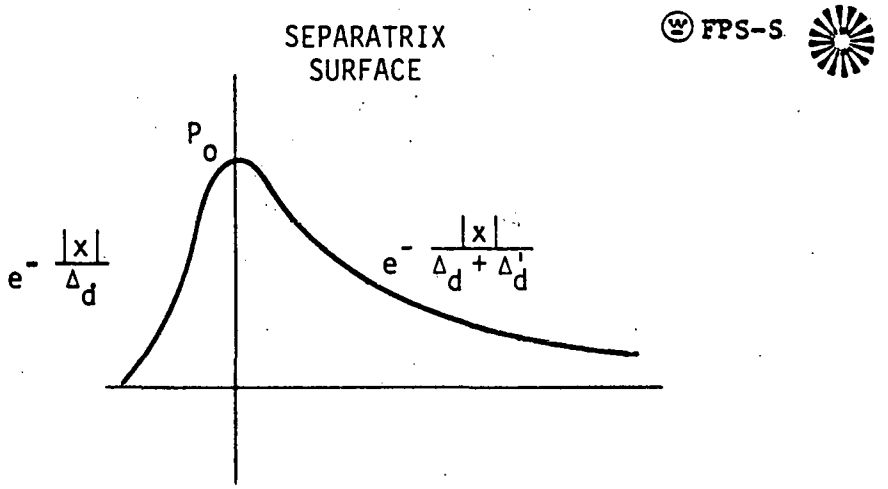

Figure 3-4. Plasma Power Profile on the Collector as a Spatial Function from the Separatrix.

4.0 MECHANICAL DESIGN

4.1 DIVERTOR COIL DESIGN

The trimetric view of DTHR in Figure 4-1 shows the perspective of the bundle divertor. The major components of the bundle divertor are located on the horizontal centerline of the reactor between two TF coils that are spaced 30° apart. The wider TF coil spacing is required to provide sufficient room for the divertor coils and their associated dewars and shielding.

The bundle divertor consists of two circular coils surrounded by a duct that is appended to the side of the reactor vessel. The duct terminates in a combination flange that can be bolted and seal welded to a mating closure. The mating closure which houses the bundle divertor collector system is a rectangular vessel flanged at one end and closed at the other. The rectangular vessel also contains collector discharge compartments located on top and bottom surfaces.

As is shown by Figure 4-2, the two circular divertor coils each consist of an assembly of 37 bobbins. Thirty-five of the bobbins each containing 12 conductors, and two bobbins each containing 6 conductors. The last one is a special two-piece bobbin that provides for double stacking of the 12 conductors over one-half its circumference. The double stacking arrangement provides for a narrower bobbin in the double stack region to provide space for more shielding. All bobbins are 3.5 cm thick and have a mean circumference of $\approx$ 8.33 m. There are 438 conductor turns per divertor coil. The conductor inside the jacket of a cable has a cross section area of 4 cm^2. Each coil assembly is superconducting and is enclosed in a separate dewar. Each assembly weighs approximately 18,600 kg.

In construction, that portion of the periphery of the divertor coil that is adjacent to the other divertor coil is supported by a curved structure containing notches to fit the bobbins. Each bobbin is fitted and bolted to the curved

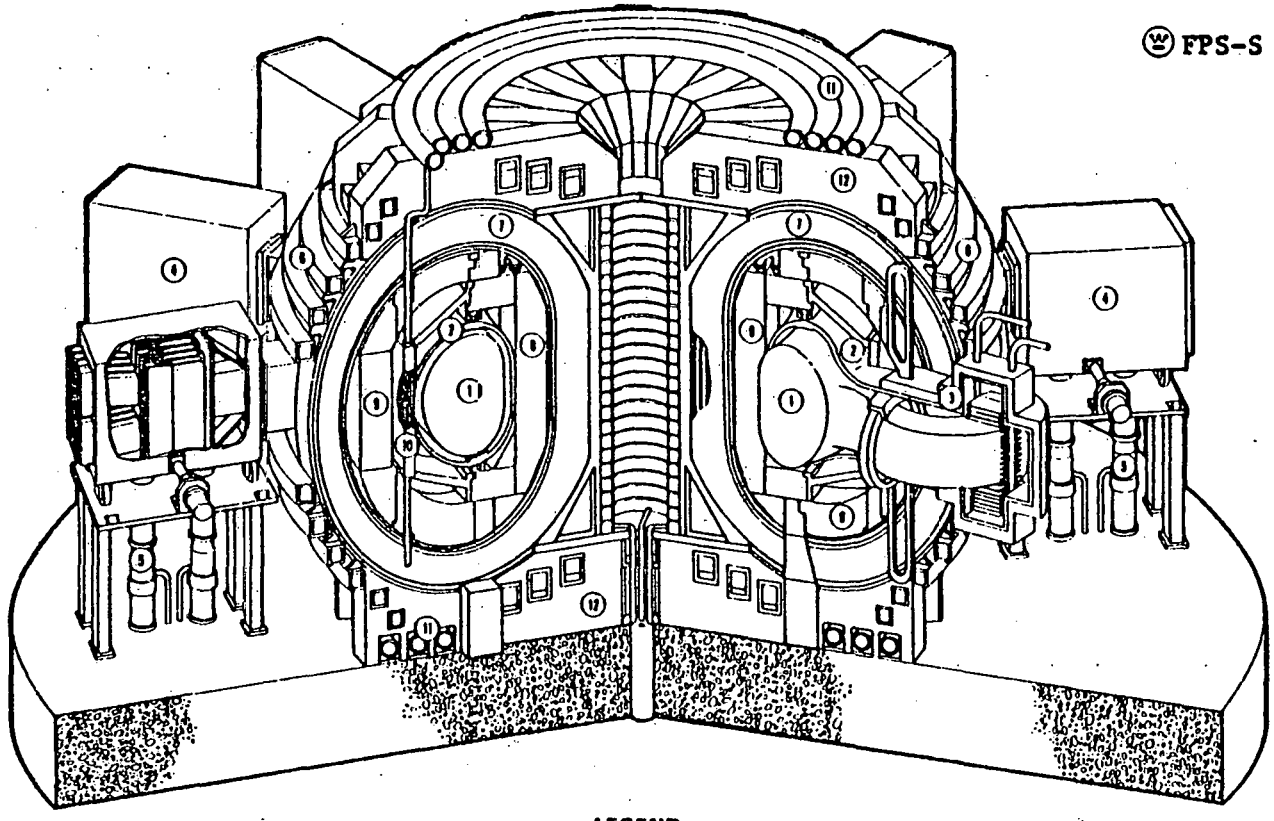

LEGEND

1 Plasma	7 Toroidal Field Coils
2 Vacuum Vessel	8 Inner Shield
3 Bundle Divertor	9 Outer Shield
4 Neutral Beam Injectors	10 Blanket Module
5 Vacuum Pumps	11 Cooling Headers
6 Poloidal Field Coils	12 Support Structure

Figure 4-1. Demonstration Tokamak Hybrid Reactor

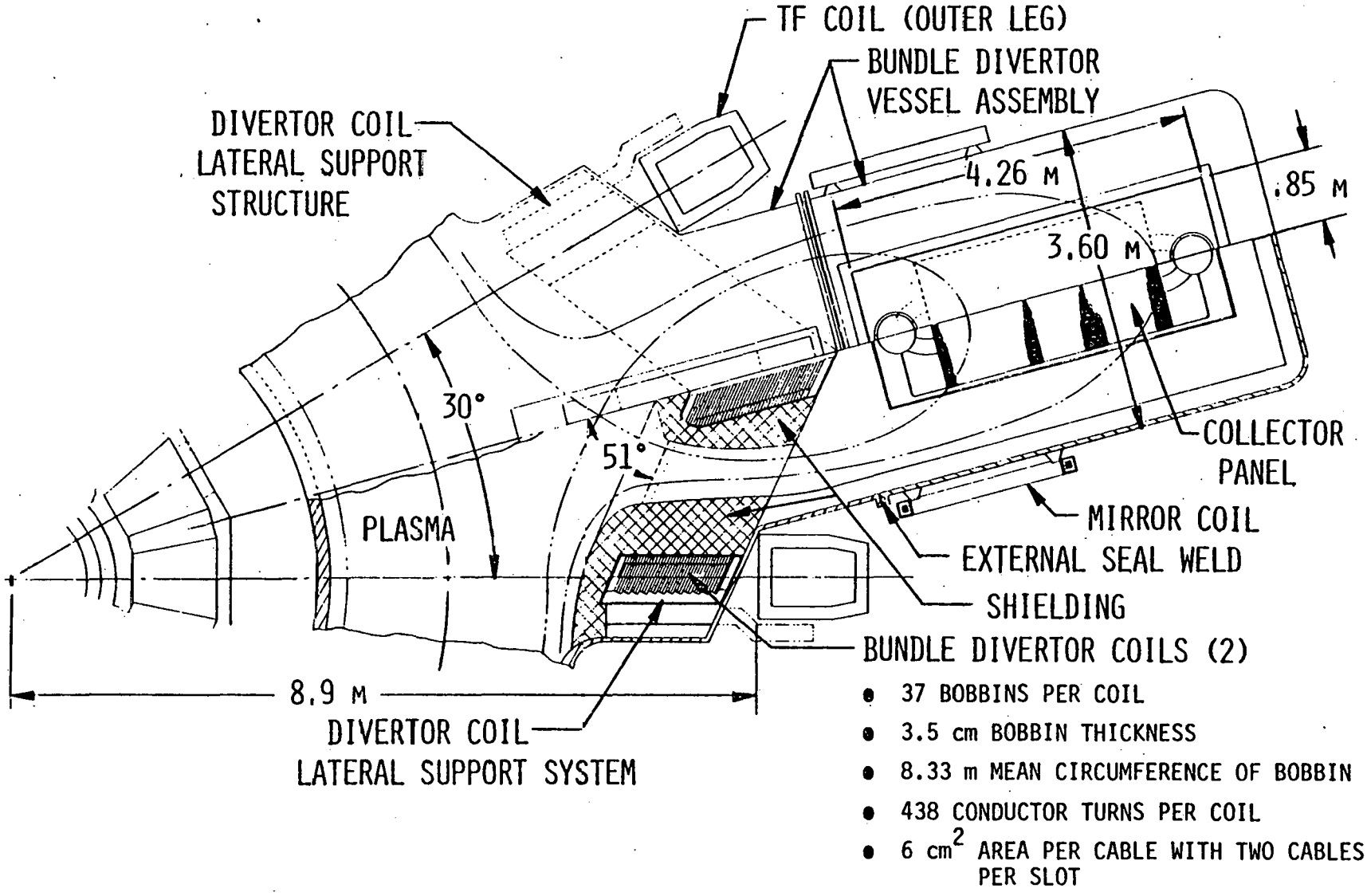

Figure 4-2. DTHR Bundle Divertor Plan View.

structure. When the two divertor coils are positioned in the divertor vessel duct, the curved support structures are adjacent to each other and provide a common horizontal support for both coils and their associated dewars. The coil bobbins are vertically supported and suspended within each dewar by additional hanger rods located at the top, bottom, and outer sides of the dewars (see Figure 4-3). The dewars in turn are mounted to base plates through support legs located around the lower periphery of the dewars. Half of the horizontal magnetic force produced by each divertor coil is transmitted to a structural beam located horizontally on the outside of the dewar. Two saw-toothed beams transfer the horizontal load from the bobbin plates through the dewar to the structural beam. The horizontal force on the structural beam is transmitted through the divertor vessel wall to external structures. The central half of the horizontal magnetic force produced by the divertor coils is transmitted to outside structures through eight keys located between the curved center support structures and the structural dewars of the top and bottom auxiliary coils.

Based on the Lorentz forces of 2.09 kN per linear cm of cable and F_Z = 1.59 kN per linear cm of cable for the conductors in the bundle divertor, the following conductor slot and tooth dimensions were developed. In the analysis, it was assumed that the coil bobbin structural material would be 304 stainless steel with a yield strength (S_y) or 407 MPa at 20 K and that two conductor cables, each measuring 2.45 x 2.45 cm on the outside, would be fitted into each support slot as shown in the sketch below. A factor of safety of two has been assumed in the analysis to permit the use of simplified equations and eliminate the need for stress concentration factors.

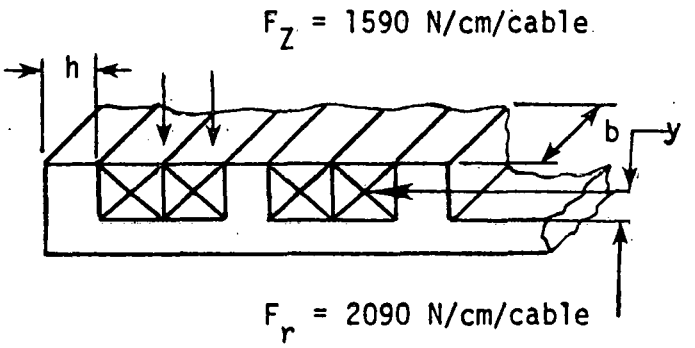

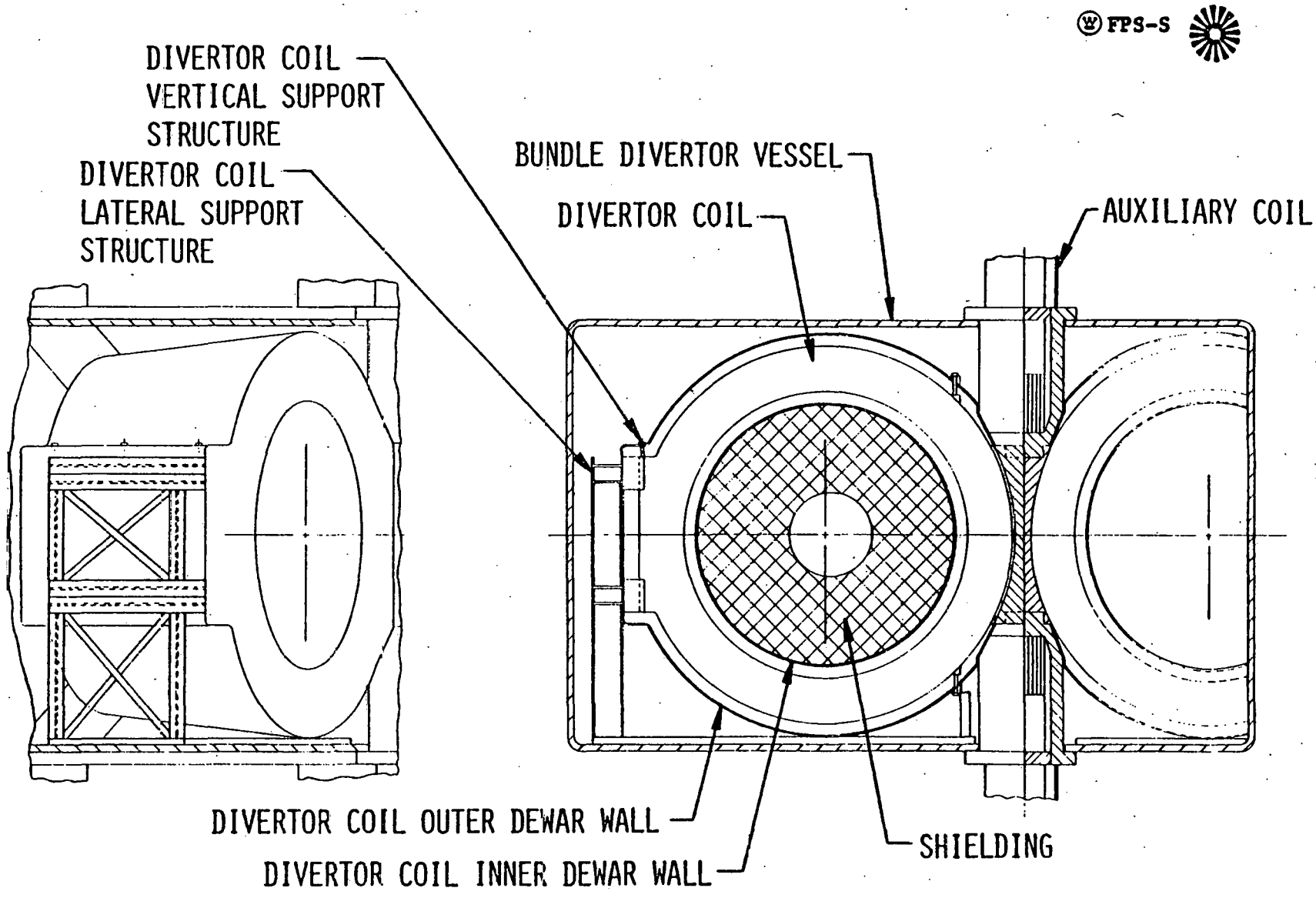

Figure 4-3. Bundle Divertor Coil Cut-Away Views.

The total horizontal design force, F_{rT}, resulting from the two cables on a single tooth is 2 F_r times the factor of safety and is equal to 8360 N per linear cm of cable. The bending moment at the base of the tooth is equal to this total design force times the moment arm y and is expressed by the equation

$$M = F_{rT} \times y = 8360 \times \frac{0.0245}{2} = 102.4 \text{ Nm}$$

The width of the tooth (h) is determined from the equation

$$\frac{I}{c} = \frac{bh^2}{6} \quad \frac{M}{S_y}$$

where $\frac{I}{c}$ the section modules and b = 0.01 m. Therefore,

$$h = \sqrt{\frac{6\,M}{S_y \times b}} = \sqrt{\frac{102.4 \times 6}{407 \times 10^6 \times 0.01}} = 0.012 \text{ m}$$

The width of the tooth needed to resist bending is 1.2 cm.

The shear stress at the base of the tooth is equal to the total design force divided by the area and is

$$S_S = \frac{F_{rT}}{A} = \frac{8360}{0.012 \times 0.01} = 69 \text{ MPa}$$

The area in shear is acceptable since the allowable shear stress for 304 stainless is taken as 0.5 of the yield strength and is equal to 203 MPa.

The thickness of the bobbin at the bottom of the conductor slot is based on bending between the bobbin teeth as shown in the following sketch.

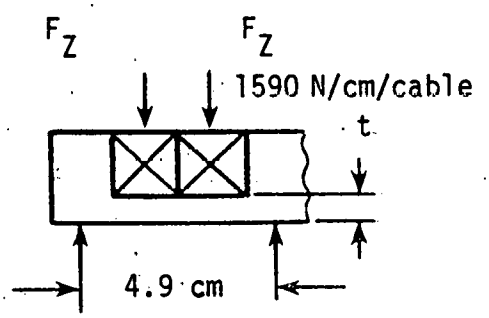

The load F for two cables is equal to two times the vertical force, F_Z, times the factor of safety, 2. The distance between supports is ℓ = 4.9 cm. The maximum bending moment equation equals

$$M_{max} = \frac{F\ell}{12} = \frac{1590 \times 2 \times 2 \times 0.049}{12} = 26 \text{ Nm.}$$

The required thickness (t) of the bobbin at the bottom of the slot is determined from the equation

$$t = \sqrt{\frac{6\,M}{S_y \times b}} = \sqrt{\frac{26 \times 6}{407 \times 10^6 \times 0.01}} = 0.0062 \text{ m}$$

The thickness of the bobbin at the bottom of the conductor slot is therefore conservatively selected as 1.0 cm.

Basic sizing of the vertical and horizontal bobbin support rods and keys for restraining the dead weight and magnetic force were determined using the following design stress limitations.

- Weight of each coil including bobbins, conductors, and dewar is approximately 18,600 kg.
- Horizontal magnetic force on coils = 44 MN.
- Rotational magnetic forces per coil is 124 MN m.
- Material design stress limitations:
  310 Stainless Steel @ 4 K S_y = 817 MPa ; S_S = 408 MPa
- Factor of safety = 2

In sizing the vertical supports to carry the weight of each coil, the 10,600 kg is resolved into two reactions, R_1 and R_2. Using the $\Sigma F_v = 0$, as shown in the sketch, the reactions R_1 and R_2 are equal to 1/2 W, which is 9300 kg or 91,140 N.

Each R_1 reaction is taken by two tension rods supporting the bobbins through the dewar. The diameter of the tension rods based on 310 stainless steel and a factor of safety (FOS) of two is derived from the following equaiton

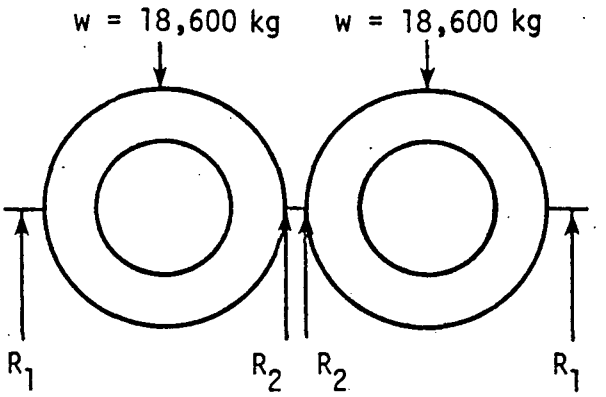

$$D = \sqrt{\frac{4A}{\pi}} = \sqrt{\frac{4}{\pi}\left(\frac{\frac{1}{2} W \times FOS}{2\ S_y}\right)} = \sqrt{\frac{4}{\pi}\left(\frac{\frac{1}{2}\ 91140 \times 2}{2 \times 817 \times 10^6}\right)}$$

$\therefore$ D = 0.0119 m diameter

The diameter for each of the two tension rods is 1.2 cm.

The R_2 reaction is also taken by similar tension rods. The structural dewars of the auxiliary coils and saw tooth beams are used to restrain the horizontal magnetic forces of the coils.

The magnetic force on the divertor coils consists of a horizontal force, F_H = 44 MN and a rotational torque T_y = 124 MNm about the vertical axis y as shown on the sketch.

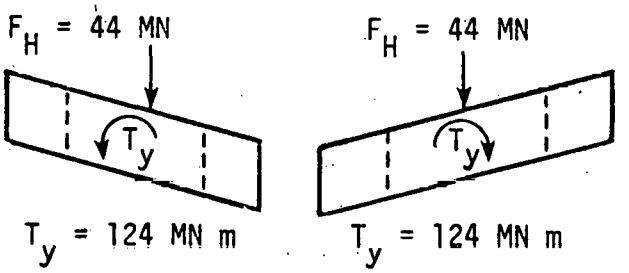

Translating the rotational torque, T_y = 124 MNm into a couple using a moment arm of 1.15 m yields two horizontal forces acting in opposite directions. The magnitude of each force is

$$F = \frac{124 \times 10^6 \text{ Nm}}{2\ (1.15 \text{ m})} = 53.9 \text{ MN}$$

These forces react on the coil as shown in the following sketch.

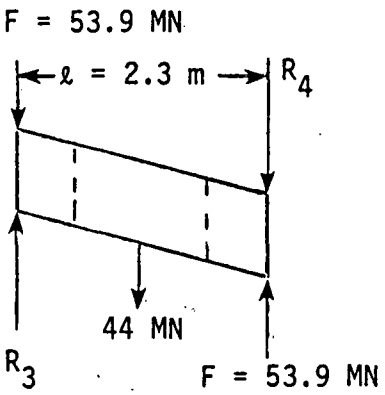

Setting $\Sigma M=0$, the resulting horizontal reactions R_3 and R_4 are determined by,

$$\Sigma M = 44 \times 10^6 \times \frac{\ell}{2} - 53.9 \times 10^6 \times \ell + R_4 \times \ell = 0.$$

Therefore, R_4 = 31.9 MN and R_3 = 75.9 MN.

Each R_3 reaction is taken by two saw-toothed beams. Each beam has 12 teeth with each tooth supporting three bobbins of the coil as shown in the sketch.

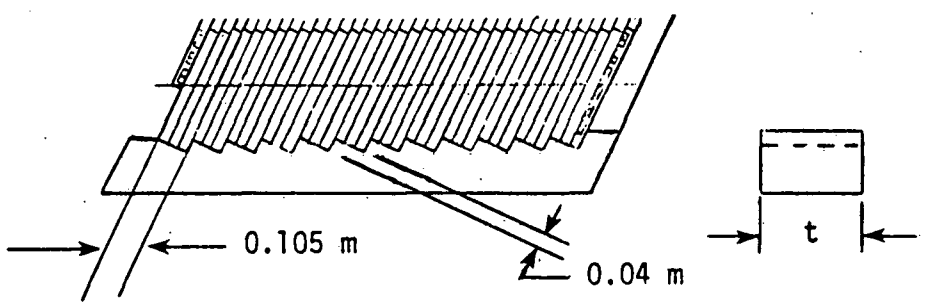

With a tooth length of 0.105 m and a reaction force, R_3 equal to 75.9 MN, the thickness of the tooth (beam width) based on a shear stress of 408 MPa is

$$t = \frac{R_3 \times FOS}{0.105\ S_S \times 24} = \frac{75.9 \times 10^6 \times 2}{0.105 \times 408 \times 10^6 \times 24} = 0.147 \text{ m.}$$

The R_4 reaction is taken by keys which connect the top and bottom surfaces of the curved center structure of the coil bobbin assembly to the structural dewars of the auxiliary coils.

The reaction from both coils is $2 \times R_4 = 63.8 \times 10^6$ N which is resisted by a total of eight keys, four keys on the top auxiliary coil and four keys on the bottom auxiliary coil. Each key is 30.5 cm long. The thickness of the keys required to resist the shear forces is determined for 310 stainless steel with a factor of safety equal to two, using the equation

$$t = \frac{A}{\ell} = \frac{1}{\ell}\left(\frac{F_h \times FOS}{8\ S_S}\right) = \frac{1}{0.31}\left(\frac{63.8 \times 10^6 \times 2}{8 \times 408 \times 10^6}\right)$$

$\therefore$

$$t = 0.126 \text{ m}$$

The thickness of each key is 12.6 cm.

The thickness of the side plates of the two auxiliary coil dewars is determined by using the force transmitted through the keys as shown on the sketch.

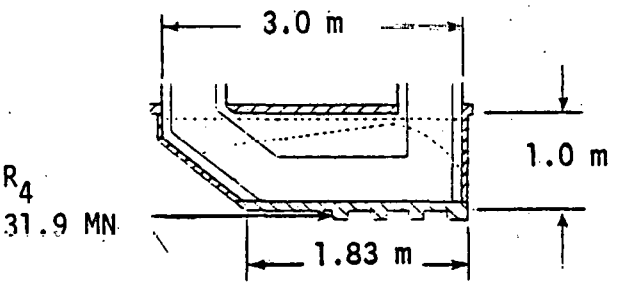

The bending moment on the side plates is equal to the R_4 reaction times, the vertical moment arm of 1.0 m and the factor of two safety.

The bending moment is

$$M = R_4 \times 2 \times 1.0 = 31.9 \times 2 \times 1 = 63.8 \text{ MNm.}$$

The thickness (B) of the dewar side plate is computed from

$$B = \frac{6\,M}{2\,S_y h^2} = \frac{6 \times 63.8 \times 10^6}{2 \times 817 \times 10^6 \times 3^2} = 0.059 \text{ m}$$

The thickness (B) of each side plate is 0.059 m.

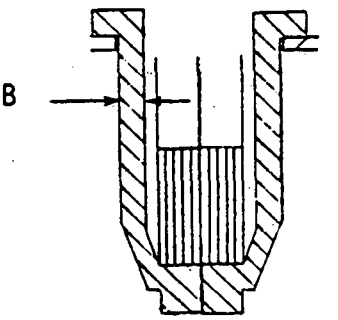

The shear stress on the side plates in the area of the four keys is calculated by the equation

$$S_S = \frac{P}{A}$$

where P is equal to the R_4 reaction time the factor of safety two and the area is equal to 0.118 m, the thickness of two plates, times a length of 1.83 m.

Substituting these values in the equation, the stress

$$S_S = \frac{P}{A} = \frac{31.9 \times 10^6 \times 2}{0.118 \times 1.83} = 295 \text{ MPa} .$$

Therefore, the thickness of the dewar plate is acceptable in shear as the allowable shear stress for 310 stainless is 408 MPa.

Two auxiliary divertor coils, divided into two parts, are located vertically above and below the main divertor coils. The two-part design provides space for the poloidal coils (see Figure 4-4). Each part of the auxiliary coil consists of ten parallelogram shaped bobbins each 3.0 cm thick and containing five conductor slots. Each conductor slot supports four conductors of the same size and shape used in the main divertor coils. The auxiliary coils have a total of 200 superconducting cables and are designed with individual dewars.

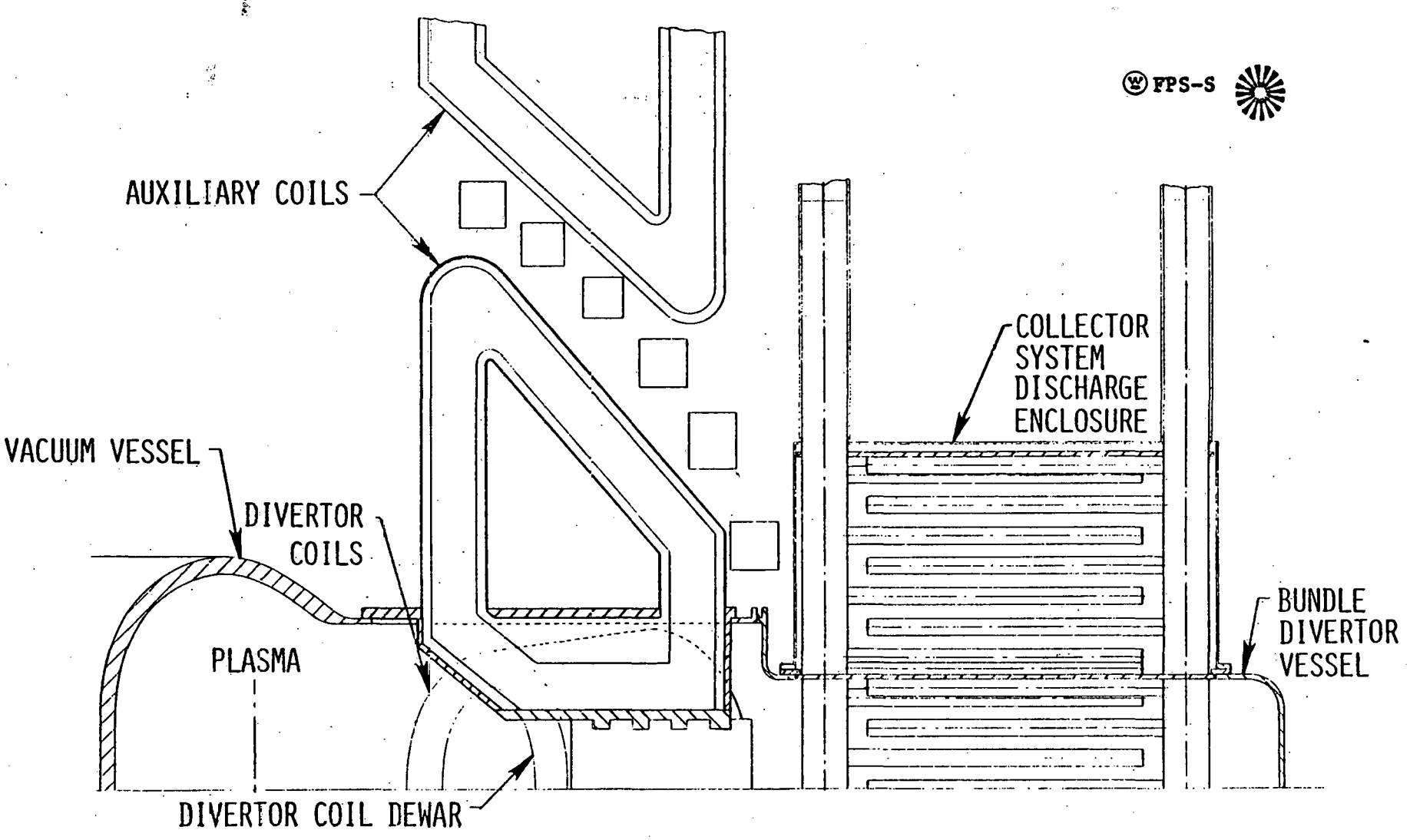

Figure 4-4. Bundle Divertor Side Elevation.

The outer part of the two-part auxiliary coil, that is, the part furthest from the divertor coils, is mounted to a structure supported by the adjacent TF coils. The inner part, or part closest to the divertor coils, is provided with a horizontal flange for mounting to the divertor vessel. The divertor vessel duct directly above and below the main divertor coils has rectangular openings to receive that portion of the auxiliary coil extending inward beyond the mounting flange. When the auxiliary coils are installed and the flanges seated on the divertor duct, that portion of the auxiliary coil dewar extending inside the divertor vessel duct is keyed to the curved center support structure of the two main divertor coils. The flange is clamped and seal-welded to the divertor vessel duct.

Included as part of the bundle divertor are two mirror field coils which are mounted on each side of the divertor collector system vessel. The mirror field coils are used to further shape and direct the flux path into the collector panels. Each coil is made up of three circular bobbins with a mean diameter of 2.0 m and contain a total of six conductors of the same size and shape as those used in the main divertor coils.

4.2 DIVERTOR COLLECTOR ASSEMBLY DESIGN

As is shown by Figure 3-1, the divertor collector assembly consists of a series of panels 1.0 m wide by 2.76 m long. The panels are arranged in a saw-tooth pattern such that the overall arrangement of the collector assembly is accordion shaped. The construction of the collector panels uses a 2.0 m length of 0.95 cm diameter copper tube bent at the mid-point to form a Vee with a 1.27 cm bending radius at the apex of the Vee. Two hundred ninety-two of the formed tubes are then stacked side by side and stitch welded to form two panels, one for each side of the Vee. The panels thus formed are of tubular construction for coolant and have a rippled surface to increase the total surface area.

Seven of the Vee shaped panels are assembled together in saw-tooth fashion by joining the open end of two adjacent Vee panels to a common manifold. The pipe shaped manifold is sized to equal twice the number of tubes in one panel since each manifold is serving two panels. A second set of seven Vee shaped

panels are assembled in the same manner and the two assemblies are then interlaced to form a double saw-tooth pattern. The inlet and outlet pipe manifolds are connected to a manifold located vertically at each end of the Vee shaped panels. To make the design practical a two-phase operating cycle was selected. In the first phase the collector panels are located such that they trap the particles from the plasma and in the second phase the collector panels are moved to a discharge area where the collector panels are discharged by a heating and pumping process. To accomplish this a second assembly of double saw-tooth panels is employed. The two units are stacked together with a solid plate mounted between the stacks. Similar solid plates are attached at the top and bottom of the assembly. As noted earlier, collector discharge compartments are located on the top and bottom of the bundle divertor collector vessel. The collector panels are mounted to a device that mechanically moves the assembly up and down periodically. The solid end plates and the plate mounted on the mid-plane of the assembly engage with metal seal rings located in the top and bottom sections of the divertor housing. This arrangement isolates the plasma region from the top and bottom collector discharge compartments or degassing chambers. Such a cycling method is demonstrated by the Figures 3-2, 4-1, and 4-4.

A secondary cooling tube and fin arrangement is installed in front of the leading edge of each Vee shaped collector panel (Figure 3-1 exploded view). The tubes are hydraulically connected to the vertical inlet and outlet manifolds by extended piping and necessary fittings. The purpose of this secondary cooling tube and fin is to reduce the thermal load and erosion to the radiused edge of the Vee panel and provide a replaceable unit less costly than the tubular constructed collector panels.

4.3 ALTERNATE COLLECTOR ASSEMBLY DESIGNS

Two alternate divertor collector panel designs have been developed as part of this study. In one system (see Figure 4-5), 348 tubes 0.79 cm diameter one-half meter long are used to make up a Vee shaped panel. All the tubes are attached to a small 1.59 cm diameter manifold located at the apex of the Vee. Alternately, half of the tubes are directed in one direction of the Vee leg

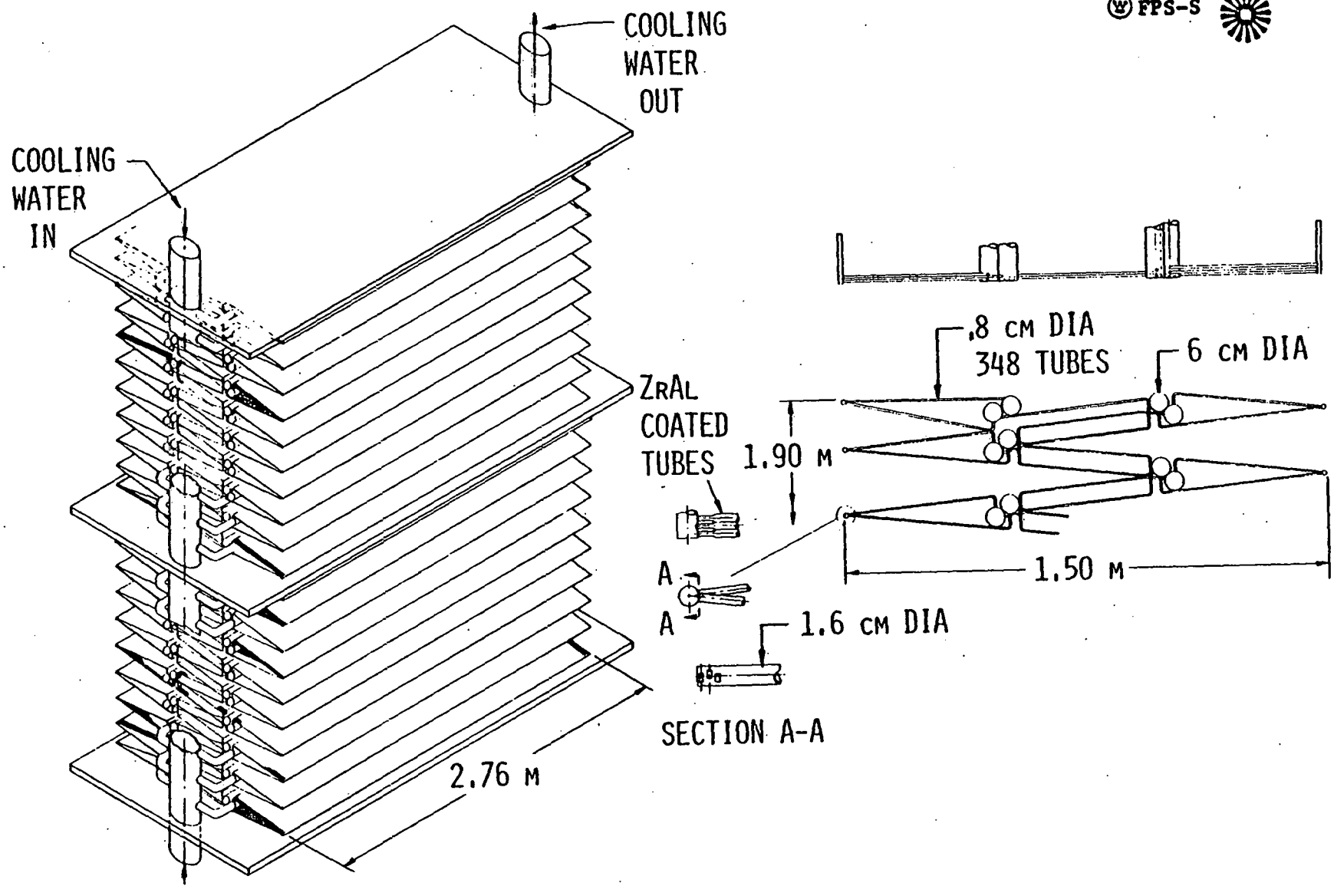

Figure 4-5. Collector System (Alternate Scheme I).

while the other half is directed in the other direction of the Vee leg. As a result, each panel of the Vee structure contains only 174 tubes with a space of one tube diameter between each tube. The tubes at the open end of the Vee terminate into a pipe-like inlet and outlet manifold. The panel dimension for this structure is 2.76 m long by 0.5 m wide. In order to maintain an effective panel width of 1.0 meter a second array of tubes is needed. In this case, 174 of the same diameter tubes one meter long are bent at the mid-point in the form of a modified Vee. The open ends are connected into the same inlet and outlet pipe manifolds. The width of the modified Vee at the apex is equal to the width of the first Vee structure at the manifold end. The ends of the tubes terminating into manifolds are bent as required to locate the manifolds inside the area prescribed by the boundaries of the Vee. These assemblies are then assembled in double saw-tooth fashion similar to the divertor collector panel design explained in the above paragraphs. While this concept has less tubes with intermittent spaces, the contact area for trapping the particles is the same. In this case, those particles that pass between tubes on one panel are intercepted by the back-side of the tubes in the adjacent panels. This scheme is intended to give a better heat distribution and more uniform thermal loading to the tubes.

The second alternate divertor collector panel design uses a tube within a tube as the return path for the coolant which is shown in Figure 4-6. Since the one end of the outer 1.27 cm diameter tube is capped off, no return bend or manifold is needed at this end of the tube. The two hundred fifty-four outer tubes 0.54 m long are placed side by side to form a panel of tubular construction 3.23 m long by 0.54 m wide. The open ends are fitted radially to an inlet pipe manifold. The inner tube is centered and supported inside the larger tube by a wire helixed over the inner tube. The end of the inner tube extending beyond the outer tube passes diametrically through the inlet manifold and terminates into an outlet manifold that parallels the inlet manifold. The helixed wire also provides a swirl path for the coolant. In this design, every other double tube assembly is forshortened sufficiently to enable the leading edge of two panels to interlace in the apex region of the Vee formed by the two panels. A similar set of tube panels are located behind and in line with the foremost panels to provide a total panel width of 1.08 m. This

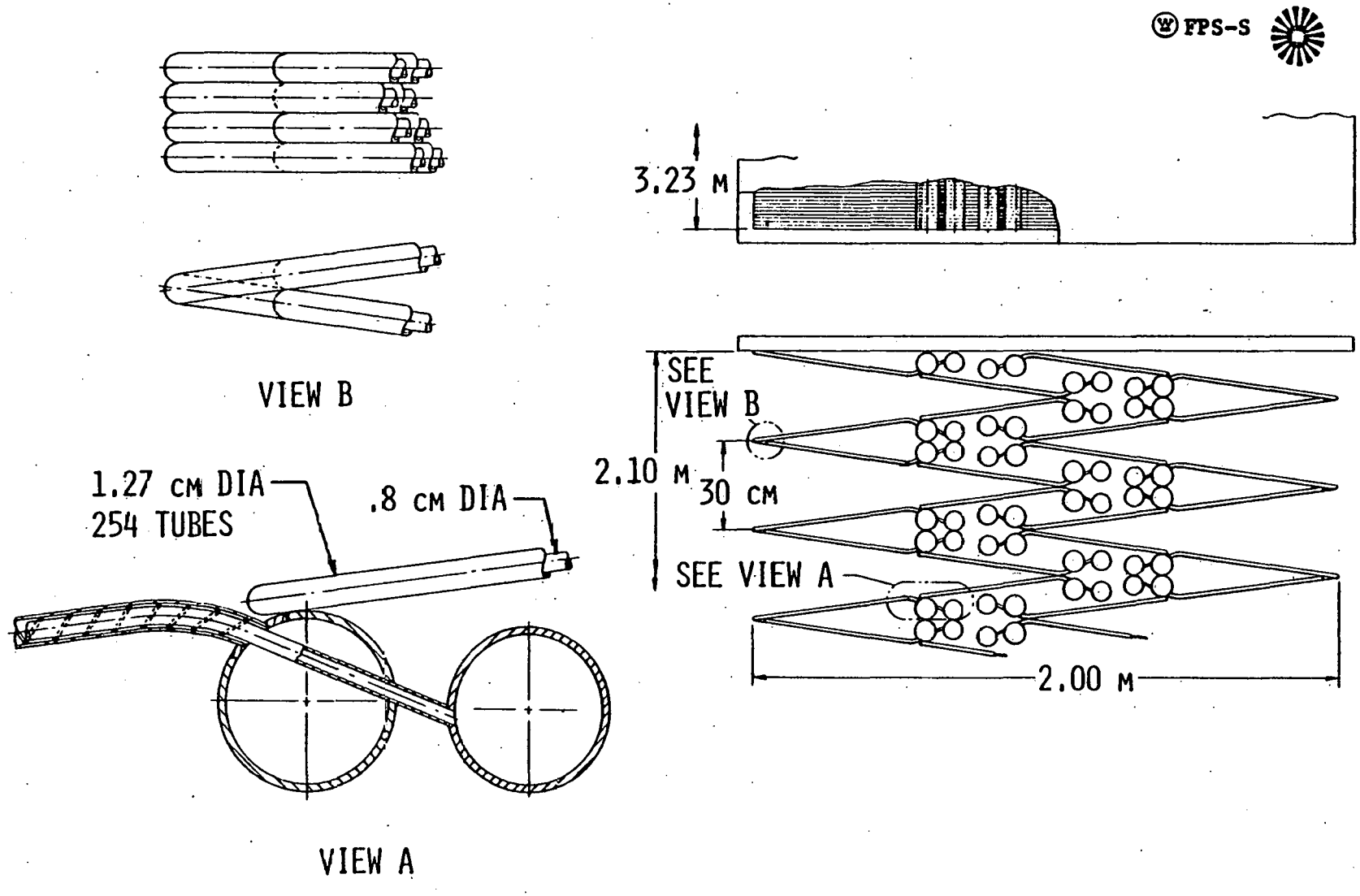

Figure 4-6. Collector System (Alternate Scheme II).

array of panels and associated inlet and outlet manifolds are arranged in the same double saw-tooth pattern to complete the divertor collector panel assembly. This design is intended to eliminate the leading curved portion of the one-piece Vee tube design. While both alternate collector panel designs appear to be mechanically feasible, more detailed strength, thermal, and hydraulic calculations are required.

4.4 DIVERTOR COIL MAINTENANCE

The location of the bundle divertor outside the reactor blanket area and between a pair of TF coils is one of the key features of the bundle divertor concept. The degree of maintainability of this type of divertor is dependent on whether the coils of the divertor are located outside or inside the vacuum vessel duct which joins the bundle divertor collector system to the reactor vessel. Both coil locations have been investigated with this concept.

Servicing and maintenance of the bundle divertor is found to be much more difficult when the coils are located outside the vacuum vessel duct. In the earlier design, shown by Figures 4-7 and 4-8, the coils were mounted external to the divertor vacuum vessel duct and removal of the divertor coils required the coil dewar be disassembled and the coil dismantled so that one bobbin at a time could be threaded out between the TF coils and the divertor coil vacuum vessel ducts. The earlier design also required that the divertor coil shielding be removed prior to removal of the coils. This sequence of disassembling under irradiated conditions would be time consuming and require complicated handling equipment.

In the present design, as is shown by Figure 4-2, the divertor coils and associated dewar and shielding are removed as a complete unit once the divertor collector panel system vessel is removed. Each coil assembly, mounted on a base plate, is moved radially outward through the opening in the divertor vessel duct. As one coil is moved radially outward, it is rotated about a vertical axis such that the coil will clear the divertor vessel housing that extends inside the TF coil space envelope.

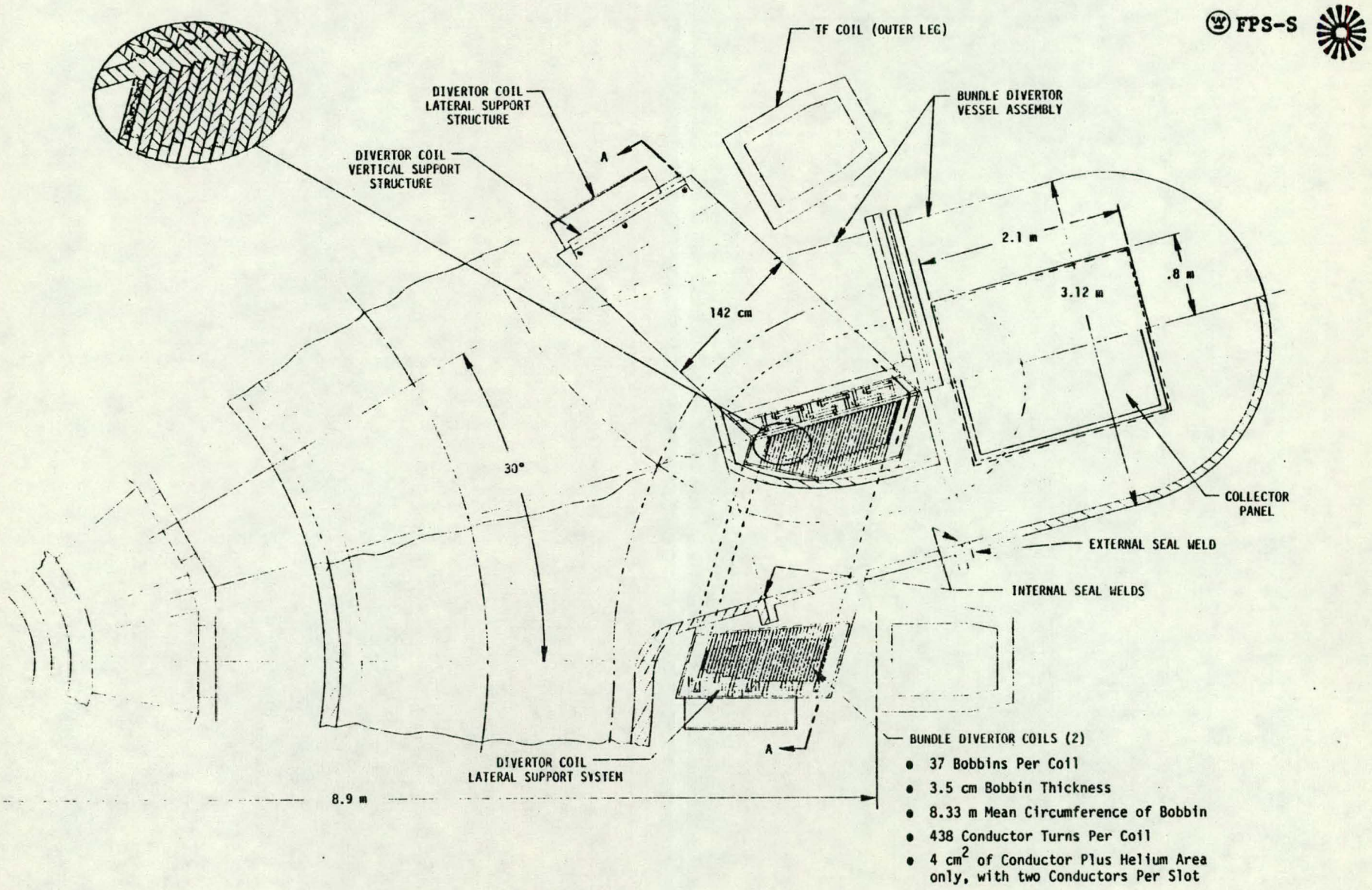

Figure 4-7. DTHR Bundle Divertor Concept Plan View when the Coils are Outside the Vacuum Vessel.

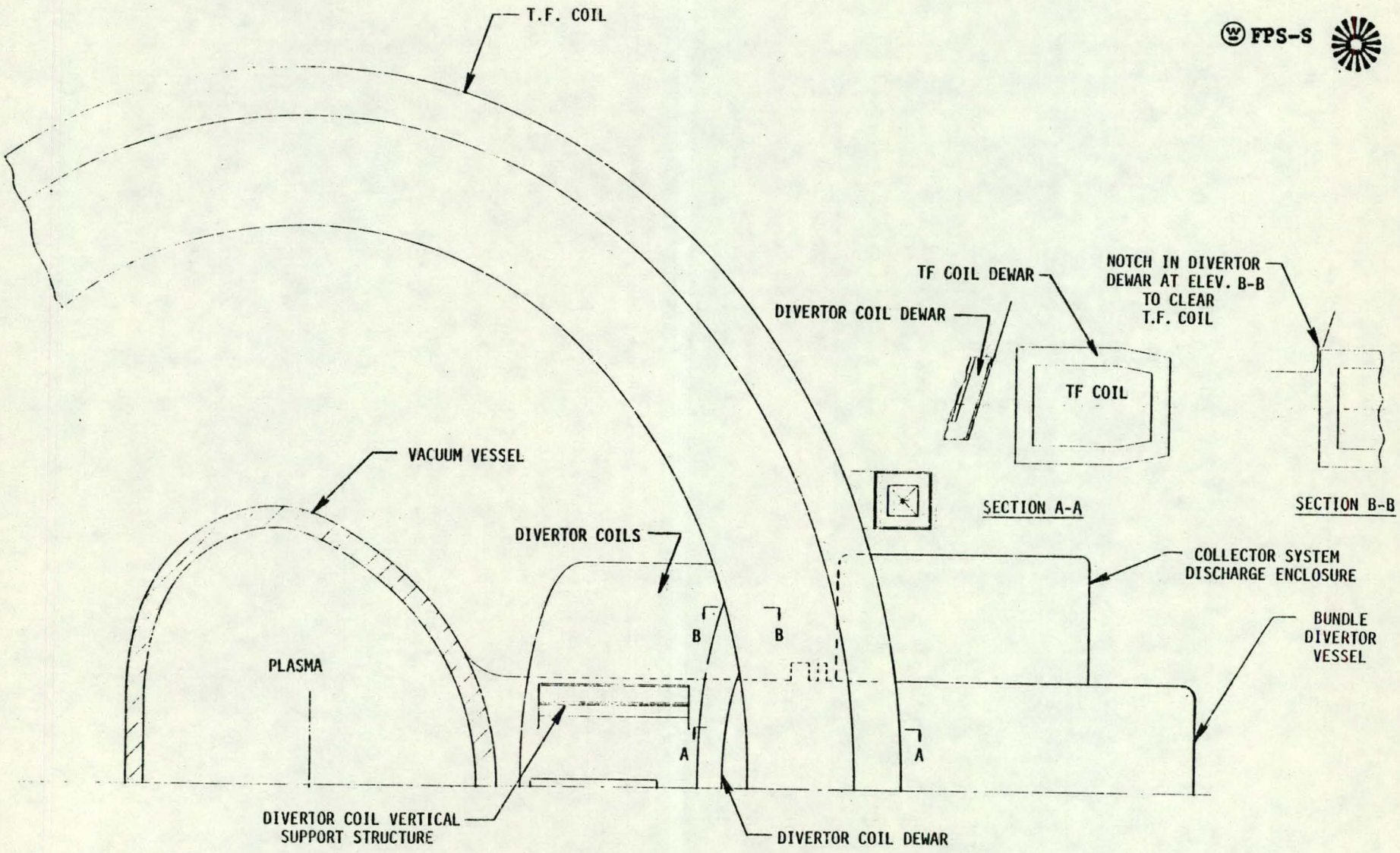

Figure 4-8. DTHR Bundle Divertor Concept Side Elevation for the Divertor Coils Outside the Vacuum Vessel.

Removal of the second divertor coil is accomplished by translating it on its base to the center of the divertor vessel duct opening and then moving it radially out through the opening. Figure 4-9 shows a sequence of steps necessary to remove the divertor coils from the divertor vessel after the divertor collector system housing is removed. Servicing of the divertor collector system is accomplished by removal of the upper or lower collector discharge compartments without any additional removal of reactor components.

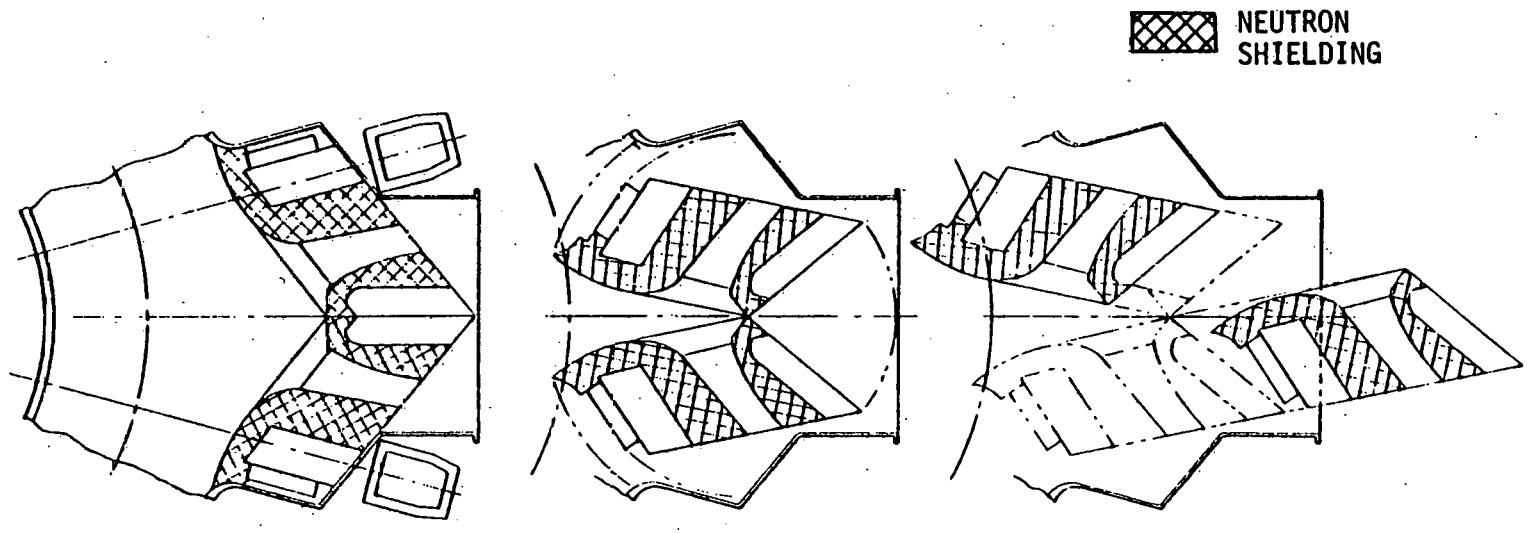

Figure 4-9. DTHR Bundle Divertor Coil Removal Sequence.

5.0 CRYOGENIC DESIGN OF THE DIVERTOR MAGNETIC COIL

The magnetic coils for the bundle divertor are to be superconducting to reduce the power supply system and operating costs. Recent advances in the design and development of the Nb_3Sn superconductors for high field operation have made their application to the divertor coils possible. The peak field at the divertor coils is 10 tesla and the required ampere-turns is 14×10^6. The details of the magnetic field distribution of the coil have not been defined at this time. For the purpose of this analysis the coil is assumed to be divided into two equal zones. The zone near the plasma is taken to be operated at ten tesla and the other at seven tesla. Multi-filamentary and cabled Nb_3Sn plus copper composites are used as the conductors. The cables are to be cooled by forced-flow supercritical liquid helium. Since the conductors are to be wound radially and the zones are divided axially, two conductor designs can be used with one design at one zone to save superconductor and refrigeration costs. The thermal design of the superconductors and the refrigeration loads are described in the following subsections.

5.1 SUPERCONDUCTOR DESIGN PARAMETERS

As discussed in Section 4.0, there are two circular coils in the divertor. Each coil consists of 37 bobbins. There are six slots in one bobbin and two conductors are wound inside one slot. Hydraulically, the two conductors in each bobbin are to be cooled in parallel. The coolant would enter the channel from the inner bore of the coil and exit at the outer bore. There will be a total of 74 parallel conductor cooling channels in one coil. The length of the channel is about 50 m consisting of six turns (see left side bobbin in Figure 5-1).

The conductor plus helium area and the coolant flow area fraction were selected to be 4 cm^2 (2 x 2 cm) and 0.35, respectively. The selection of these and other conductor parameters are mostly based on the results of superconductor design study performed for the Large Coil Program and reported in Reference 22. The rationale for selecting the various design parameters are given in detail

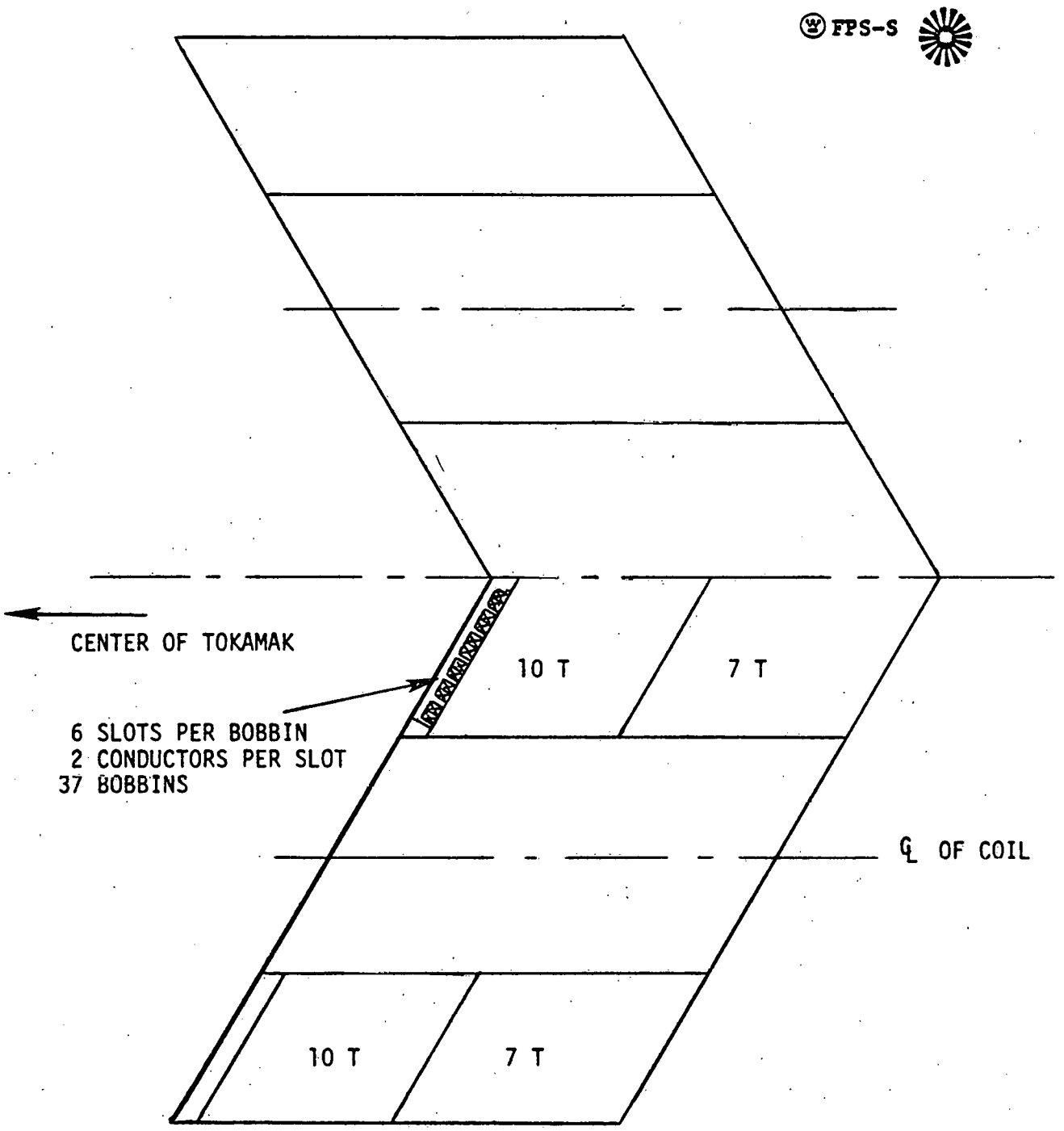

Figure 5-1. Oversimplified Divertor Coil Model for Cryogenic Design.

in the reference. They will not be reiterated in this report. A feasible coil and superconductor configuration suitable for the bundle divertor operation at 10 tesla is shown in Table 5-1. The conductor to operate at seven tesla is shown in Table 5-2.

Because of the limited space available for the coils, the transport current was taken to 32 kA as shown in the tables. With this high operating current, cryostability of the superconductor is a major design requirement. The transient cryostability analysis was performed using a "zero-dimensional" thermal model. With this model, the transient heat balance equations of the conductor composite and of the helium coolant were solved to determine from what initially driven normal temperature the conductor can freely recover its superconductivity at various coolant flow rates. The results are shown in Figure 5-2. In this figure, the maximum recoverable initially imposed normal temperatures are plotted against the helium flow rate per conductor channel. The recovery capabilities of the ten tesla and the seven tesla cables are shown in the figure. Any initial normal temperature above the solid lines indicates a thermal-runaway condition. At any initial normal temperature below the solid lines the conductor can fully recover its superconductivity. For the ten tesla conductor the helium flow rate has to be at least 8 g/sec before it can recover from an initial normal temperature above 15 K. Below the flow rate of 8 g/sec it can only recover from a temperature at the current sharing region. The nominal operating coolant flow rate for this ten tesla conductor was, therefore, selected to be 8 g/sec per conductor for cryostable operations. Similarly, the nominal operating coolant flow rate for the seven tesla conductors was selected to 3 g/sec per conductor for cryostable operations. The seven tesla conductors not only require less coolant flow, but also possess higher recovery capability than the ten tesla conductors.

After the detailed magnetic field distribution is better defined, the coil could be divided into more than two zones according to the field distribution. In this way, greater savings in superconductor cost and coolant requirements can possibly be realized.

TABLE 5-1

PRELIMINARY SPECIFICATIONS FOR THE MAGNETIC COIL AND THE Nb_3Sn SUPERCONDUCTORS FOR THE DTHR BUNDLE DIVERTOR OPERATED AT 10 TESLA

SUPERCONDUCTOR	Nb_3Sn + BRONZE + COPPER
PEAK MAGNETIC FIELD	10 TESLA
TOTAL AMPERE-TURNS	14×10^6
NUMBER OF COILS	2
NUMBER OF BOBBINS PER COIL	37
SLOTS PER BOBBIN (NORMAL)	6
NUMBER OF CONDUCTOR PER SLOT	2
TOTAL NUMBER OF TURNS PER COIL	438
MEAN COIL CIRCUMFERENCE	8.33 m
STRUCTURE-TO-CONDUCTOR RATIO	1.2
CONDUCTOR PLUS He AREA	4 cm^2
VOID FRACTION FOR COOLANT FLOW	0.35
J OPERATING/J CRITICAL	0.5
NUMBER OF STRANDS PER CONDUCTOR	567 (ALL ACTIVE)
STRAND DIAMETER	0.0764 cm
SUPERCONDUCTOR OPERATING CURRENT DENSITY	150,000 A/cm^2
Cu-TO-NON Cu AREA RATIO	1.54
NON Cu CURRENT DENSITY	31,250 A/cm^2
TRANSPORT CURRENT	32 kA
HELIUM COOLANT INLET TEMPERATURE	4.2 K

TABLE 5-2

PRELIMINARY SPECIFICATIONS OF Nb_3Sn SUPERCONDUCTORS
FOR DTHR BUNDLE DIVERTOR OPERATED AT 7 TESLA

PEAK MAGNETIC FIELD	7 TESLA
CONDUCTOR PLUS He AREA	4 cm^2
VOID FRACTION FOR COOLANT FLOW	0.35
J OPERATING/J CRITICAL	0.5
NUMBER OF STRANDS	567
STRAND DIAMETER	0.0764 cm
SUPERCONDUCTOR OPERATING CURRENT DENSITY	285,000 A/cm^2
Cu-TO-NON Cu AREA RATIO	3.82
NON Cu CURRENT DENSITY	59,375 A/cm^2
TRANSPORT CURRENT	32 kA
HELIUM COOLANT INLET TEMPERATURE	4.2 K

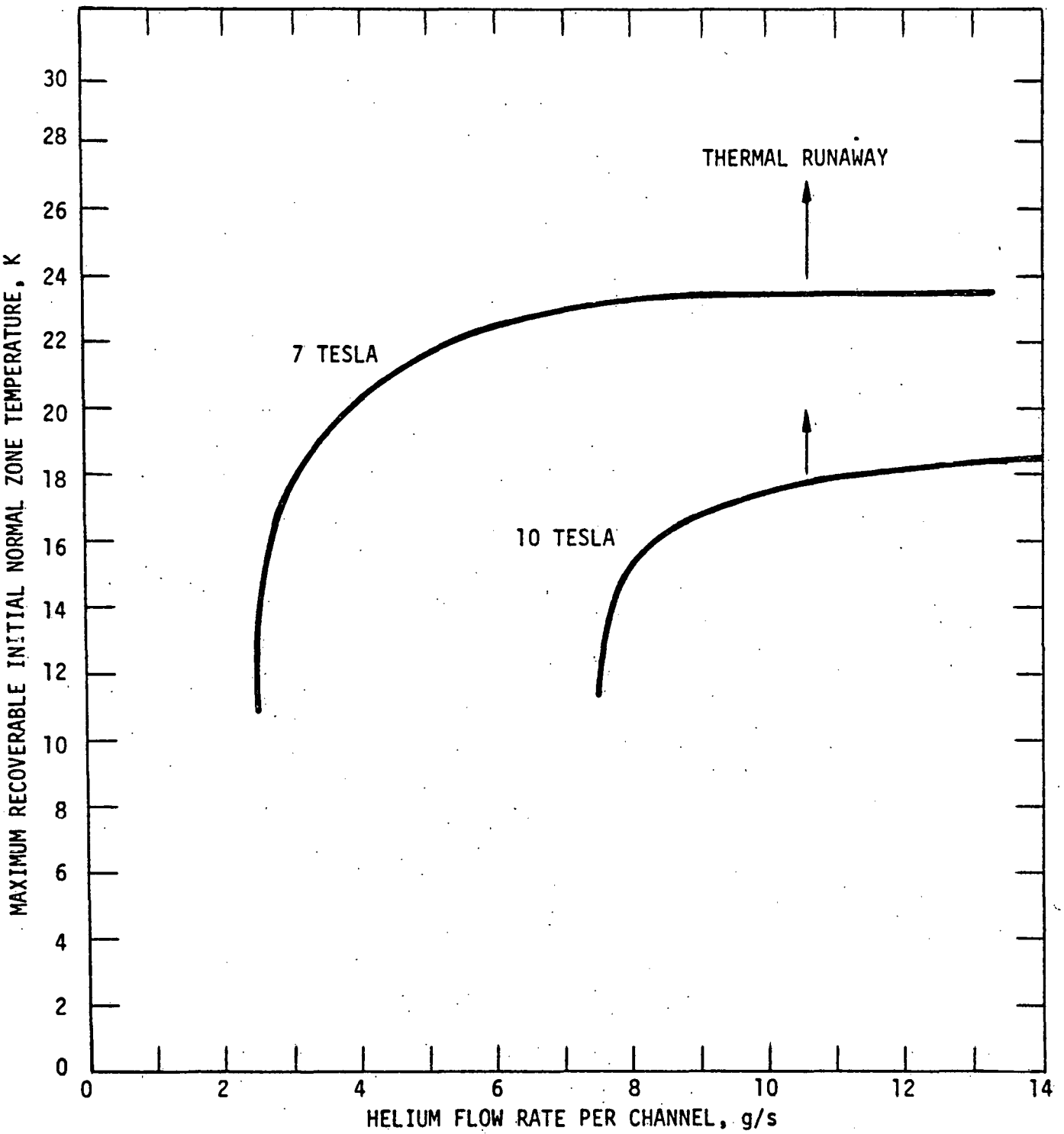

Figure 5-2. Cryogenic Recovery Capability of the Nb_3Sn Superconductors at 10 and 7 Tesla.

5.2 REFRIGERATION LOADS

As discussed in the previous section, the nominal coolant flow rate for the 10 tesla conductor was determined to be 8 g/sec per conductor channel. The corresponding coolant flow velocity is about 0.44 m/sec. Since the conductor length per channel is 50 m (Table 5.1), the coolant residence time is therefore 116 seconds, which is slightly longer than the cycle time of 85 seconds for the DTHR.

If an amount of heat is suddenly deposited into the conductor driving it to a normal state at a temperature below 15 K, the conductor would recover its superconductivity within 30 to 50 msec. But this amount of heat is transferred to the coolant surrounding the normal zone raising the coolant temperature one or two degrees. This slug of hot helium must move out of the channel before the next heat release occurs to remain cryostable. A likely cause of the sudden heat release is during the initiation of a power pulse in the tokamak operation. It is desirable, therefore, to have the coolant velocity high enough to move any hot element out of the channel within a cycle of the power operation. Based on this consideration, the operating coolant flow rate for the 10 tesla conductor was doubled to reduce the residence time to 58 seconds. The required pump work for the 10 tesla conductors, assuming a 75% pump efficiency, was thus calculated to be 45.8 watts per channel.

For the 7 tesla conductor, since the threshold temperature for current sharing is higher at 7 tesla than at 10 tesla, a slower coolant velocity is tolerable. The operating coolant flow rate was increased to three times the nominal value of 3 g/s as given in the previous section. The required pump work, also at 75% efficiency, would be 8.15 watts per channel.

There are 74 channels for each type of conductor and there are two divertor coils, the total pump work is therefore 7.98 kW at 4.2 K. The nuclear heating was estimated, based on 60 cm of shielding surrounding the coils, to be 2 kW averaged over a pulse cycle. The electric power requirement for the sum of these two items is about 3.5 MW.

The dewar heat losses have not been estimated since the dewar design has not been defined at this time. This heat load is usually small compared with the above two items.

6.0 THERMAL DESIGN OF THE PARTICLE COLLECTORS

The details of the mechanical design of the particle collectors are described in Section 4.2. The collecting surfaces are formed by the exposed half of a bank of copper tubes. These tubes are bent into a V-shape. One unit of the V-tubes is shown in Figure 6-1. Peak thermal load (Q_1) on the vertical area normal to the V's is 3.2 kW/cm^2 at the edge of the collector nearest to the divertor coil. This normal flux decreases to 0.07 kW/cm^2 at the far end of the collector. The distribution of the normal heat flux was estimated to be in the manner as shown in the figure. Because of the ten time increase in surface area on the V-tubes, the heat flux (Q_2) on the collector surfaces is therefore, 1/10 of Q_1, except at the vertex of the V's where the heat flux is Q_1. In order to protect the V-tubes, a separate straight tube is placed at the vertices of each of the V bends. This straight tube is not used for particle collection, but acts as a thermal shield. It can be operated at a different temperature from the V-shaped tubes. The thermal designs of the V-tubes and the front tubes are presented in the following subsections.

6.1 COLLECTOR V-TUBES

The length of the V-tubes in this preliminary design was selected to be 2 m long in order to limit the coolant pressure drop and temperature rise. Pressurized water is used as the coolant. Because of the circular curvature of the front surface of the tube, the circumferential heat flux distribution on one tube is taken to vary according to a cosine distribution with the peak value located at the central, outer-most point of the tube.

The thermal design objective is to operate the tube collecting surface at a temperature ranging between 200°C to 300°C for optimum particle collecting efficiency (see Section 3.2 for divertor operation). To meet this requirement the water inlet pressure and temperature were selected to be 35 atm and 170°C, respectively. The water flow rate was determined so that the minimum and maximum tube outer surface temperatures (on the particle collecting half)

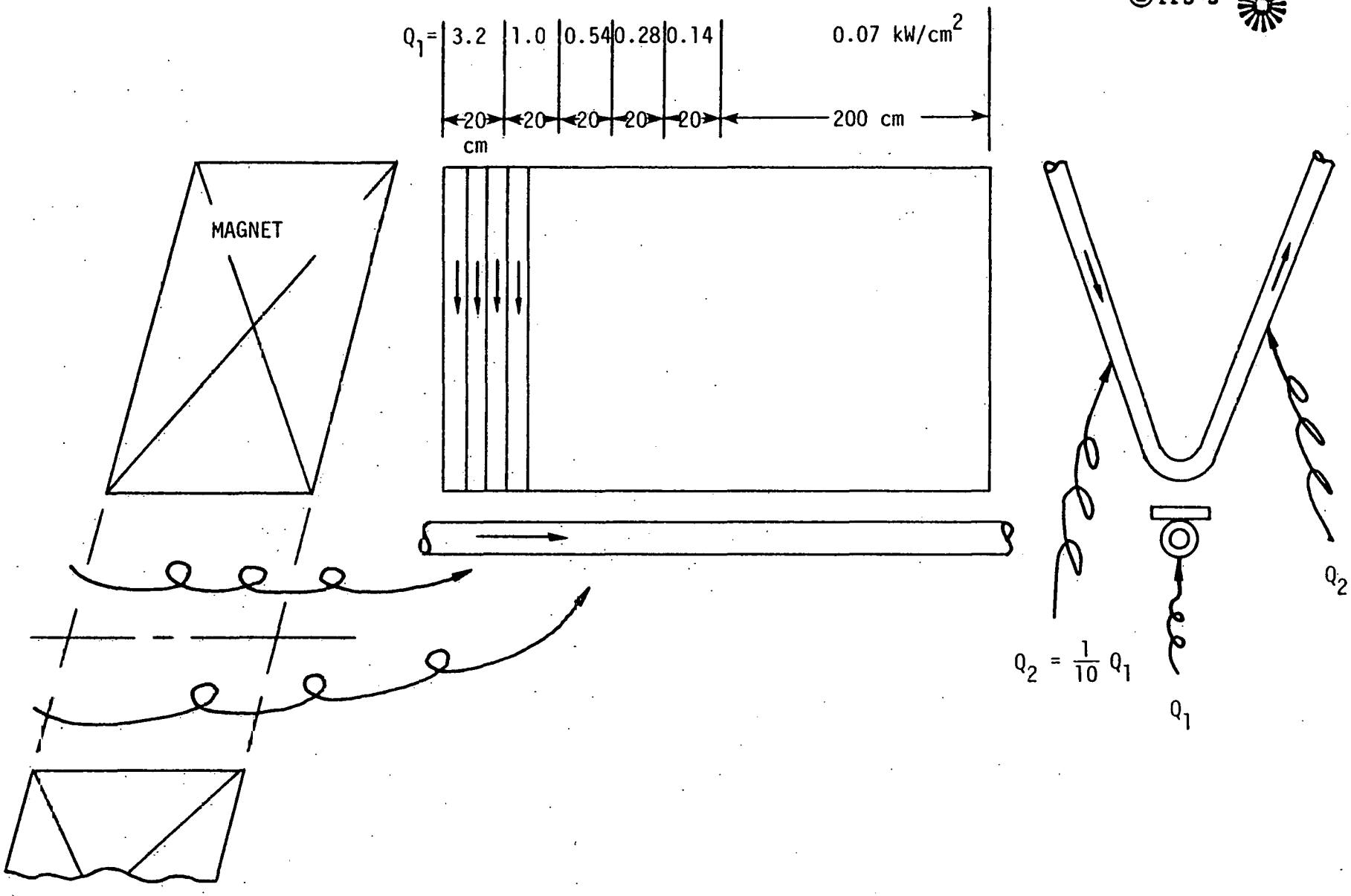

6-1. Bundle Divertor Particle Collector Tubes.

are within this range. Because of the pulse length for the DTHR steady state thermal conditions were calculated. The tubes located at the front edge of the collecting area subjected to the peak heat flux of 3.2 kW/cm^2 were analyzed. The results are summarized in Table 6-1. In this table, results with two tube sizes are shown. For these two sizes of tubes with the flow rates studied, the maximum and minimum front wall temperature are within the temperature range required. The overall average front half wall temperature is about 250°C for optimum particle collecting efficiency. The maximum temperature difference through the wall thickness is about 7°C for all cases. The temperature difference across the tube diameter (circumferential ΔT) is, however, higher for the larger tube. It is expected that for a tube OD of smaller than 0.953 cm (0.375"), the temperature difference across the tube diameter is smaller, but the required pumping power would be much larger. The tube with 0.953 cm (0.375") outer diameter appears to be satisfactory for this application. The circumferential temperature distribution at the outlet end of the tube is shown in Figure 6-2. About 70% of the circumferential ΔT occurs at the front half of the surface where the particles are collected. The thermal conditions of the tubes away from the magnet (see Figure 6-1) would have a similar pattern. The coolant flow rates on these tubes would be reduced according to the surface heat flux at the location.

6.2 FRONT TUBES

The straight tube in front of the vertex of a unit of the V-tubes is used to absorb the high thermal loading along the leading edge of the V-bend. With this front tube the V-tubes behind it can be designed for a uniform thermal loading 10 times smaller. The front tube is also made of copper with 0.8 cm (0.3125") outer diameter, but a wall thickness of 0.05 cm (0.020") instead of the thickness of regular copper tubing stock of the same outer diameter. The thin wall is required for structural performance purposes. Pressurized water is used as the coolant as in the V-tubes. Coolant inlet pressure and temperature were selected to be 34 atm and 100°C, respectively.

Since the particles only strike the front half of the tube surface, in order to reduce the temperature difference across the tube diameter (along the

TABLE 6-1

SUMMARY OF THERMAL DESIGN OF WATER-COOLED V-TUBES FOR PARTICLE COLLECTION

$Q = 0.32 \frac{kW}{cm^2}$, P_{in} = 34 atm, T_{in} = 170°C

CASE	1	2	3	4
TUBE OD, cm(in)	0.953 (0.375")		1.270 (0.500")	
TUBE ID, cm(in)	0.813 (0.312")		1.108 (0.436")	
WATER FLOW RATE kg/s PER TUBE	0.227	0.273	0.364	0.455
T_{out}, °C	232	222	222	212
P_{out}, atm	33.6	33.4	33.8	33.7
ΔP, (psi)	6	9	3	5
MAXIMUM FRONT WALL TEMP, °C (AT TUBE OUTLET)	304	286	313	292
MINIMUM FRONT WALL TEMP, °C (AT TUBE INLET)	205	201	210	203
OVERALL AVERAGE FRONT WALL TEMP, °C (AVERAGED AXIALLY OVER THE FRONT HALF OF TUBE SURFACE)	257	246	265	251
PUMPING POWER AT 75% EFF, WATTS/TUBE	14.5	25.6	10.8	21.6
MAXIMUM HEAT TRANSFER COEFF, W/cm^2-°C	4.35	4.95	3.41	4.02
MAXIMUM REYNOLDS NUMBER	3.16×10^5	3.63×10^5	3.46×10^5	4.12×10^5
MAXIMUM ΔT THROUGH WALL, °C	7	7	7	7
ΔT ACROSS TUBE DIAMETER, °C	68	61	91	80

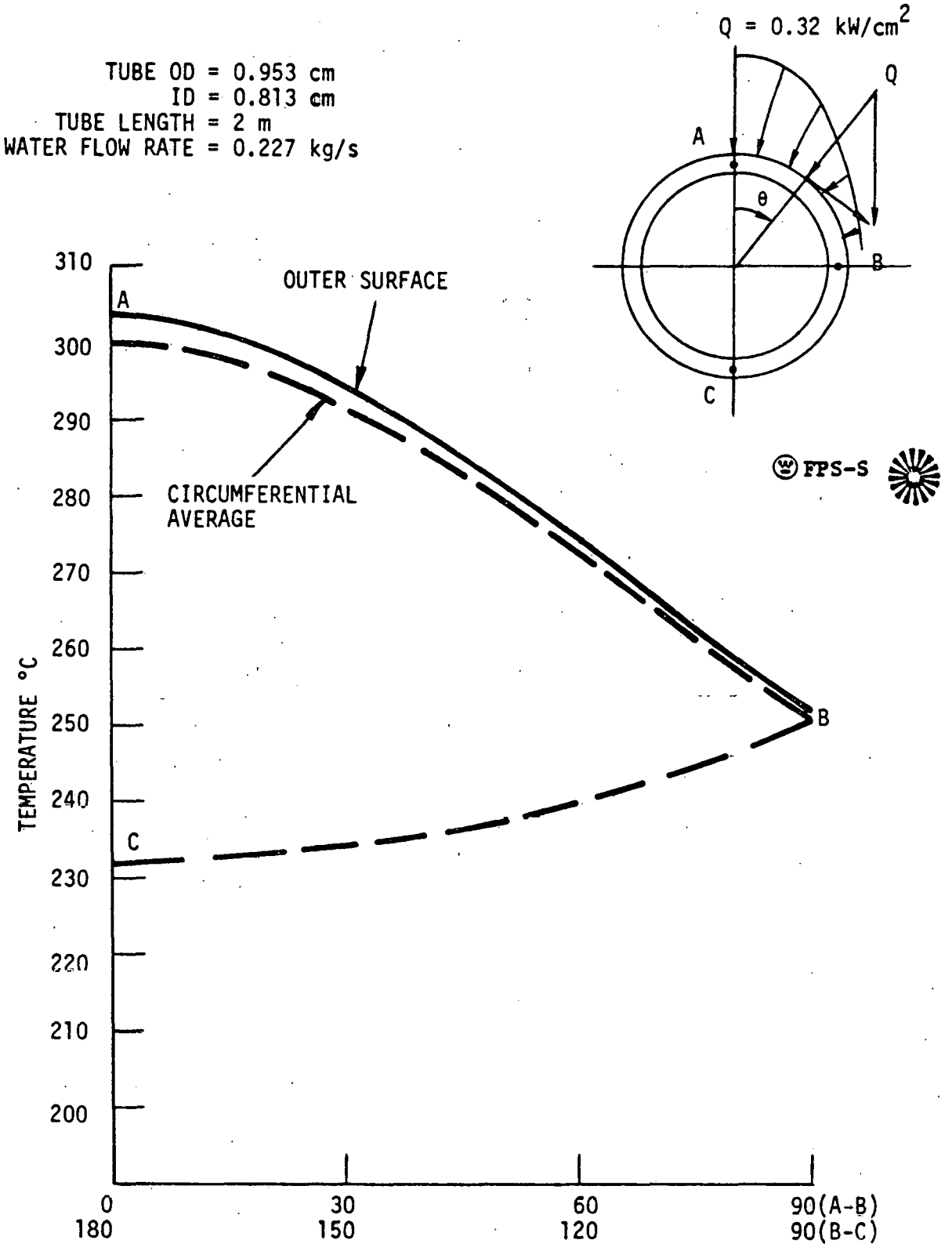

Figure 6-2. Circumferential Temperature Distribution at Tube Outlet End.

circumference of the tube wall), a plate is to be attached to the back of the tube wall to absorb some heat input to the back of the tube. The back plate extends about 0.12 cm beyond the tube diameter at each side and is about 0.13 cm thick.

As seen from Figure 6-1, the heat flux at the inlet end of the tube (nearest the divertor coil) is 3.2 kW/cm^2 extended over a length of 20 cm. The heat flux intensity decreases to 0.07 kW/cm^2 at the other end of the tube. A worst case was analyzed in which steady state, one-dimensional (radial direction) temperature distribution was calculated at the cross section with the peak heat flux of 3.2 kW/cm^2. The thermal design objective is to operate the tube below a maximum temperature of 430°C. This limit is set by the structural performance consideration (discussed in Section 7.0).

Several cooling inlet temperatures ranging from 100°C to 220°C and heat transfer coefficient ranging from 8.5 W/cm^2-C to 16 W/cm^2-C were investigated. In order to keep the maximum tube temperature to below about 430°C, the water inlet temperature of 100°C and heat transfer coefficient of 11.35 W/cm^2-C (20,000 Btu/Hr-ft^2-F) were required. With these water conditions, the circumferential temperature distribution at the inlet end of the tube is shown in Figure 6-3. The maximum temperature difference across the tube wall thickness is 45°C and the maximum temperature difference across the tube diameter is about 213°C. Without the back plate to absorb some heat at the back side of the tube, the temperature difference across the diameter is 326°C, an increase of more than 100°C. These thermal conditions are used in the structural evaluation (Section 7.0).

It is noted that to achieve a heat transfer coefficient in the order of 11 W/cm^2-C inside a tube requires internal turbulence generators. Experiments and analyses using twist tape (swirl vortex tubes) have been performed. References (25) and (26) are examples of published information. Results show that enhancement of heat transfer in single-phase water can be up to a factor of two above that from a smooth tube, but frictional pressure loss can be several times higher than that from a smooth tube depending on the tape twist pitch. Assuming an enhancement of 1.5 in the heat transfer coefficient, the

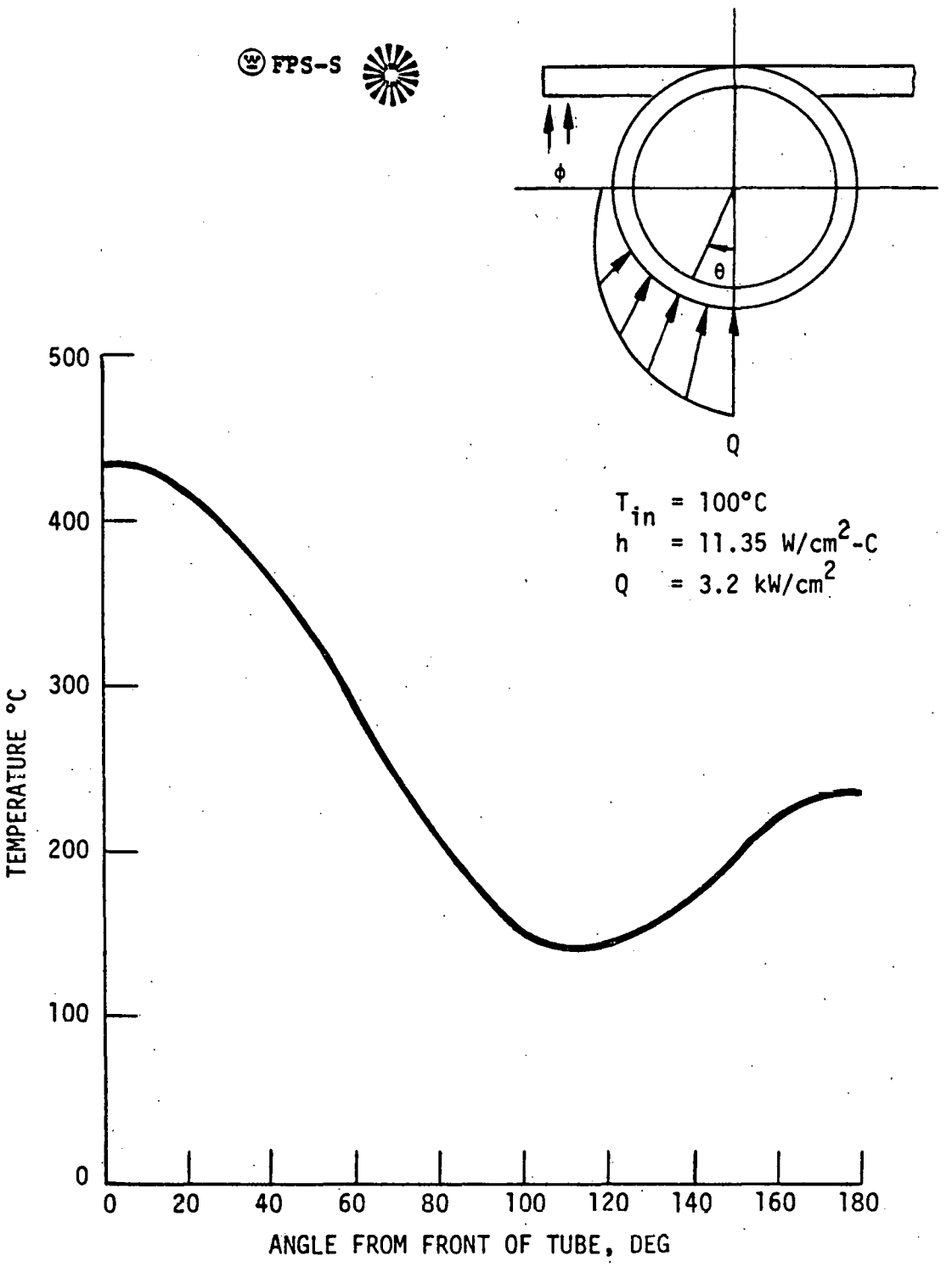

Figure 6-3. Steady State Circumferential Temperature Distribution of the Front Thermal Shield Tube.

Reynolds number required to achieve a heat transfer coefficient of 11.35 W/cm^2-C was calculated to be about 3.5×10^5 for this size of tube. This Reynolds number is in the range of the data and considered obtainable using the twist tape inside the tube.

Considering the axial heat flux distribution on the front tube as shown in Figure 6.1, the integrated surface heat input is 93 kW. Allowing a water temperature rise across the 3 m long tube of 58°C, the water flow rate required for steady state operation is 0.6 kg/sec. If the frictional pressure loss is increased by a factor of two due to the presence of the tape, the pressure loss over the 3 m length is 1.54 MPa (15.2 atm). Since the water inlet pressure is selected to be 34 atm, this should not impose any problem of boiling at the tube exit. It should be noted that only a length of 20 cm at the inlet end is subjected to the peak heat flux, the twist tape is not needed over the entire length of the front tube. This would further reduce the overall pressure loss over the tube. For example, if the twist tape only extends over 20 cm at the region of the peak thermal load, the frictional pressure loss across this 20 cm length is only about 1 atm which is quite small.

7.0 COLLECTOR STRESS EVALUATION

The structure of the collector panels under a peak heat flux was evaluated[27] in relation to criteria that protect against coolant leakage into the plasma over planned replacement schedules. A one year replacement schedule at 40% availability was chosen for the bobbin closest to the plasma based on the nuclear shielding assessment given in Section 8.0.

The scope of the structural evaluation covers all V-shaped tube bundles and thermal shields, but was reduced by considering only the severely loaded thermal shield tube which is a worst case upper bound to the less severely loaded tubes in the V-shaped tube bundles. Other components, including the headers and support structure not directly exposed to the heat flux, are not considered to limit planned replacement schedules.

7.1 V-SHAPED TUBE BUNDLE AND THERMAL SHIELD

Individual V-shaped tube bundles are fabricated from 0.95 OD x 0.08 cm wall tubes while the thermal shield tubes are 0.8 OD x 0.05 cm wall. Both tubes are constructed from Amzirc, a high thermal conductivity copper alloy with zirconium, to provide a yield stress higher than that of pure OFHC copper. The V-shaped tubes are 35% cold worked and aged to provide the ductility necessary for forming the vertices without cracking. The thermal shield tube is 85% cold worked and aged to permit the spiral ribbon to be swaged in place. The thermal shield back plate is a 1 cm wide x 0.13 cm thick sheet formed to mate with the curvature of the 0.8 cm OD thermal shield tube. OFHC copper is used as the thermal shield material to provide an optimum brazing condition with the Amzirc tube. The coolant in both V-shaped tubes and the thermal shield tube is water pressurized to 3.45 MPa. The water flow rate in the V-shaped is adjusted to maintain the tube surface temperature below 300°C to provide optimum adherence of charged particles. For the thermal shield tube exposed to the intense incident heat flux, the water flow rate is selected to maintain

reasonable metal temperatures with collection of charged particles of least importance. A spiral ribbon is provided in the thermal shield tube, is swaged in place to induce vortex flow and promote a high water to tube heat transfer coefficient necessary to dissipate the intense incident heat flux. An isometric view of the V-shaped tube bundle and thermal shield is presented in Figure 3-1.

7.2 LOADING EVALUATION

The thermal shield tube mechanical loads include internal coolant pressure, deadweight, and seismic loads. Of these, only internal coolant pressure is considered significant. Owing to the water coolant flow pressure drop, the worst case internal pressure load (P) in the thermal shield tube occurs at the water inlet, p = 3.45 MPa.

The thermal shield tube thermal loads are the through-the-wall and across-the-tube temperature differences associated with the nominal heat flux of 3.2 kW/cm^2. Of these thermal loads, only the through-the-wall temperature differences are of importance in the thermal shield tube. Owing to the presence of the backing plate, across-the-tube temperature differences are attenuated so as to reduce bending stresses in the thermal shield under the intense incident heat flux to negligible levels. Furthermore, the through-the-wall temperature difference is the worst case only at one end of the thermal shield tube, which by design corresponds to the inlet water coolant. This is because the orientation of the thermal shield tube imposes a peak heat flux of 3.2 kW/cm^2 at the inlet coolant end with a rapidly decreasing incident heat flux along its length to the outlet coolant end.

In summary, the worst case thermal shield tube duty cycle consists of a 3.45 MPa internal coolant pressure mechanical load sustained throughout plasma on-off cycling with a zero pressure condition maintained during the elevated temperature bake. Swelling loads associated with neutron irradiation are assumed to be negligible. Thermal loads corresponding to plasma-on conditions cause a through-the-wall temperature difference of 45°C with a peak outside wall surface temperature of 426°C. During plasma-off conditions, a zero through-the-wall temperature difference occurs with a peak outside surface temperature equal to

the water inlet coolant temperature of 100°C. The plasma on-off cycles are repeated seven times for approximately 10 minutes followed by a bake at 600°C for 10 minutes. Each plasma on-off cycle is taken to be on for 70 seconds and off for 15 seconds. The seven plasma on-off cycles and the 10 minute bake represent a block loading of a 20 minute duration which is repeated consecutively for a total of 26,280 times over the one year replacement schedule. The thermal shield tube worst case duty cycle is illustrated in Figure 7-1.

7.3 STRESS ANALYSIS

The stress analysis is directed to the thermal shield tube over the worst case duty cycles. The stresses are computed by linear elastic methods which are justified as the maximum equivalent stress is less than the 0.1% off-set yield stress for Amzirc of 96.5 MPa.

The mechanical stress (σ_p) induced in the thermal shield tube of radius (R = 0.4 cm) and wall thickness (t = 0.05 cm) under a sustained coolant pressure (p = 3.45 MPa) during plasma on-off cycling is maximum in the hoop direction and given by the relation:

$$\sigma_p = \frac{PR}{t} = 27.6 \text{ MPa}$$

The thermal stress (σ_T) induced in the thermal shield tube wall of Young's modulus (E), Poisson's ratio (ν), and coefficient of thermal expansion (α) for a through-the-wall temperature difference (ΔT) in both hoop and meridional directions is given by the relation:

$$\sigma_T = \frac{E \alpha (\Delta T)}{2 (1-\nu)} = 73.1 \text{ MPa}$$

Here, $E = 12.9 \times 10^4$ MPa, $\alpha = 17.64 \times 10^{-6}/°C$, $\nu = 0.3$, and $\Delta T = 45°C$.

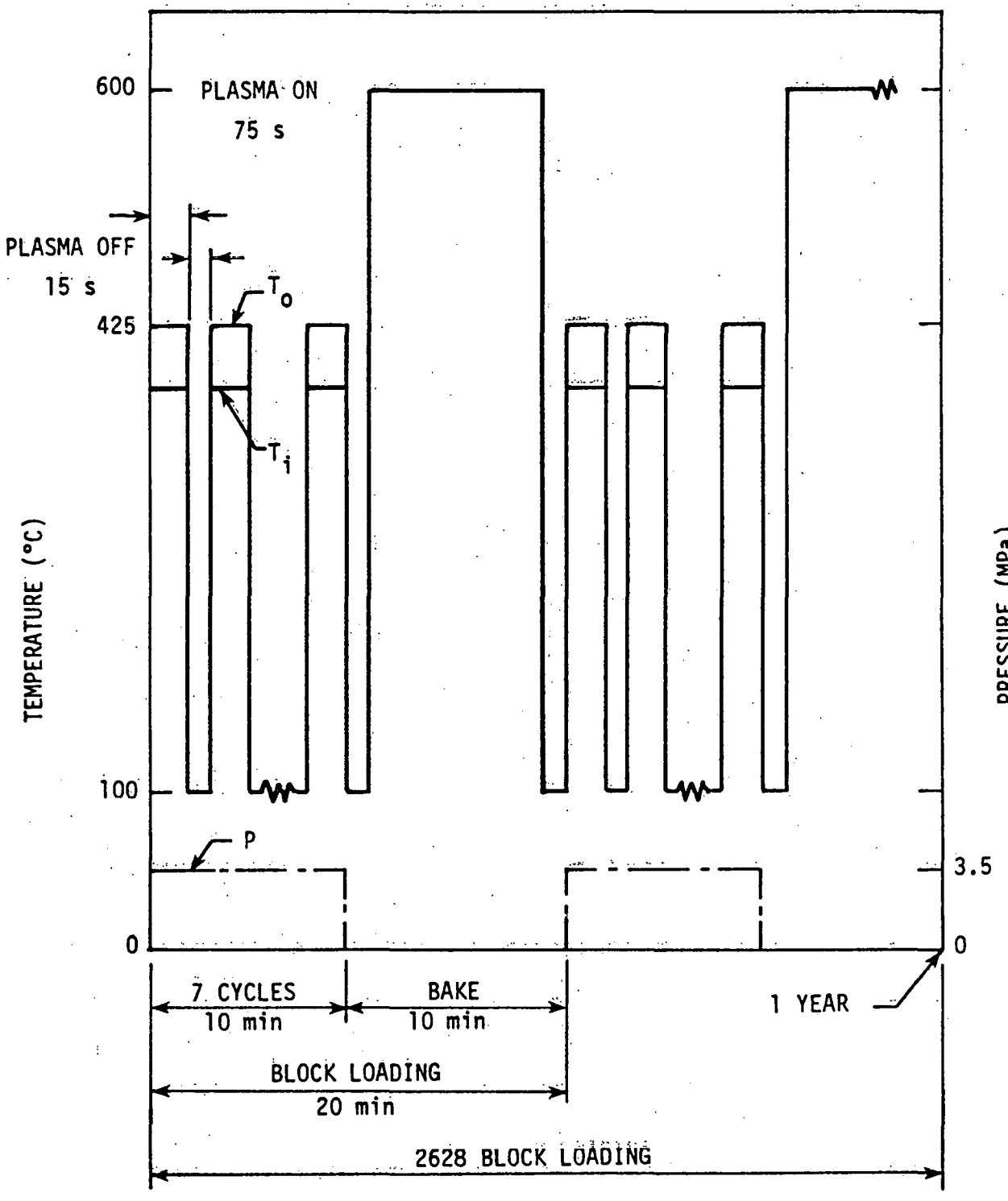

Figure 7-1. Thermal Shield Tube Worst Case Duty Cycle.

7.4 STRUCTURAL CRITERIA AND EVALUATION

The thermal shield tube structural criteria protect against coolant leakage and subsequent contamination of the plasma. Coolant leakage is characterized by a hypothetical surface crack at BOL (Beginning-of-Life) of a depth which prior to EOL (End-of-Life), slowly grows through the wall causing a coolant leakage into the plasma. The hypothetical surface crack at BOL is considered to cause EOL coolant leakage by combined fatigue and creep-crack growth alone. Criteria to protect against excessive deformation failure modes, such as perturbations of the spiral ribbon which lead to hot spots and thereby promote coolant leakage by accelerated fatigue and creep-crack growth, represent a greater degree of sophistication and are not justified for structural evaluations at this time.

The specific thermal shield tube structural criteria is quantified by assuming a hypothetical semi-circular surface crack of a depth (a_o) and length ($2\ C_o$) to be present in the tube wall at BOL. The BOL crack depth (a_o) is taken to be 25% of the wall thickness (t) or the mean grain size diameter of full thermally softened Amzirc ($a_o \cong 0.008$ cm), whichever is greater. In order to protect against coolant leakage, the controlled quantity is selected as the change in crack depth (Δa) with the criterion for acceptability being 10% of the initial crack depth (a_o). The change in crack depth (Δa) corresponds to the difference between EOL crack depth (a_f) and BOL crack depth (a_o), i.e.,

$$\Delta a = a_f - a_o \leq 0.10\ a_o$$

Linear Elastic Fracture Mechanics (LEFM) was chosen as a method to estimate the EOL crack growth. For the thermal shield tube constructed from Amzirc with a relatively low yield strength and applied elastically calculated equivalent stresses near yield values, the use of LEFM methods is a less defensible position than employing J-integral methods. However, it is not unreasonable that LEFM methods provide a first approximation to estimates of fatigue and creep growth for elastically calculated equivalent stresses near the yield strength of Amzirc, and as such, were adopted for the thermal shield tube.

In the LEFM method, the crack growth is related to the elastic stress intensity factor (K). Fatigue-crack growth (da/dN) is dependent on the range of stress intensity factor (ΔK) between maximum (K_{max}) and minimum (K_{min}) values corresponding to plasma-on and off conditions, respectively. Creep-crack growth (da/dt) is dependent on the maximum stress intensity factor (K_{max}) associated with the hold-time during plasma-on conditions. With regard to creep-fatigue interaction on crack growth, no data is currently available for Amzirc to justify a linear damage summation. However, for the sake of completeness in the interim, a linear damage rule is assumed for the thermal shield tube constructed of Amzirc. Accordingly, the EOL crack depth (a_f) is expressed in terms of the BOL crack depth (a_o), and fatigue-creep crack growth materials data according to the relation:

$$a_f = a_o + \int_{a_o}^{a_f} \left(\frac{da}{dN}\right) dN + \int_{a_o}^{a_f} \left(\frac{da}{dt}\right) dt$$

Where, a = crack depth (cm)

$\frac{da}{dN}$ = fatigue-crack growth (cm/cycle) = $C_f (\Delta K)^{n_f}$

C_f, n_f = fatigue constants

ΔK = elastic stress intensity factor range (MPa $\sqrt{cm}$)

N = number of fatigue cycles

$\frac{da}{dt}$ = creep-crack growth (cm/hr) = $C_c (K_{max})^{n_c}$

C_c, n_c = creep constants

t = time (hours)

The thermal shield tube is assumed to have a hypothetical semi-circular surface crack present at BOL with a crack depth (a_o) equal to the greater of 25% of the wall thickness of 0.008 cm. For the tube with a wall thickness of 0.051 cm, the BOL crack depth (a_o) is governed by 25% of the wall thickness, i.e., a_o = 0.013 cm.

The elastic stress intensity factor K-solution for Mode I axial surface cracks in cylindrical shells as applied to a semicircular crack with a depth to wall

thickness ratio (a/t = 0.25) is given by:

$$k = 0.127\ [1.03\ \sigma_t + 0.7\ \sigma_b + 1.13\ P]$$

Where, σ_t = membrane stress (MPa)

σ_b = bending stress (MPa)

P = internal pressure (MPa)

In the thermal shield tube, the maximum elastic stress intensity factor (K_{max}) occurs during plasma-on conditions, while the minimum value (K_{min}) corresponds to plasma-off conditions.

For plasma-on conditions, the linearized elastically calculated membrane (σ_t) and bending (σ_b) stresses for an internal coolant pressure (P) provide the worst case tensile stress at the inside surface of the thermal shield tube. They are: σ_t = 27.6 MPa; σ_b = 73.1 MPa; and P = 3.45 MPa.

Accordingly, the maximum stress intensity factor (K_{max}) is

$$K_{max} = 10.6\ \text{MPa}\ \sqrt{\text{cm}}$$

Similarly, for plasma-off conditions, σ_t = 27.6 MPa, σ_b = 0, and P = 3.45 MPa. Thus, the minimum stress intensity factor (K_{min}) is:

$$K_{min} = 4.1\ \text{MPa}\ \sqrt{\text{cm}}$$

With the regard to a structural evaluation, fatigue and creep-crack growth data for Amzirc is not available at the specific plasma-on operating temperature of 426°C in the presence of periodic baking at 600°C. Accordingly, accurate estimates of EOL crack depth are not possible at present. On the other hand, some related materials data is available which, if extrapolated to thermal shield tube temperatures, can be used in the interim to establish the potential for design acceptability until specific materials data becomes available.

Fatigue-crack growth data within Westinghouse is available for annealed OFHC copper in an air, dry argon, dry hydrogen and hydrogen saturated water at 24° and 82°C shows no effect of environment or temperature on either crack growth rate (da/dN) or the threshold stress intensity factor range (ΔK threshold). In the open literature, the threshold value reported for copper is 13.2 MPa $\sqrt{cm}$. However, the Westinghouse data indicates that the threshold value for annealed OFHC copper is higher than 13.2 MPa $\sqrt{cm}$. The threshold stress intensity factor range is of special interest in high cycle -- low stress application such as the thermal shield tube because no crack growth occurs for applied stress intensity factor ranges less than the threshold value.

Owing to the similarities between OFHC copper and Amzirc, and the fact that an environmental or temperature effect was not observed over test conditions for annealed OFHC copper, it is not unreasonable that the fatigue threshold for Amzirc at 426°C would be similar to that for annealed OFHC copper at 82°C. Accordingly,

$$\frac{da}{dN} = 0, \text{ for } \Delta K < \Delta K \text{ threshold}$$

Where, ΔK threshold = 13.2 MPa $\sqrt{cm}$.

In ductile materials, such as Amzirc and OFHC copper, crack tip blunting occurs at elevated temperature so that conventional stress rupture properties provide an indication of creep-crack growth (da/dt) at instability. Available stress rupture data for 85% cold worked Amzirc aged during the stress-rupture test at 400°C show rupture times of 100 and 300 hours at stress levels of 241.4 and 220.7 MPa, respectively. The stress rupture data is representative of the thermal shield tube at a maximum operating temperature of 426°C, but does not reflect the accelerated aging at the bake temperature of 600°C. Stress rupture data for hard drawn OFHC copper at 450 and 650°C show a rapid decrease in rupture times with increasing temperature. The effect of the elevated temperature bake on 85% cold worked Amzirc based on the decrease in rupture time observed for hard drawn OFHC copper is illustrated in Figure 7-2.

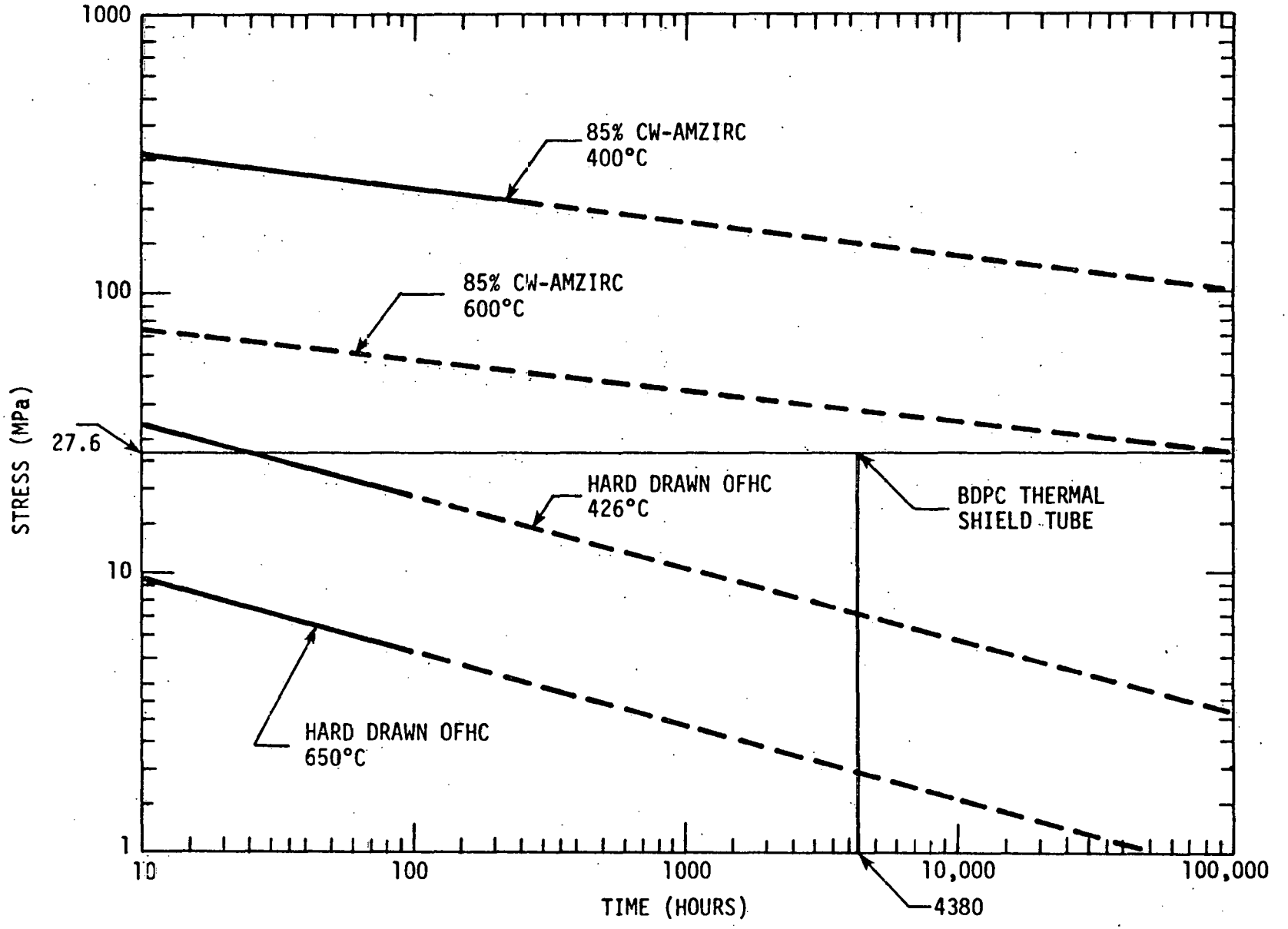

Figure 7-2. Estimated Amzirc Stress Rupture Data.

A review of the estimated stress rupture data in relation to creep-crack growth (da/dt) for 85% CW-Amzirc at 600°C for the thermal shield tube is as follows. Over a one year replacement schedule, a total of 526 plasma-on cycles with 85 s durations correspond to 4380 hours of operation at 600°C. At a water coolant pressure of 3.45 MPa, the hoop stress in the thermal shield tube is 27.6 MPa with a time to rupture of 100,000 hours. Accordingly, the creep damage is approximately 4.4% at 100% availability. For a 40% availability, the creep damage is 1.7%. Thus, stress rupture is not expected for the thermal shield tube. Alternately, unstable creep-crack growth (da/dt) for Amzirc at thermal shield tube temperatures over planned replacement schedules is not expected. For the purposes of the thermal shield tube structural evaluation, the creep-crack growth (da/dt) is taken to be zero. With regard to fatigue-crack growth (da/dN), the applied stress intensity factor range (ΔK),

$$\Delta K = K_{max} - K_{min}$$

$$\Delta K = 10.6 - 4.1$$

$$\Delta K = 6.5 \text{ MPa } \sqrt{cm}$$

Now, ΔK threshold = 13.2 MPa $\sqrt{cm}$. As $\Delta K < \Delta K$ threshold, no fatigue crack growth occurs.

Thus, the EOL crack depth (a_f) is estimated as approximately equal to the BOL crack depth (a_0), i.e., $a_f \cong a_0$. The thermal shield tube structural criterion in protecting against coolant leakage into the plasma requires that the increase in crack depth (Δa) from BOL to EOL to be less than 10% of the BOL crack depth, i.e.,

$$\Delta a \leq 0.10\ a_0$$

As the EOL and BOL crack depth were found to be approximately equal to each other, the change in crack depth ($\Delta a = a_f - a_0 \cong 0$). For the criterion ($0.10\ a_0 = 0.00125$ cm), coolant leakage caused by crack growth is not expected in the thermal shield tube over planned replacement schedule.

7.5 RECOMMENDATIONS

The current thermal shield tube design utilizes water as a coolant pressurized to 3.45 MPa and a spiral ribbon to promote a high film coefficient by inducing vortex flow. However, the high coolant pressure also enhances creep-crack growth in the Amzirc, and thereby reduces operating life at elevated temperature. In addition, the use of a spiral ribbon requires swaging to retain its position in the tube, but requires the use of Amzirc in an annealed condition to permit swaging. However, the use of cold work Amzirc is desirable because the resistance to creep-crack growth is retained longer, thereby promoting longer thermal shield tube replacement schedules approaching 5.0 kW/cm^2. In this arrangement, liquid sodium may be a better coolant selection for the thermal shield tube as a high film coefficient is obtained at low pressure without a spiral ribbon. As such, the use of liquid sodium, as the thermal shield tube coolant is recommended for future design studies. Since the collector is outside the TF coils and in the weak field region as compared to being inside the torus and in high field regions as is the case for poloidal divertors. The use of liquid metals as a coolant may be plausible.

In order to provide confidence in subsequent structural evaluations of the thermal shield tube, fatique and creep-crack growth data for cold worked Amzirc in a water or liquid sodium environment reflecting the thermal softening that occurs during operation and baking is required. Precracked, flat tensile specimens simulating the load controlled coolant pressure stress and deformation controlled thermal stress in assessing the adequacy of Amzirc are recommended. It should be noted that the structural evaluation is the worst case and includes baking at 600°C. However, regeneration by baking may not be required, and as such, the structural life of the thermal shield tube should increase significantly. The latter will be considered in future design studies.

8.0 SHIELDING ASSESSMENT

The minimum shielding space to protect against the direct neutrons is between the first wall and the foremost corner at the outside leg of the divertor coil. This space is 60 cm. The shielding design has not been done. However, a good assessment can be obtained based on the work by Faulkner for the ORNL/W TNS[28] and published information[29].

The TNS is about the same size as DTHR. The space between the first wall and superconductive TF coils was filled with 30 cm of shielding material (65% in volume of stainless steel and 35% borated water), 25 cm water-cooled copper EF coils (50% each in volume), 5 cm void, 5 cm lead, 15 cm thermal insulation, and 60 cm void. The total shielding space excluding void is 60 cm (30 cm SS and borated water, 25 cm copper and water, and 5 cm lead) which would fit into the shielding space for the divertor of DTHR. This is obviously not the best choice of shielding design for a divertor but can be used to assess the problem. The neutron and gamma fluxes for the shielding materials just described are shown by Figure 8-1. This curve shows almost three decades of attenuation. The total nuclear heating rate across the shielding, copper, and superconductive TF coils is shown by Figure 8-2. Faulkner[29] gave an analytical expression for nuclear heating in the TF coils as

$$W(X) = P_w \times 1.277 \times e^{-\frac{t}{T}} \; e^{-\frac{x}{X}} \; W/cm^3 \qquad (8\text{-}1)$$

where P_w is the neutron wall loading in MW/m^2, t is the thickness of shielding provided by the vessel shield and copper coils and T is the characteristic length of e-folding attenuation, x is the depth into the TF coil which is replaced by divertor coils in DTHR and X is the characteristic length of e-folding attenuation. Here, T = 8.1 and X = 11.6. The effective shielding thickness for one decade of attenuation is 18 cm.

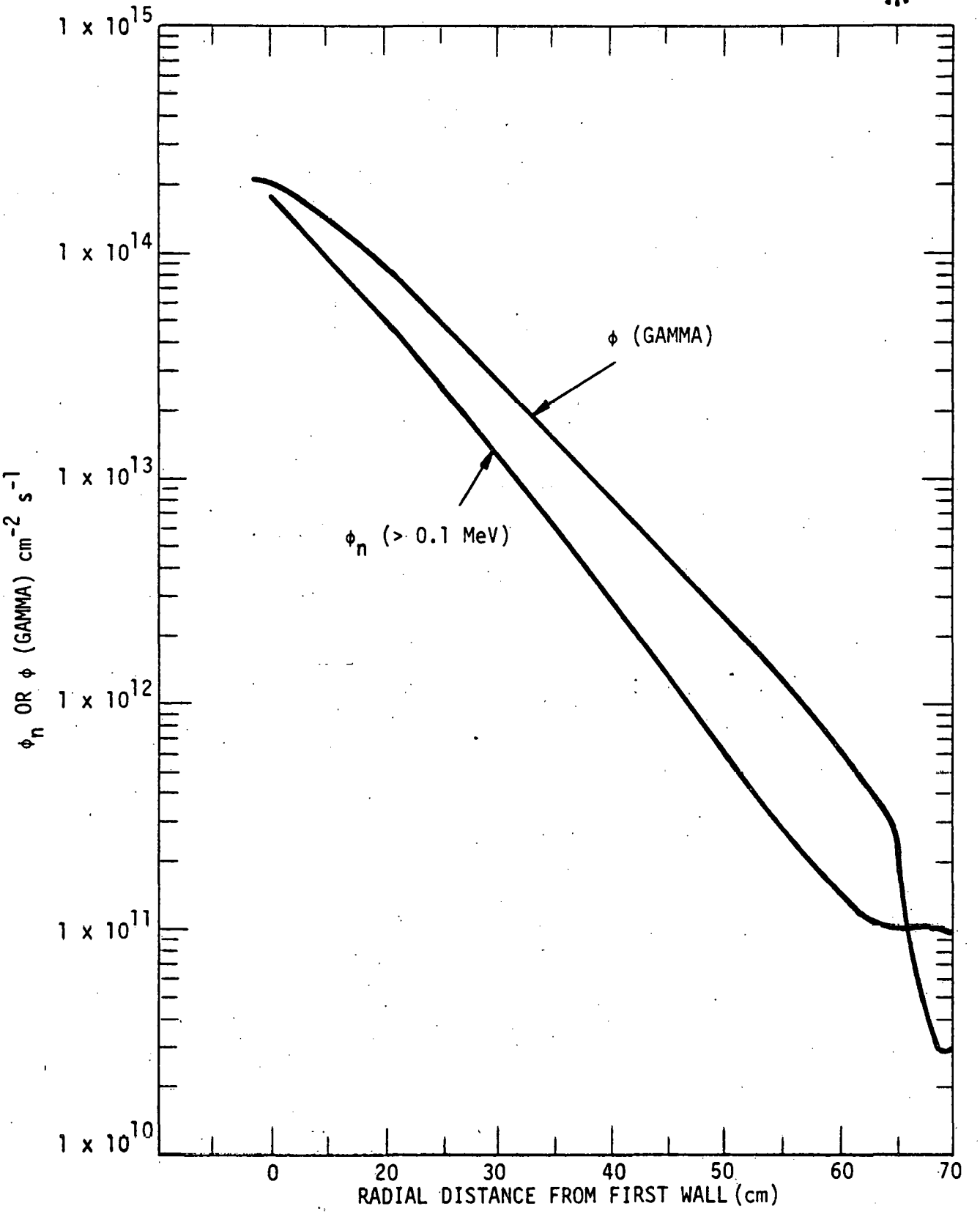

Figure 8-1. Neutron and Gamma Fluxes at Distances from First Wall. (See Figure 8-2)

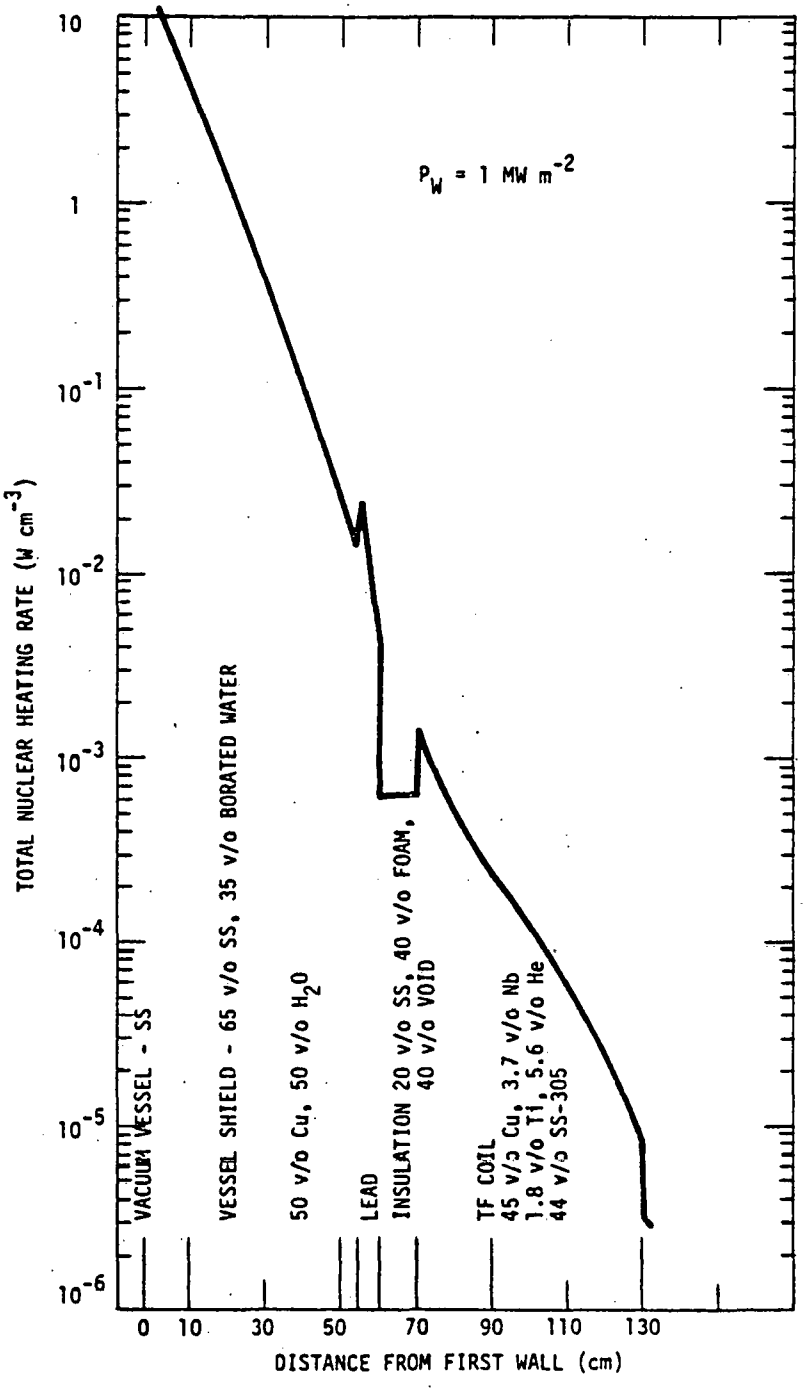

Figure 8-2. Total Nuclear Heating Rate. Data Taken From TNS (Reference 28). Note NbTi is Used in this Case. This Data is Used to Assess the Shielding Need and is not Specifically Done for this Design.

The effects of this radiation heating of the divertor coil can be evaluated in terms of refrigeration requirements and the insulator damage. Integrating Equation (8-1) from x = 0 to 110* cm and using t = 60 cm then multiplying by the annular area of the coil the total nuclear heating is found to be 2.0 kW for P_w = 2 MW/m^2. The refrigeration pumping requirement is nominal for this heating power.

The highest nuclear heating rate is 3 x 10^{-3} W/cm^3 at the corner of the coil closest to the plasma where the insulator will be subjected to the most serious damage. The machine operates ~20% of the time (50% duty factor, 40% availability). The maximum dose on the epoxy insulator is 3 x 10^9 rads which is about the maximum allowable dose[30,31]. This means that the front bobbin has to be repaired once a year. This estimation is conservative. Better shielding materials, which can give four decades of attenuation, are available. One such shield design, for example, consists of W and B_4C as has been studied by Abdou[29]. The characteristic length for an e-field attenuation is T = 6.5 cm which is equivalent to one decade of attenuation per 15 cm. A 60 cm shielding space would give four decades of attenuation; the life time of the insulator would be three times longer. An epoxy fiberglass insulator that can tolerate a dose as high as 10^{10} rads is also reported[31]. It can be concluded that a 60 cm shielding space for a bundle divertor may be adequate, even for commercial reactors, based on the radiation dose limit on insulator. The life of the superconductor stabilizer may be another limiting factor. All of these will be evaluated when the proper radiation shielding is designed.

---

* Note data used is assumed approximately right for the purpose of assessing the shielding need. Exact calculation for proper shielding and Nb_3Sn will be carried out.

9.0 DIVERTOR POWER REQUIREMENTS

The divertor coil is unusual in that the power required to charge the superconducting coil is small compared to the bus losses. Consequently, the rating is a function of the coil current and the bus voltage drop. The self-inductance of the coils is calculated by assuming the coils are circular with a rectangular cross section. For this:

$$L = 0.132 \text{ H.}$$

The ratings of the system and subsystems were determined based on the peak conductor current I_c = 32 kA. Figure 9-1 shows the block diagram of the system.

9.1 DIVERTOR COIL CHARGING REQUIREMENTS

A reasonable charging time was chosen to be t_c = 1800 s. The maximum power is

$$\begin{aligned} P_c &= (1/2\ L_c I_c^2/t_c) \times 2 \\ &= (0.132)\ (32 \times 10^3)^2/1800 \\ &= 75.2 \text{ kW,} \end{aligned}$$

and the coil voltage

$$V_c = \frac{P_c}{I_c} = 2.35 \text{ volts}$$

9.2 REQUIREMENTS FOR THE BUS

Assuming conservatively that the bus length is L_B = 121.9 m (400 ft), and using aluminum bars with a resistance of $6.2 \times 10^{-6}/(12 \times 0.0254)$ ohm/m for 3.0 kA per conductor, the total resistance is

$$R_B = 6.2 \times 10^{-6} \times \frac{2\ L_B}{12 \times 0.0254} \times \frac{3000}{I_c} = 0.122\ \frac{L_B}{I_c},$$

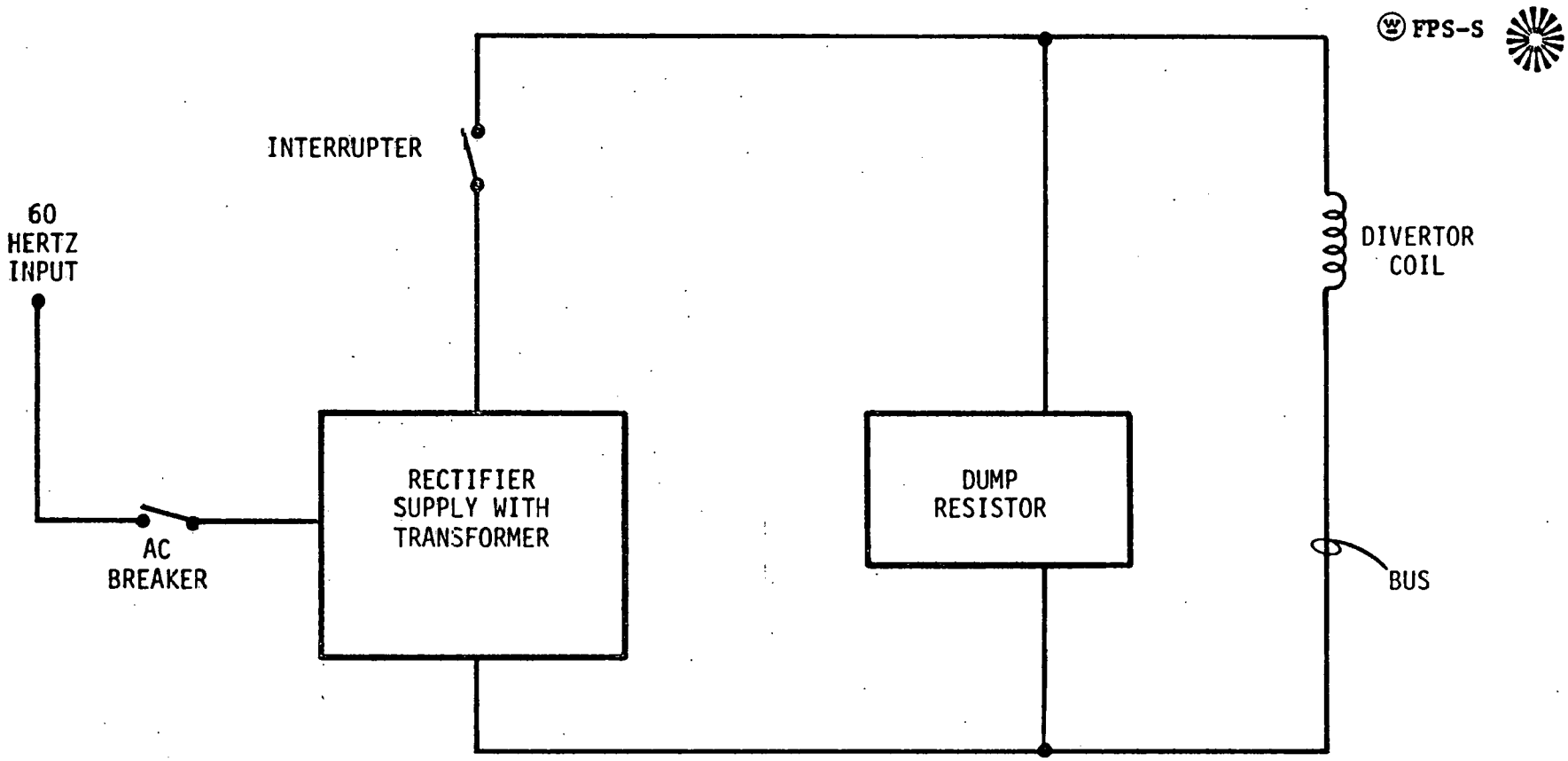

Figure 9-1. Divertor Power Supply System.

and the bus voltage drop is

$$V_B = I_c R_B = 14.9 \text{ volts.}$$

9.3 POWER SUPPLY

The supply voltage is

$$V_s = V_c + V_B = 17.2 \text{ volts.}$$

The supply rating is

$$R = V_s I_c = 551 \text{ kW.}$$

Assuming 90% supply efficiency, the maximum power from ac line input is

$$R_{ac} = \frac{R}{0.9} = 612 \text{ kW.}$$

After the coil is charged the steady state requirement will be

$$R_{ac} \text{ (steady state)} = \frac{V_B}{0.9} I_c = 16.53 I_c = 529 \text{ kW}$$

Assuming 6% regulation the maximum VA rating of the line is

$$R_{VA} = \frac{\pi}{2\sqrt{2}} (R_{ac}) (1 + \text{REG})$$

$$= 721 \text{ kVA}$$

9.4 POWER REQUIREMENT SUMMARY

The power requirement for the cryogenic refrigeration is 3.5 MW (see Section 5-2). The water pump for the collector panel requires less than 0.1 MW. The electric power requirement can be summarized as:

Input Power to Supply	0.61 MW
Refrigeration Power	3.5 MW
Maximum Water Pump Power	0.1 MW
Total	∿ 4.2 MW

10.0 SUMMARY AND CONCLUSIONS

A positive conclusion that can be drawn from this complete integrated design study is that a bundle divertor impurity control and exhaust system is feasible for a demonstration reactor such as DTHR. Since DTHR conditions are in the reactor regime, the extrapolation to a commercial reactor is not a major step. The major design features of the reference bundle divertor are summarized in Table 10-1.

The design method can be extrapolated based on the criterion that the maximum toroidal field intensity can be nulled to create a separatrix. Such field strength is about 4 tesla, which is in the intermediate range expected for future reactors when the scrape-off thickness is 20 cm and the nuclear shielding space is a minimum of 60 cm. The divertor coil windings are made from superconducting Nb_3Sn/Cu cable, which has an overall cross section of 2.45 cm x 2.45 cm and can carry a current of 32 kA. Such a superconducting cable is within current technology. Cryostable forced flow supercritical helium cooling systems can be designed for a 10 tesla field because of the relatively short pumping path. A safety factor of two for the helium flow speed was selected. Overall power requirements are less than 5 MW. The structure is designed for the maximum magnetic stress using the yield strength of stainless steel as the design limit and employing a safety factor of two.

The peak thermal flux (3.2 kW/cm^2) imposed on the collector system is localized on a very short length (less than 20 cm) thermal shield tube located near the separatrix. Heat removal is not difficult even when using water as the coolant in the thermal shield tube. The materials integrity will limit the life of the thermal shield tube under high water pressure; however, life of the thermal shield tube can be improved by designing it as a separate circuit detached from

TABLE 10-1

SUMMARY OF KEY BUNDLE DIVERTOR DESIGN PARAMETERS

MAXIMUM THERMAL POWER DIVERTED	280 MW
PARTICLE THROUGHPUT	3.6×10^{22}/s
DIVERTOR COILS	
AUXILIARY COIL CURRENT	6.4 MA-TURN/COIL
DIVERTOR COIL CURRENT	14 MA-TURN/COIL
MIRROR EXPANSION COIL CURRENT	0.10 MA-TURN/COIL
DIVERTOR COIL ANGLE α	40°
OVERALL AVERAGE CURRENT DENSITY	4 kA/cm^2
SHIELDING SPACE	0.6 m
DIVERTOR COIL INSULATOR LIFETIME	> 1 YEAR
CRYOGENIC SYSTEMS	
CONDUCTOR	Nb_3Sn/Cu
CONDUCTOR SIZE	2 cm x 2 cm
CABLE CURRENT	32 kA
CABLE CURRENT DENSITY	8 kA/cm^2
HELIUM INLET TEMPERATURE	4.2 K
NUCLEAR HEATING LOAD	2 kW
PUMPING POWER	3.5 MW
COIL MECHANICAL PERFORMANCE	
MAXIMUM STRESS	2090 N/cm/CABLE
TORQUE	124 MN-m/COIL
TRANSLATIONAL FORCE	44 MN/COIL
STRUCTURE MATERIAL	304 SS
YIELD STRENGTH	407 MPa AT 20 K

TABLE 10-1 (CONTINUED)

BURIAL CHAMBER	
COLLECTOR PANEL AREA	188 m^2
PEAK THERMAL LOAD ON PANEL	0.32 kW/cm^2
PEAK THERMAL LOAD ON SHIELD TUBE	3.2 kW/cm^2
PARTICLE FLUX	$1.9 \times 10^{20}/s\text{-}m^2$
CRYOSORPTION AREA (DUAL SYSTEM)	90 m^2
COOLING WATER	
INLET TEMPERATURE (MAXIMUM)	170°C
INLET PRESSURE (MAXIMUM)	34 atm
PUMP WORK	< 0.1 MW
MAXIMUM THERMAL SHIELD CREEP DAMAGE	<2%/YEAR
OPERATING PRESSURE	10^{-5} TORR
PULSE LENGTH (MAXIMUM HOLDING TIME)	600 s

the collector panels. This will eliminate the temperature fluctuations due to the shuttling of the collector system to and from the high temperature degassing chambers. The use of sodium or lithium as a coolant may improve the performance and lifetime of the collector panel and thermal shield tube and must be evaluated.

The placement of the divertor coils inside the vessel duct extensions was chosen for maintenance purposes. The divertor assembly, including the shielding, can be pulled out easily as a unit or each divertor coil assembly removed separately without the use of specialized remote servicing equipment. The maintenance procedure is under development.

The scaling of divertor coils is influenced by the magnetic field intensity, TF coil number and size, the shielding space between plasma and divertor, and reactor size. Designing for a large number of TF coils is clearly not a good choice for a reactor from engineering considerations. A number around 16 is favorably considered today. The size of the TF coils is determined by ripple, blanket and shielding, access and other engineering considerations. The existing design can accommodate a divertor with sufficient shielding space (70 cm). A large device size favors divertor scaling. The only issue is the magnetic field intensity which, for the DTHR design, is in the right range ($\sim$ 5.5 T). There are good indications that higher fields are still possible. Therefore, the divertor coil design can be scaled to a reactor.

The particle collector design was based on the assumptions which are most stringent. Relaxed conditions can be anticipated as better understanding of plasma behavior in the scrape-off layer, confinement times, and magnetic configurations are developed.

11.0 REFERENCES

1. T. F. Yang, A. Y. Lee, G. W. Ruck, W. J. Lange, "A Compact Poloidal Divertor Reference Design for TNS," IEEE Proc. 7th Symposium on Engineering Problems of Fusion Research, Vol. I, 178, Knoxville TN (1977).

2. P. E. Stott, C. M. Wilson, A. Gibson, "The Bundle Divertor - Part I; Magnetic Configuration," Nuclear Fusion, Vol. 17 #3, 481 (1977).

3. H. J. Grawley, "The Practical Feasibility of a Bundle Divertor for a Tokamak Power Reactor," Proc. Ninth Symposium on Fusion Technology, Garmisch-Partenkirchen, W. Germany (1976).

4. G. M. Swift and F. H. Southworth, "Bundle Divertor Designs for ILB Advanced Fuel Tokamaks," Proc. 7th Symposium on Engineering Problems of Fusion Research, Vol. II, 1198, Knoxville TN (1977).

5. T. F. Yang, "An Improved Bundle Divertor Design for ISX-B," WFPS-TME-075, Westinghouse Electric Corp. (1978). Also "A Consideration of Bundle Divertor for TNS," ANS Transactions, Vol. 27, 57, San Francisco CA (1977).

6. A. D. Sanderson, P. E. Stott, "A Bundle Divertor for Fusion Reactor," CLM-P530, Culham Laboratory, Abingdon, Oxfordshire, England (1978).

7. J. Sheffield, R. A. Dory, "The Ripple Bundle Divertor for Tokamaks," ORNL/TM-6220 (1978).

8. T. C. Varljen, J. L. Kelly, G. Gibson, R. P. Rose, "Preliminary Consideration of a Multipurpose Fusion-Fission Hybrid Facility," ANS Transactions, Vol. 30, 51, Washington DC (1978).

9. DTHR Reference Design Summary, WFPS-TME-107, Westinghouse Electric Corp. (1978).

10. A. Mense, Ph D. Dissertation, University of Wisconsin (1977).

11. A. J. Mense, G. A. Emmert, J. D. Callen, Nuclear Fusion 15, 703 (1975).

12. A. H. Boozer, A. B. Rechester, "Effect of magnetic perturbations on Divertor Scrape-off Width," Physics of Fluids, Vol. 21, 682 (1978).

13. M. Keilhacker, "Physics of Divertors and the Scrape-off Layer," IPP III/42, Max Plank Institut fur Plasma Physik (1978).

14. F. L. Hinton, F. L. Hazeltine, "Kinetic Theory of Plasma Scrape-off in a Divertor Tokamak," Physics of Fluids, Vol 17, 2236 (1974).

15. S. Hsuan, M. Okabayashi, S. Ejima, "Measurement of Plasma Flow Velocity into the Divertor of the FM-1 Sperator by Using Ion Accustic Waves Propagation," Nuclear Fusion 15, 191 (1975).

16. H. Kimura, et al., JAERI-M 6861-6971, Japan Atomic Energy Research Institute (1977).

17. P. E. Scott, C. M. Wilson, and A. Gibson, "The Bundle Divertor-Part II Plasma Properties," Nuclear Fusion 184, 475 (1978) and references cited.

18. L. Rosai, B. Ferrario, P. della Porta, "Behavior of Sorb-AC Wafer Pumps in Plasma Machines," A.V.S., Boston MA (1977).

19. P. A. Redhead, J. P. Hobson, and E. V. Kornelson, The Physical Basis of Ultrahigh Vacuum, Chapman & Hall, London (1967).

20. H. J. Halama, J. R. Argus, "Measurements of Absorption Isotherms and Pumping Speed of Helium on Molecular Sieve in the 10^{-11}-10^{-7} Torr Range at 4.2 K," J.V.S.T. Vol. 11, 333 (1974).

21. G. H. Miley, "Surface Effects Related to Voltage Breakdown in CTR Devices," Journal of Nuclear Materials, Vol. 63, 331 (1976).

22. P. J. Harbour, M.F.A. Harrison, "The Influence of Electron Emission at the Divertor Target of a Tokamak Fusion Reactor," CLM-P528, Culham Laboratory, England (1978). To be published in 3rd Intl. Conf. on Plasma Surf. Interactions in Contr. Fus. Devices, Culham England (1978).

23. T. F. Yang, J. D. Callen, "The Stability of Plasma in a Bundle Divertor," Westinghouse Electric Corporation, to be published.

24. R. F. Lopina and A. E. Bergles, "Heat Transfer and Pressure Drop in Tape-Generated Swirl Flow of Single-Phase Water," Trans. of ASME, Journal of Heat Transfer, pp 434-442 (August 1969).

25. H. F. Poppendiek and W. R. Gambill, "Helical, Forced-Flow Heat Transfer and Fluid Dynamics in Single and Two-Phase Systems," Proc. of the 3rd International Conference on the Peaceful Use of Atomic Energy, pp 274-283 (1964).

26. J. Kim, et al., "A Heat Transfer Study of Water-Cooled Swirl Tubes for Neutral Beam Targets," Proc. of the 7th Symposium on Engineering Problems of Fusion Research, pp 1593-1594 (1977).

27. T. V. Prevenslik, "Structural Evaluation of a DTHR Bundle Divertor Particle Collector," WFPS-TME-100, Westinghouse Electric Corp. (1978).

28. T. C. Varljen, G. Gibson, J. W. French, F. M. Heck, "Engineering Parameters for Four Ignition TNS Tokamak Reactor Systems," IEEE 7th Symposium on Engineering Problems of Fusion Research, Vol. I, 76, Knoxville TN (1977).

29. M. A. Abdou, "Nuclear Design of the Blanket/Shield System for a Tokamak Experimental Power Reactor, ANL/CTR/TM-51 (1975).

30. H. Brechna, "Effect of Nuclear Radiation on Organic Materials; Specifically Magnet Insulators in High Energy Accelerators," SLAC 40, Stanford Linear Accelerator Center (1965).

31. B. Badger, et al., "UWMAK-I, A Wisconsin Toroidal Fusion Reactor Design," FDM-68, University of Wisconsin (1973).